Old Dominion University

ODU Digital Commons

Mechanical & Aerospace Engineering Theses & Dissertations

Mechanical & Aerospace Engineering

Spring 2016

Thin Film Studies Toward Improving the Performance of Accelerator Electron Sources

Md Abdullah Al Mamun
Old Dominion University, mmamu001@odu.edu

Follow this and additional works at: https://digitalcommons.odu.edu/mae_etds

 Part of the Materials Science and Engineering Commons, Mechanical Engineering Commons, and the Power and Energy Commons

Recommended Citation

Al Mamun, Md A.. "Thin Film Studies Toward Improving the Performance of Accelerator Electron Sources" (2016). Doctor of Philosophy (PhD), Dissertation, Mechanical & Aerospace Engineering, Old Dominion University, DOI: 10.25777/ndwn-4a14
https://digitalcommons.odu.edu/mae_etds/6

This Dissertation is brought to you for free and open access by the Mechanical & Aerospace Engineering at ODU Digital Commons. It has been accepted for inclusion in Mechanical & Aerospace Engineering Theses & Dissertations by an authorized administrator of ODU Digital Commons. For more information, please contact digitalcommons@odu.edu.

THIN FILM STUDIES TOWARD IMPROVING THE PERFORMANCE OF ACCELERATOR ELECTRON SOURCES

by

Md Abdullah Al Mamun
B.Sc., Sep 1999, Bangladesh University of Engineering and Technology, Bangladesh
MBA, Nov 2005, IBA, University of Dhaka, Bangladesh
M.Sc., Aug 2009, Florida Atlantic University, USA

A Dissertation Submitted to the Faculty of
Old Dominion University in Partial Fulfillment of the
Requirements for the Degree of

DOCTOR OF PHILOSOPHY

MECHANICAL AND AEROSPACE ENGINEERING

OLD DOMINION UNIVERSITY
May 2016

Approved by:

Abdelmageed A. Elmustafa (Director)

Miltiadis Kotinis (Member)

Dipankar Ghosh (Member)

Bernard Matthew Poelker (Member)

ABSTRACT

THIN FILM STUDIES TOWARD IMPROVING THE PERFORMANCE OF ACCELERATOR ELECTRON SOURCES

Md Abdullah Al Mamun
Old Dominion University, 2016
Director: Dr. Abdelmageed A. Elmustafa

Future electron accelerators require DC high voltage photoguns to operate beyond the present state of the art to conduct new experiments that require ultra-bright electron beams with high average current and higher bunch charge. To meet these demands, the accelerators must demonstrate improvements in a number of photogun areas including vacuum, field emission elimination in high voltage electrodes, and photocathodes. This dissertation illustrates how these improvements can be achieved by the application of suitable thin-films to the photogun structure for producing ultra-bright electron beams.

This work is composed of three complementary studies. First, the outgassing rates of three nominally identical 304L stainless steel vacuum chambers were studied to determine the effects of chamber coatings (silicon and titanium nitride) and heat treatments. For an uncoated stainless steel chamber, the diffusion limited outgassing was taken over by the recombination limited process as soon as a low outgassing rate of ~1.79(±0.05) × 10^{-13} Torr L s^{-1} cm^{-2} was achieved. An amorphous silicon coating on the stainless steel chambers exhibited recombination limited behavior and any heat treatment became ineffective in reducing the outgassing rate. A TiN coated chamber yielded the smallest apparent outgassing rate of all the chambers: 6.44(±0.05) × 10^{-13} Torr L s^{-1} cm^{-2} following an initial 90 °C bake and 2(±20) × 10^{-16}

Torr L s^{-1} cm^{-2} following the final bake in the series. This perceived low outgassing rate was attributed to the small pumping nature of TiN coating itself.

Second, the high voltage performance of three TiN-coated aluminum electrodes, before and after gas conditioning with helium, were compared to that of bare aluminum electrodes and electrodes manufactured from titanium alloy (Ti-6Al-4V). This study suggests that aluminum electrodes, coated with TiN, could simplify the task of implementing photocathode cooling, which is required for future high current electron beam applications. The best performing TiN-coated aluminum electrode demonstrated less than 15 pA of field emission current at −175 kV for a 10 mm cathode/anode gap, which corresponds to a field strength of 22.5 MV/m.

Third, the effect of antimony thickness on the performance of bialkali-antimonide photocathodes was studied. The high-capacity effusion source enabled us to successfully manufacture photocathodes having a maximum QE around 10% and extended low voltage 1/e lifetime (> 90 days) at 532 nm via the co-deposition method, with relatively thick layers of antimony (≥ 300 nm). We speculate that alkali co-deposition provides optimized stoichiometry for photocathodes manufactured using thick Sb layers, which could serve as a reservoir for the alkali.

In summary, this research examined the effectiveness of thin films applied on photogun chamber components to achieve an extremely high vacuum, to eliminate high voltage induced field emission from electrodes, and to generate photocurrent with high quantum yield with an extended operational lifetime. Simultaneous implementation of these findings can meet the challenges of future ultra-bright photoguns.

Copyright, 2016, by Md Abdullah Al Mamun, All Rights Reserved.

This dissertation is dedicated to the innocent victims of modern civilization.

ACKNOWLEDGMENTS

This material is based on work supported by the U.S. Department of Energy (DOE), Division of Material Sciences under Grant No. DE-FG02-97ER45625, Office of Science and Office of Nuclear Physics under Contract No. DE-AC05-06OR23177, the DOE R&D for Next Generation Nuclear Physics Accelerator Facilities Funding Opportunity No. DE-FOA-0000339, and the National Science Foundation under Grant No. DMR-0420304. This work is also supported by Jefferson Science Associates under U.S. DOE Contract No. DE-AC05-84ER40150 and funded from the DOE Office of High Energy Physics and the Americas Region ILC R&D Program.

I am grateful to my dissertation advisor Dr. Abdelmageed Elmustafa and to my supervisor Dr. Matthew Poelker for their constant guidance and full support throughout this research. I thank my dissertation committee members for their suggestions and support. My deep appreciation goes to Dr. Marcy L. Stutzman, Dr. Carlos Hernandez-Garcia, Dr. Russell Mammei, Dr. Shukui Zhang, Eric Foreman, Rhys Taus, Phillip Adderley, Jim Clark, John Hansknecht, and Steven Covert for their great cooperation and technical support during this research. I also thank Dr. Wei Cao and Dr. Kai Zhang of ODU; and the surface characterization lab staff members of the College of William & Mary for their support regarding the surface characterization experiments.

Finally, I thank my family members for their patience and support.

TABLE OF CONTENTS

Page

LIST OF TABLES x

LIST OF FIGURES xii

CHAPTER

1. INTRODUCTION 1
   - 1.1. Background 1
   - 1.2. Motivation 3
   - 1.3. Approach 5
     - Gas load reduction for vacuum improvement 6
     - Elimination of high voltage induced field emission from electrodes 8
     - Optimization of quantum yield and lifetime of photocathodes for high current delivery 10
   - 1.4. Scope of the work 13
   - 1.5. Goals and objectives 14
   - 1.6. Outline of the experiments 14
     - Investigation on outgassing rates of vacuum chambers 15
     - Investigation on high voltage induced field emission from electrodes 15
     - Investigation on optimizing the photocathode fabrication 16
   - 1.7. Outline of the dissertation 16

2. EFFECTS OF HEAT TREATMENTS AND COATINGS ON THE OUTGASSING RATE OF STAINLESS STEEL CHAMBERS 18
   - 2.1. Introduction 18
   - 2.2. Experiment 20
     - Chamber fabrication 20
     - Coating details 21
     - Outgassing measurement 22
     - Coating analysis 23
   - 2.3. Results 24
     - Bare stainless steel 24
     - Amorphous Si coating 26
     - TiN coating 29
     - Coating analysis 32
   - 2.4. Discussion 34
   - 2.5. Summary 38

Chapter Page

2.6. Conclusion 39

3. TIN COATED ALUMINUM ELECTRODES FOR DC HIGH VOLTAGE ELECTRON GUNS 40
3.1. Introduction 40
3.2. Experiment 44
Apparatus 44
Polishing and preparing the electrodes 48
3.3. High voltage test results 49
HV characterization results of bare aluminum electrodes 52
HV characterization results of TiN coated aluminum electrodes 53
HV characteristics results of diamond paste polished Ti-alloy electrodes 54
3.4. Surface evaluation 55
Topography and chemical composition 55
Hardness measurement 58
3.5. Summary 61
3.6. Conclusion 63

4. EFFECTS OF ANTIMONY THICKNESS ON THE PERFORMANCE OF BIALKALI-ANTIMONIDE PHOTOCATHODES 64
4.1. Introduction 64
4.2. Experiment 66
Deposition chamber 66
Vacuum protocols 69
Vent-bake protocols 70
Vent-no-bake protocols 70
Antimony deposition and surface characterization 71
Effusion source for alkali codeposition 73
Photocathode preparation 74
Photoemission characterization 76
4.3. Results and discussion 77
Effects of vacuum practice on Sb growth 77
FESEM results 77
XRD results 80
AFM results 82
Quantum efficiency of photocathodes 84
QE lifetime of photocathodes 89
Spectral response 90
Correlations between Sb thickness, chemical consumption and photocathode optical performance 92

Chapter Page

4.4. Conclusion 95

5. CONCLUSIONS 97
5.1. Summary 97
5.2. Future work 100

REFERENCES 103

APPENDICES 116

VITA 139

LIST OF TABLES

Table Page

2.1. Uncoated chamber (SS1) bake history and corresponding outgassing rate at 20 °C 24

2.2. Amorphous silicon coated (a-Si) chamber bake history and corresponding outgassing rates at 20 °C 27

2.3. Chamber coated with amorphous silicon following heat treatment (SS1:a-Si) bake history and corresponding outgassing rate at 20 °C. The outgassing rate of SS1 prior to coating with a-Si was 1×10^{-13} Torr L s^{-1} cm^{-2} 28

2.4. Titanium nitride coated chamber (TiN) bake history and corresponding outgassing rate at 20 °C. Outgassing rates may be artificially low if there is any pump speed in the system, and the inhomogeneity found in the EDS analysis suggests the presence of some elemental Ti 31

2.5. Coating thickness and RMS roughness values for bare steel, TiN coated and a-Si coated test samples 34

3.1. Relevant characteristics of candidate electrode materials at room temperature 41

3.2. Field strength required to produce 100 pA of field emission, following helium gas conditioning, except titanium alloy sample TA2, which did not require it. For entries with (>) symbol, field emission current did not exceed 100 pA at −225 kV bias voltage, the maximum voltage available 50

4.1. List of deposition conditions and the corresponding Sb thickness in micrometer. On GaAs substrates, a direct measurement of Sb film thickness was possible via cross-section views using FESEM. For Ta substrates, the Sb film thickness was estimated using the relationship obtained among grain size, roughness, and thickness from Sb films on GaAs 84

LIST OF FIGURES

Figure Page

2.1. Schematic of the outgassing measurement experimental apparatus during a 400 °C bake showing the chamber, SRG, isolation valve, and pumps. For bakes at lower temperature, the first isolation valve, the ion pump, and the RGA were within the oven 21

2.2. Representative rate-of-rise data at four room temperatures. These data were obtained using the SS1 stainless steel chamber, and correspond to outgassing rates between 1.4×10^{-13} and 5.5×10^{-13} Torr L s^{-1} cm^{-2} following a 150 °C bake (third in the series noted in Table 2.1). A least-square linear fit was used for each data set to calculate outgassing rates 23

2.3. Outgassing rates for the bare stainless steel (SS1) chamber as a function of inverse room temperature, with each data set obtained following a bake at the temperature noted in the legend. The error bars for statistical and systematic errors are smaller than the data points for these data. The slope yields the temperature dependent activation energy as described in the text 26

2.4. Outgassing rates for the a-Si and the SS1:a-Si chambers as a function of inverse room temperature, with each data set obtained following a bake at the temperature noted in the legend. The low outgassing rate of the heat treated SS1 chamber (solid stars) was largely preserved following coating the chamber with a-Si and baking. The error bars for statistical and systematic error are comparable in size to the data points shown for these data 29

2.5. Outgassing rates for the TiN-coated stainless steel chamber as a function of inverse room temperature, with each data set obtained following a bake at the temperature noted in the legend. The best outgassing rate for the SS1 bare stainless steel chamber is plotted for reference. Systematic and statistical errors, though small at larger

Figure Page

outgassing rates, become significant at the lowest measured outgassing rates 31

2.6. EDS and SEM data show coating composition and morphology for (a) bare stainless steel, showing expected composition and morphology, (b) a-Si on stainless steel, with a Si peak evident in conjunction with the steel substrate, and (c) TiN coating with approximately 1:1 atomic ratio of Ti and N, but obvious particulate matter and pores visible across the surface. Inset SEM images each show a 120 μm × 80 μm area.... 33

2.7. Outgassing rates for each chamber are plotted vs the Fourier number, F_0. The straight line represents the calculated outgassing rate for the systems using Fick's law, disregarding surface effects. For the steel chambers, the transition from diffusion limited reduction in outgassing rate to recombination limited behavior occurs near $F_0 = 1$, with the outgassing rates vs F_0 in close agreement with Fick's law at low F_0 (see inset), and diverging from Fick's law toward recombination limited behavior at higher F_0 values. The a-Si chambers have outgassing rate largely independent of F_0 suggesting that the surface effects of the system dominate the outgassing, and diffusion of hydrogen from the material during bakes is not significant. The steep slope of the TiN indicates either an excellent diffusion barrier or a slight pumping speed in the coating that increases with additional heat treatment 36

3.1. (a) Schematic of the insulator, test electrode and anode used to collect the field emission. Photographs of the dc high voltage field emission test stands—(b) baked chamber TS1 and (c) unbaked chamber TS2 used to evaluate each cathode electrode 45

3.2. Field emission current vs bias voltage and field strength for different cathode/anode gaps for (a) bare aluminum, (b) TiN-coated aluminum, and (c) titanium alloy electrodes. Labels with "B" represent electrodes that are tested in the baked chamber TS1 51

3.3. SEM images of bare and TiN-coated aluminum electrode surface, (a) bare aluminum

Figure Page

electrode surface showing a typical defect, (b) bare aluminum electrode surface showing a defect produced as a result of helium gas conditioning, (c) TiN-coated aluminum electrode surface showing a subsurface defect covered by TiN coating, and (d) TiN-coated electrode surface subjected to high field strength, and damaged postbreakdown 56

3.4. Surface morphology of the TiN coated 1200 grit polished Al6061 coupon revealed by AFM with (a) 3D and (b) 2D displays. RMS roughness and average grain height were measured as 7 and 20 nm, respectively, for the scan area of 1 μm × 1 μm 57

3.5. (a) Hardness and (b) modulus as a function of contact depth of indentation for uncoated and TiN coated Al6061. The error bars represent three standard errors 59

3.6. SEM images of the residual impressions of (a) 500 nm and (b) 3 μm Berkovich indents on the TiN coated 1200 grit polished Al6061 coupon. The occurrence of cracks for the larger indent was observed as pop-in events during indentation 60

3.7. Load vs displacement into surface for 2 μm indents on uncoated and TiN coated Al6061 coupons with 1200 grit surface finish. Pop-in events observed for indenter penetration depth of >450 nm indicate fracture incidences 61

4.1. (a) Photograph of the bialkali-antimonide photocathode deposition chamber with effusion-type alkali dispenser (shown in the inset), (b) schematic of the substrate holder assembly with substrate heater, (c) photograph of the laser system with the mirrors attached to the stepper-motor-controlled translation stages, (d) photograph of the GaAs substrate secured to the sample holder using an annular Ta cup, and (e) schematic of the effusion-type alkali dispenser used for coevaporation of K and Cs species (with permission from Lawrence S. Cardman) 67

4.2. FESEM images illustrating topography and cross-sectional views of Sb films grown on Ta and GaAs substrates for 100 and 120 min deposition times, with 32.7(±0.2) and

Figure Page

33.7(±0.2) A current, respectively, applied to the Sb crucible heater, under two different vacuum protocols: [(a) and (b)] vent-bake and [(c) and (d)] vent-no bake. For vent-bake vacuum protocol, the normal operating pressure was ~10^{-7} Pa. For vent-no bake vacuum protocol, the pressure was ~10^{-6} Pa 79

4.3. XRD patterns of Sb films with varying thicknesses deposited on GaAs substrate. Antimony films deposited under vent-bake protocol are labeled with asterisk (*) 81

4.4. AFM images illustrating surface morphology of Sb films grown on Ta and GaAs substrates for [(a) and (b)] 100 min with 32.7(±0.2) A, and [(c) and (d)] 120 min with 33.7(±0.2) A current applied to the Sb crucible heater following the vent-no bake protocol 83

4.5. RMS roughness and grain size as function of Sb thickness for Sb films deposited on GaAs substrate. Fitting parameters: a = 29.57444, b = 5.248599, c = 0.4383123, and d = 129.843 (R^2 = 0.9976) 83

4.6. QE (%) map of the photocathodes biased at 284 V with 532 nm (3.96 mW). The photocathodes were prepared by bialkali codeposition following the vent-bake protocol on (a) a 30 min grown Sb layer and (b) a 100 min grown Sb layer; and following the vent-no bake protocol on (c) a 100 min grown Sb layer. Z axis in the 3D plot represents QE (%) 86

4.7. FESEM topography and QE distribution of the photocathodes biased at 284 V with 532 nm (3.96 mW). The photocathodes were prepared by bialkali codeposition following the (a) vent-bake protocol on a 100 min grown Sb layer and (b) vent-no bake protocol on a 100 min grown Sb layer 87

4.8. QE as a function of Sb thickness for bialkali-antimonide photocathodes deposited on Ta and GaAs substrates. The photocathodes were biased at 284 V and illuminated with 4 mW of laser light at 532 nm 88

Figure Page

4.9. (a) QE decay as a function of illumination time, (b) QE lifetime as a function of Sb thickness (t_{Sb}) for bialkali-antimonide photocathodes created under vent-no bake practice. The photocathodes were prepared by bialkali codeposition following the vent-no bake protocol and illuminated with 532 nm (3.96 mW) at 284 V bias 90

4.10. (a) Spectral response of bialkali-antimonide photocathode deposited on Ta and GaAs substrates are shown together with the spectral response of conventional bialkali-antimonide photocathodes used in photomultiplier tubes. QE distribution is shown for 425 and 532 nm. The photocathode was prepared by bialkali codeposition on Sb layer of ~300 nm thickness deposition following the vent-no bake protocol 91

4.11. Normalized quantity (Q) of source materials for optimal QE as a function of Sb thickness (t_{Sb}) for bialkali-antimonide photocathodes manufactured via codeposition of alkali species..... 93

CHAPTER 1

INTRODUCTION

1.1. BACKGROUND

Electron accelerators generate highly energetic electron beams that are utilized for a variety of basic research and industrial applications [1-3]. The diverse application of electron-beams includes investigation of the fundamental nature of matter, characterization and modification of material properties, surface treatment and semiconductor processing, microscopic surface physics studies, radiation therapy for medical sterilization, inspection of nuclear fuels, production of fissile materials for nuclear weapon, and many more [4,5]. An electron gun operates under very high vacuum where a cathode produces the free electron beam delivered to the accelerator that increases the energy of the electron. Electron beam technology has undergone numerous modifications over the long history of the development of electron beam devices [2]. Various electron beam sources have been developed for different applications by modifying the electron beam parameters such as diameter, current, energy, polarization, emittance, etc. to meet the particular application requirements [6].

National Laboratories under the Department of Energy (DOE) have played a central role in pioneering accelerator technologies. The invention of the free electron laser (FEL) in the 1970s enabled generating ever-higher-power electromagnetic radiation using high-energy electrons which is of direct interest to defense applications and led to the Navy's proposed application of free-electron laser technology to shipboard defense [7,8].

Electron guns can be classified based on the emission mechanism (thermionic, cold emission, plasma source, or photocathode), by the type of electric field generation (direct current or radio frequency), by the number of electrodes, or by focusing (pure electrostatic or with magnetic fields). The first generation electron guns were thermionic guns which relied on a thermal emitter [9]. However, thermionic emission cathodes were unable to provide polarized electron beams which were later produced by photoemission cathodes to conduct fundamental physics studies [10]. Afterward, the direct current (DC) electron guns and photoemission cathodes went through continuous development for improved polarized electron sources, and much of this developmental work has been reported in the proceedings associated with the series of Spin Physics conferences [9]. In 1981, the Stanford Linear Accelerator (SLAC) demonstrated the use of GaAs photocathode in a radio frequency (RF) synchronized electron gun to produce electron beams with very high peak currents (60 A leaving the cathode) and large bunch charges (>8 nC per bunch) in relatively short duration (~2 ns) pulses [11]. In 1985, the achievement of high peak currents over 200 A/cm^2 from a pulsed-laser irradiated Cs_3Sb photocathode was reported [12]. In 1987, Los Alamos National Lab developed the RF gun with Cs_3Sb photocathode that employed short optical pulses at high repetition rates and high peak brightness to deliver trains of high charge bunches (27 nC) for FEL applications [13]. These early developments led to the increasing use of photoemission cathodes in both DC and RF electron guns to deliver high brightness and high bunch charge electron beams [9].

The Thomas Jefferson National Accelerator Facility (Jefferson Lab) is known for its unique particle accelerator, the Continuous Electron Beam Accelerator Facility (CEBAF), which is used to conduct basic research of the atom's nucleus. Jefferson Lab developed CEBAF to conduct high-

precision electromagnetic nuclear physics experiments at high beam energies up to 4 GeV and deliver CW beams of high average current (up to 200 μA) with very low energy spread ($\Delta E/E_{rms} < 2 \times 10^{-5}$) and small emittance ($\varepsilon_{n,\,rms} < 1$ mm-mrad) [14]. Jefferson Lab is also the home of an Energy Recovery Linac (ERL) that is primarily used to support the FEL where a DC high voltage photogun operates at much higher bias voltage compared to the CEBAF photogun to provide higher bunch charge. In addition, the photogun must deliver considerably higher average current up to 10 mA. The electron beam at the Jefferson Lab ERL is not polarized and this allows use of photocathodes with considerably higher quantum efficiency (QE).

1.2. MOTIVATION

At CEBAF of Jefferson Lab, the typical photocathode operating lifetime is 100 C. This indicates that an electron charge of 100 C can be extracted before the photocathode quantum efficiency (QE) falls to 1/e (~36.8%) of its initial value. This definition of lifetime is somewhat arbitrary in the sense that with sufficient laser power, it is possible to operate beyond the 1/e lifetime, but this metric provides a reasonably good basis for quantifying gun performance. Frequently, the nuclear physics experiments at CEBAF require average current of 200 μA from the gun, running continuously for months. The typical 100 C photocathode lifetime can provide uninterrupted beam delivery for about 6 days before the laser must be directed to a "fresh" location on the photocathode. Eventually, QE is low across the entire photocathode surface and the photocathode must be heated and reactivated, a process that accounts for ~12 h of accelerator downtime. The most demanding experiments for the polarized source at CEBAF are parity violation experiments, which require extremely stable beam conditions. Improved photocathode lifetime beyond 100 C

would reduce downtimes, and would improve beam quality by helping to minimize long-term helicity correlated beam systematic variations, e.g., charge and position asymmetry.

In recent years, ambitious electron accelerators are being proposed for various new applications [9]. Electron Ion Collider (EIC) proposals require electron beams with high average current and high bunch charge to achieve ambitious luminosity goals [15]. Specifically, the electron ion collider eRHIC proposal requires 50 mA polarized electron beam with 3.5 nC bunch charge. eRHIC and a competing EIC proposal MEIC both expect to cool proton beams using unpolarized electron beams with ~100 mA average current and >1 nC bunch charge [15,16]. For proposed accelerators such as eRHIC that must operate at milliampere average beam current, it is even more important to extend the operating lifetime of today's GaAs photoguns. The initial phase of operation for the eRHIC ERL-Ring accelerator complex calls for 25 mA average current of highly polarized electrons. At 25 mA, the gun must provide over 2000 C/day. A polarized electron source with charge lifetime of 100 C can deliver 25 mA for just one hour before QE falls to 1/e of its initial value. Ultimately, the eRHIC ERL-Ring facility might need to operate at 250 mA e-beam current, or 20,000 C/day, to achieve the facility's desired luminosity. A photogun with today's 100 C charge lifetime would support eRHIC scientific productivity for just minutes, which is clearly an unacceptable condition. A charge lifetime of 100 C is representative of photoguns operating at ~100 μA. Charge lifetime would likely be much less at milliampere current levels, since lifetime drops with increasing beam current. Hence, even these bleak estimates for operating time at milliampere current are likely optimistic.

Typically, RF or SRF guns are considered for nC bunch charge applications. While DC high voltage guns are considered for high average current CW beams applications. No photogun exists

today that simultaneously provides nC bunch charge and high average current CW beam. Therefore, extending photogun capability to achieve these requirements represents an important EIC R&D goal. Successful operation of a DC high voltage photogun at 500 kV will help overcome the space charge forces that degrade beam quality at nC bunch charge. The electron source and injector system are vital components for these applications and photoemission cathodes are preferred as the electron sources to produce very high beam brightness [9]. Electron beams with high average current, small emittance, very low energy spread and high polarization with extended periods of lifetime are the demanding beam quality specifications for supporting the experimental needs [14].

1.3. APPROACH

Many present and future particle accelerators are limited by the stringent requirements of extreme high vacuum, maximum electric field gradient and peak surface fields that can be realized inside direct current (DC) high voltage photoelectron guns, and high quantum yield as well as extended lifetime from photocathodes to satisfy high current applications. Vacuum, field emission and photocurrent are thus vital aspects of photogun technology. The governing phenomena of these aspects have inherent similarities (see appendices) and the surface properties of gun structure materials can directly influence these phenomena. Thin films offer greater control for modifying the surface properties of functional materials and thus offer opportunity for overcoming the limiting aspects of current photoguns. The detailed approaches for implementation of thin films in photogun structure toward improvement of photogun performance are discussed in following subsections with brief backgrounds of the problems.

1.3.1. Gas load reduction for vacuum improvement

Improved vacuum is essential to improving the electron gun charge lifetime at high average current. New accelerator initiatives [15,16] like eRHIC require spin-polarized photoguns with performance characteristics considerably beyond today's state of the art. Namely, the GaAs photogun must provide very high average current (>>1 mA) at high polarization and with sufficiently long operating lifetime. Extending the operating lifetime of DC high voltage GaAs photoguns, especially at mA beam currents, depends on our ability to improve vacuum inside the gun high-voltage vacuum chamber.

Imperfect vacuum and the associated phenomenon known as 'ion back bombardment' are the chief factors limiting the performance of modern DC high voltage GaAs-based spin-polarized electron sources [14,17]. Residual gas inside the gun vacuum chamber and nearby beamline can be ionized by the extracted electron beam. Ions produced within the cathode/anode gap are accelerated toward the photocathode by the gun's static electric field. Ions with sufficient kinetic energy can strike the photocathode surface and sputter away the chemicals used to create the necessary negative electron affinity condition. Energetic ions can also penetrate the photocathode surface, damaging the GaAs crystal structure or serving as unwanted interstitial defects that alter the electron diffusion length within the material, reducing photocathode QE.

A measurable and marked improvement in gun vacuum can be achieved by implementing a prolonged bake of the gun vacuum chamber at 400°C, which serves to reduce the chamber outgassing rate [18]. As such, this heat treatment has become the 'standard practice' at CEBAF of Jefferson Lab. Further vacuum improvement, however, demands that we lower the gas load or increase available pump speed. NEGs and ion pumps are used for pumping for many years, but

it is possible they limit the ultimate pressure inside the photogun. For example, it is widely known that ion pump speed falls as the system pressure drops below 1×10^{-10} Torr, and it is possible that the ion pump represents a source of gas (rather than a pump) in the XHV systems. Also, NEG pump speed is highest following high temperature activation where the NEGs are heated to release the adsorbed hydrogen and drive the heavier getterable gasses into the NEG material. NEG activation introduces a high gas load that needs to be expelled from the system lest it re-contaminate the NEGs on cool down. Today's polarized electron source designs do not provide a means to adequately pump away this gas load. Cryo-condensation pumps are also used to achieve lower pressure, but they require careful shielding of the cold surface maintained at ~2 K, using chevrons at liquid nitrogen temperature. There are at least two drawbacks to cryo-pumps from an accelerator operations point of view. Commercial cryo-pumps employ compressors to generate liquid helium, and these compressors introduce unacceptable levels of mechanical vibration on the photogun during beam delivery. Another operations drawback is that eventually, the cold surfaces of the cryo-pump become saturated with adsorbed gas and pump speed diminishes. When this happens, a valve must be closed to isolate the cryo-pump from the gun vacuum chamber, and the cold surfaces must be warmed to expel the adsorbed gas. Large gate valves are expensive, and cryo-pump regeneration represents downtime—the photogun flaw we are striving to eliminate.

The operating lifetime of a photocathode within a DC high voltage photogun is limited by vacuum, which is determined in part by the outgassing rate of hydrogen from the vacuum chamber walls. By reducing the outgassing rate, the vacuum level improves proportionally and similarly, the operating lifetime of the photocathode. Thin-film coatings applied to the interior

and/or exterior surfaces of the vacuum chamber can reduce the outgassing rate and provide further vacuum improvement. Therefore, thin films will be investigated for their effectiveness to serve as diffusion barriers to reduce the gas load within ultrahigh vacuum chambers.

1.3.2. Elimination of high voltage induced field emission from electrodes

Successful operation of a DC high voltage photogun at high bias voltage requires that field emission be eliminated from the cathode electrode. Field emission is the unregulated release of electrons from the cathode electrode surface when the cathode is biased at high voltage. Field emission occurs when electrons tunnel through the barrier potential under the influence of very high fields of 10^9 V/m or more [19]. Operation of the photoemission electron guns at the very high bias voltages is required to produce low emittance beams, and field emission often limits the maximum achievable bias voltage, and consequently limits the electron beam energy [20-22]. Field emission is problematic for a number of reasons: it degrades the vacuum level via electron stimulated desorption and leads to shortened operating lifetime of the gun, it creates undesired x-rays that are harmful to nearby personnel, and high levels of field emission can damage electron gun components [17,23,24]. Despite considerable effort, a comprehensive theory of DC field emission has not been developed and mitigation techniques to improve practical maximum accelerating gradients have had only limited success. Part of the problem is that DC field emission involves a complex mixture of microscopic effects, which are determined by the geometry, metallurgy, and surface preparation of the accelerating structures (electrodes), and the vacuum conditions within the photogun.

Initial investigations revealed that field emission initiates from electrode sites where the work function is lower, and microstructural defects such as grain boundaries often serve as the low work function regions on the electrode surface [19,25,26]. Inert gas conditioning of electrodes has been proven to eliminate field emission from cathode electrodes of DC high voltage photoelectron guns via sputtering and implantation mechanisms that might improve the work function of the surface, and the effect is reversed when the electrode is heated [27]. Chemical contamination and particulate contamination or micro-protrusions also can lower the work function or often serves to enhance the localized electric field that can onset field emission at a lower bias voltage [28].

Today's photogun electrodes are painstakingly polished to a mirror-like surface finish that helps to prevent field emission [29-33]. Cathode electrodes for electron guns are typically manufactured from hard metals like stainless steel (SS), titanium-alloy (Ti-alloy), or molybdenum (Mo) [19]. Once fabricated at the machine shop, the relatively rough surface of the electrode must be mechanically polished by hand using silicon carbide paper and diamond grit, to obtain a smooth surface free of microscopic protrusions which cause field emission. However, the polishing process for electrodes manufactured from hard metals is time consuming and labor intensive. An alternative to this expensive polishing process might be the application of thin-film coating on electrodes that may provide a smooth surface finish and improved surface properties such as higher work function and defect free surface to reduce field emission. Therefore, thin films will be investigated for their effectiveness to suppress filed emission from cathode electrodes under very high voltage in a photogun.

1.3.3. Optimization of quantum yield and lifetime of photocathodes for high current delivery

In accelerator electron guns, a photocathode exploits the photoelectric effect to produce an electron beam. A good photocathode must withstand the accelerator environment's harsh electric fields, high currents, and chemical contaminants without degrading. The photocathode must also be able to generate a consistent high-quality electron beam over a long lifetime.

The significance of photocathodes with high QE at the longest practical wavelength for high average current and high bunch charge applications is underlined in the expressions of instantaneous current and bunch charge. A linear photoemission cathode can generate instantaneous current as expressed by:

$$I = \lambda \times P \times \mathrm{QE}(\%)/124, \tag{1.1}$$

where I (mA) is the instantaneous photocurrent, λ (nm) is the illumination wavelength, P (W) is laser power, and QE(%) is the cathode quantum efficiency which is the ratio of the number of emitted electrons to the number incident photons. The integral of this expression over time determines the bunch charge Q (nC) produced by an optical pulse of total energy E (μJ) and expressed by:

$$Q = \lambda \times E \times \mathrm{QE}(\%)/124. \tag{1.2}$$

Different photocathodes families have been used in electron accelerators; these include bare metals, conventional thermionic dispenser cathodes, alkali tellurides, alkali antimonides, and negative electron affinity (NEA) semiconductors [9,34,35]. Among these families, bare metals generally have QEs $\leq$ 0.01% and require UV illumination, while dispenser cathodes provide ~0.1% QE in the near UV. Clearly, bare metal photocathodes and dispenser cathodes appear unsuitable for higher average current applications. The remaining three cathode families provide

relatively high QE of which alkali tellurides and alkali antimonides have positive electron affinity (PEA). In the PEA case, the bottom of the conduction band lies below the external vacuum level, while in the NEA case, the conduction band minimum lies above the external vacuum level. Thus, in the NEA cathodes it is energetically possible for an electron at the conduction band minimum to escape, while this is not so for the PEA cathodes. Therefore, the PEA cathodes are not good in providing high QE in IR, while the NEA cathodes offer reasonably high QE from the near IR to the near UV. However, PEA cathodes being stoichiometric compounds are less susceptible to heating due to light absorption and ion-back bombardment. Tests conducted at Cornell indicated that in vacuum the temperature of an NEA cathode and its support can rise above 280 °C when illuminated by 20 W of green light [9].

Moreover, the particular damage mechanism in a NEA GaAs cathode from ion back bombardment is not yet fully understood, and sputtering of the cesium-fluorine activation layer in a NEA GaAs cathode is always a strong suspicion for the damage caused by ion back bombardment. Computations with the code SRIM indicate that the sputtering by the dominant residual gas component hydrogen may be adequate to explain the QE degradation in an ion back bombardment event. However, the removal of surface material by sputtering in stoichiometric compounds like alkali antimonide and telluride cathodes will always leave identical underlying material. Therefore, the alkali antimonide and alkali telluride photocathodes are less likely to be affected by ion-back bombardment as compared to NEA photocathodes.

Bialkali antimonide photocathodes thus represent a good alternative to delicate GaAs, providing similarly high quantum yield but exhibiting less sensitivity to ion back bombardment, and demonstrating more robust performance. Dowell *et al*., 1995 have successfully fabricated

CsK_2Sb photocathodes that yielded a QE of 12% which was used in the RF gun accelerator of the Boeing/Las Alamos Average Power Laser Experiment (APLE) [36]. Interest in these photocathode materials has been renewed due to the increasing demand for high current electron source applications such ERLs, EIC, MEIC, eRHIC, and electron beam cooling (EBC) [15,16]. Although several national laboratories are actively involved in improving the yield and lifetime of the CsK_2Sb including Brookhaven National Lab (BNL), Lawrence Berkeley National Lab (LBNL), and SLAC National Accelerator Lab, some questions about the physics of the photocathode materials remain unresolved. The Photocathode Physics for Photoinjectors (P3) workshops are devoted to improving the understanding of the physics of these photocathodes materials.

Today, Jefferson Lab relies on GaAs photocathodes, which provide good QE; however, this material is highly sensitive to vacuum condition, and photocathode lifetime is limited by many factors including poor vacuum, high voltage discharges within the gun, and low level field emission. The CsK_2Sb bialkali photocathode can be a potential substitute for GaAs because of its ability to survive under markedly harsher vacuum conditions compared to GaAs [37]. Moreover, alkali-antimonide photocathodes with positive electron affinity are considered 'prompt emitters' providing short electron bunches and small longitudinal emittance. Importance of these photocathodes has been revived as a result of new light source initiatives and proposed experiments that rely on high average current energy recovery linacs like the DarkLight experiment [38] and a necessity to employ electron cooling of proton beams for recent electron ion collider proposals [39].

For the past years, BNL and Jefferson Lab have been collaborating to study the characteristics of CsK_2Sb photocathodes inside a DC high voltage photogun. The first set of runs at 1 mA and at

100 kV bias voltage indicated disappointing charge lifetime, comparable to values obtained with GaAs photocathodes [40]. Surprisingly, following an inadvertent beam/vacuum event, lifetime improved dramatically, with QE virtually unchanged or increasing at currents up to 10 mA [37]. The photocathode lifetime degraded at current >10 mA, and further testing indicated this was due to laser heating and associated changes in photocathode chemical composition. The CsK_2Sb photocathode appears to be more rugged than the GaAs one; however, the chemistry could be very complicated, and the basic physics of bialkali-antimonide photocathode operation is not clearly understood [37]. Thus, continued evaluation of alkali-antimonide photocathodes is necessary to determine the exact recipe that provides optimum photocathode performance at high current.

1.4. SCOPE OF THE WORK

The outgassing, field emission and photoemission phenomena are fundamentally related to the electronic, structural and mechanical properties of materials such as bandgap energy, work function, activation energy, hardness, modulus, and microstructure. Thus, it is important to relate the outgassing from the gun structure material; the accelerating structure's field emission mechanisms including electric field, conditioning, and surface preparation of the electrodes; and the performance of the photocathode to their material properties. Old Dominion University's Applied Research Center (ODU-ARC) is an enterprise center and houses the following equipment: Transmission Electron Microscope (TEM), Scanning Electron Microscope with Energy Dispersive X-ray Spectroscopy (SEM-EDS), Atomic Force Microscope (AFM); Scanning Tunneling Microscope (STM), and Agilent XP Nano Indenter. Additional equipment includes: X-

Ray Photoelectron Spectroscope (XPS), Time-of-Flight Mass Spectrometer, Raman and Optical Spectrometer, Ellipsometer, and X-ray Diffraction (XRD). The ODU-ARC expertise on materials science and engineering combined with that of the Jefferson Lab electron source group expertise on actual photoguns provided a unique experimental opportunity.

1.5. GOALS AND OBJECTIVES

The goal of this dissertation is to improve the performance of Jefferson Lab's DC high voltage photoelectron gun using thin films to provide ultra-bright electron beams. In order to achieve this goal, experiments on thin films were designed to meet the following objectives: (1) achieving better vacuum using a barrier coating on the vacuum chamber wall to minimize outgassing (i.e., gas load) and improve the pump speed, (2) eliminating field emission under very high voltage from the cathode electrodes made of inexpensive materials with the application of TiN coating, and (3) identifying proper growth conditions for bialkali-antimonide photocathodes which can demonstrate high QE and extended lifetime.

1.6. OUTLINE OF THE EXPERIMENTS

In this dissertation, three complementary studies were performed to explore how suitable thin-films could be used to improve photogun vacuum and thereby prolong operation, eliminate field emission from high voltage electrodes, and to obtain high average current photocathodes. A brief outline with the context of these experiments is presented below.

1.6.1. Investigation on outgassing rates of vacuum chambers

This individual study evaluated the effectiveness of thin-film coatings on vacuum chambers to serve as diffusion barriers to reduce the gas load within ultrahigh vacuum chambers. For this purpose, we constructed three identical vacuum chambers made of stainless steel (SS304L). The outgassing rates of these nominally identical 304L stainless steel vacuum chambers were measured to determine the effects of chamber coatings and heat treatments. One chamber was coated with titanium nitride (TiN) and one with amorphous silicon (a-Si) immediately following fabrication. The last chamber was first tested without any coating and then coated with a-Si following a series of heat treatments. The outgassing rate of each chamber was measured at room temperatures between 15 and 30 °C following bakes at temperatures between 90 and 400 °C. The outgassing results were interpreted in terms of diffusion-limited versus recombination-limited processes. Surface science techniques including scanning electron microscopy (SEM) and surface profilometry were used to determine the topography and mechanical roughness of the coated and uncoated surfaces, and energy-dispersive x-ray spectroscopy (EDS) was used to assess the chemical composition of the coatings.

1.6.2. Investigation on high voltage induced field emission from electrodes

The aim of this individual study was to examine whether hard coating like titanium nitride (TiN) can be applied to the freshly fabricated rough surfaces of soft metal electrodes to eliminate the time consuming and labor intensive polishing process and still perform consistently well to suppress field emission of electrode under high voltage. For this, the high voltage performance of three TiN-coated aluminum electrodes, before and after gas conditioning with helium, was

compared to that of bare aluminum electrodes, and electrodes manufactured from titanium alloy (Ti-6Al-4V). As the excessive field emission often leads to permanent damage on the electrode surface, the surface topography of each electrode was investigated at every step of the polishing process, the coating process, and following each step of the high voltage evaluation, using a JEOL JSM-6060 LV scanning electron microscope (SEM). In addition, the surface roughness of each test electrodes was inferred based on AFM measurements of small test coupons (2 cm × 2 cm × 0.5 cm), before and after TiN coating. A harder electrode surface is anticipated to be less prone to surface damage due to handling and HV processing. Thus, the mechanical properties of the TiN coating, hardness and modulus, were evaluated using nanoindentation measurement, and compared to those of stainless steel, niobium, and titanium-alloy coupons.

1.6.3. Investigation on optimizing the photocathode fabrication

This individual study focused on optimizing the bialkali antimonide deposition conditions for a wide range of Sb layer thickness, and evaluated their photoemission characteristics and QE lifetime. Proper surface science investigation of the Sb layer was also conducted to understand the role of the deposition parameters on the photocathode performance [36,41,42]. Field emission scanning electron microscopy, x-ray diffraction, and atomic force microscopy were used to evaluate the morphology, porosity and roughness of the Sb-layers with varying thicknesses.

1.7. OUTLINE OF THE DISSERTATION

This dissertation is based on the published work in journals [43-46]. Chapter 2 presents the study measuring the outgassing rates of three nominally identical 304L stainless steel vacuum

chambers to determine the effects of chamber coatings (amorphous silicon and titanium nitride) and heat treatments on reducing the gas load to achieve better vacuum. Chapter 3 presents the study of the effectiveness of titanium nitride thin film applied on photocathode electrodes to eliminate field emission under very high bias voltage. The field emission measurements of three TiN-coated aluminum electrodes are presented and compared to those of bare aluminum electrodes and electrodes manufactured from titanium-alloy (Ti-6Al-4V). Chapter 4 details the photocathode preparation chamber that was designed and built for growing bialkali antimonide photocathodes. Antimony films grown on Ta and GaAs substrates were studied under different vacuum and deposition conditions to better understand growth characteristics and their effects on photocathode QE and lifetime at low voltage. The experimental results on QE and lifetime are correlated with the surface characteristics of antimony films including surface roughness, grain size crystallite size, and porosity. Surface science results from FESEM, XRD, and AFM investigations are presented. Finally, chapter 5 summarizes the main results of this work and offers some future experimental ideas related to the thin films studied here.

CHAPTER 2

EFFECTS OF HEAT TREATMENTS AND COATINGS ON THE OUTGASSING RATE OF STAINLESS STEEL CHAMBERS

2.1. INTRODUCTION

The successful operation of a GaAs-based spin-polarized electron source [18,47] requires vacuum near 1×10^{-12} Torr [ultrahigh vacuum (UHV) to extreme-high vacuum (XHV[3])] since residual gasses in the system are ionized by the electron beam and accelerated into the photocathode, causing damage and limiting the operational lifetime of the system. Proposed accelerator electron sources require higher current and corresponding vacuum improvements. The equilibrium pressure in the system, P, is defined by the equation, $P = Q/S$, where Q is the gas load from all sources including outgassing and leaks, and S is the effective pump speed. To reduce pressure, the pump speed should be maximized and the outgassing rate minimized [48,49]. For stainless steel systems with no leaks and where no process gas is introduced, the gas load is primarily from hydrogen outgassing from the steel [50]. There are numerous reports of successful reduction of the outgassing rate via moderate [51-57] and high temperature [56-63] heat treatments, which serve to reduce hydrogen outgassing. There are also numerous reports of coatings such as titanium nitride (TiN) [64-69], boron nitride [69,70], silicon [71,72], or silicon oxide [73] that may reduce the outgassing rate by acting as diffusion barriers.

Thus, the objective of this individual study was to reduce the outgassing rate (i.e., gas load)

Major content of this chapter is reprinted with permission from M.A. Mamun, A.A. Elmustafa, M.L. Stutzman, P.A. Adderley, and M. Poelker, "Effect of heat treatments and coatings on the outgassing rate of stainless steel chambers," Journal of Vacuum Science & Technology A 32 (2), Mar/Apr 2014, 021604 (8 pages). Copyright 2014, American Vacuum Society.

from the photogun chamber walls to achieve superior vacuum requirement of ultra-bright accelerator electron sources. On this end, outgassing rates have been measured and compared on identical vacuum chambers with and without thin film coatings and as a function of heat treatments to identify their effectiveness in reducing the gas load.

The experimental results presented here reproduce the outgassing rate reduction for moderate heat treatment temperatures of stainless steel and represent the first test of the amorphous silicon coating for baked vacuum chambers. Experimental results presented here for TiN coated chambers replicate the extremely low measured outgassing rates in the literature for TiN coated chambers but with large experimental uncertainty in the measurements, and indication of a potential pump speed in the coating, which would invalidate the accumulation method of measuring outgassing rate.

These experiments were conducted by measuring outgassing from complete vacuum chambers that included welds and flanges to provide an outgassing rate representative of what can be achieved for production vacuum chambers for electron sources at Jefferson Lab. Outgassing rates were measured following each of a series of system bakes and at a range of room temperatures. The room temperature dependence of the hydrogen outgassing rate allows measurement of the activation energy for hydrogen diffusion in the bare steel system and is the basis for the discussion of diffusion versus recombination limitations in the outgassing process.

Scanning electron microscopy (SEM) and surface profilometry were used to determine the topography and mechanical roughness of the coated and uncoated surfaces, and energy-dispersive x-ray spectroscopy (EDS) was used to assess the chemical composition of the coatings.

2.2. EXPERIMENT

2.2.1. Chamber fabrication

Each vacuum chamber, 20.3 cm in diameter and 38.1 cm long, was manufactured from a 304L stainless steel sheet, 0.48 cm thick with a 0.8 μm RMS surface finish that was rolled into a cylinder and welded. A DN200 Conflat™ flange was welded to one end, and a flat plate of the same thickness and material as the walls was welded to the bottom. The chamber was assembled (see Fig. 2.1) with either a zero-length DN200 to DN35 reducer flange, or a custom five-port DN200 adapter flange, thinned to 4.78 mm, with five DN35 ports to support a subsequent experiment. DN35 Conflat™ tees were used to attach a spinning rotor gauge (SRG) [74] and an all-metal right-angle isolation valve (400 °C bakable) to each chamber. Each tee was heat treated and coated identically to the corresponding test chamber, and the dimensions of the tee were included in calculations of the geometric surface area and volume. The additional surface area due to microscopic roughness was not included in calculations of outgassing rate, and the chambers were not electropolished. Chamber volumes and areas were nominally 11.3 L and 3200 cm^2, respectively, with exact dimensions used for each system and uncertainties estimated to be below 2%. After manufacture, all chambers were cleaned with a detergent [75] and solvents, then evacuated and leak checked using a residual gas analyzer (RGA) with a detectable leak threshold below 5×10^{-11} Torr L s^{-1}.

Two chambers were coated immediately following fabrication with either titanium nitride or amorphous silicon and are referred to as TiN and a-Si, respectively. The stainless steel chamber was evaluated initially without any coating, and is referred to as SS1. Following a series of

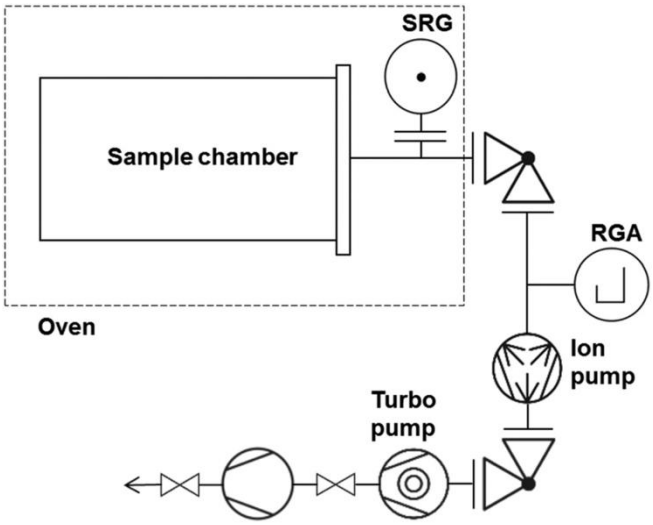


FIG. 2.1. Schematic of the outgassing measurement experimental apparatus during a 400 °C bake showing the chamber, SRG, isolation valve, and pumps. For bakes at lower temperature, the first isolation valve, the ion pump, and the RGA were within the oven.

heat treatments, SS1 was sent to be coated with the a-Si coating and is referred to as SS1:a-Si following the coating process. Additional outgassing data from previously published outgassing measurements of a stainless steel chamber [47] is included as SS2 in Fig. 2.7.

Prior to measuring outgassing rates, all chambers were evacuated and baked in a hot air oven. Following each chamber bake, outgassing rates were evaluated at room temperatures ranging from 15 to 30 °C in a clean room with temperatures stable to within 1 °C. For 400 °C heat treatments, the ion pump and RGA were located outside the oven, and they were baked to at least 150 °C using resistive heat tapes for the duration of the heat treatment, while during bakes at 250 °C and below, the ion pump and RGA were within the hot air oven.

2.2.2. Coating details

The commercial coating SilcoGuardVR -1000 from the vendor SilcoTek Corporation [76] is an

inert multilayered barrier of amorphous silicon interdiffused with the substrate resulting in a 400–800 nm coating. The silicon coating is applied by chemical vapor deposition at approximately 400 °C. The present study was designed to evaluate its potential use in baked systems for UHV and XHV applications.

The TiN coating was provided by Ionbond LLC [77] using cathodic arc physical vapor deposition. The coating was between 9 and 10 μm thick, which is considerably thicker than other coatings in the literature for UHV applications (e.g., those in Refs. 64 and 65, which are between 200 nm and 1 μm).

2.2.3. Outgassing measurement

The rate of rise, or accumulation, technique [78] with the SRG was used to measure the outgassing rate of each test chamber. This technique relies on the measurement of the pressure inside the isolated test chamber as a function of time, dP/dt, with the outgassing rate, q, given by the expression

$$q = \frac{dP}{dt} \times \frac{V}{A} \left(\frac{\text{Torr} \cdot \text{L}}{\text{s} \cdot \text{cm}^2} \right), \tag{2.1}$$

where V is the chamber volume, and A is the chamber surface area. The SRG is a direct reading gauge and was used because it disturbs the vacuum minimally compared to ionization gauges, which can generate a gas load and/or provide a small amount of pumping depending on system pressure. The SRG lower measurement limit is approximately 1×10^{-7} Torr.

Outgassing rates were calculated using pressure measurements obtained over a period of at least 24 h, with typical data shown in Fig. 2.2. Data obtained during the first ~10 h of each

accumulation measurement were disregarded to avoid inaccuracies from temperature stabilization time or equipment warm-up effects. Measurements began from either base chamber pressure, $<10^{-7}$ Torr, or by monitoring the pressure rate-of-rise starting from the pressure at the end of the previous run. Repeated measurements showed the measured outgassing rate was independent of the initial chamber pressure.

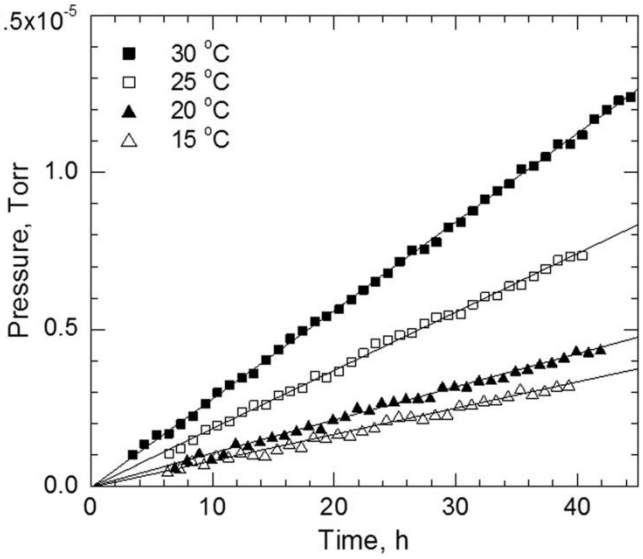


FIG. 2.2. Representative rate-of-rise data at four room temperatures. These data were obtained using the SS1 stainless steel chamber, and correspond to outgassing rates between 1.4×10^{-13} and 5.5×10^{-13} Torr L s^{-1} cm^{-2} following a 150 °C bake (third in the series noted in Table 2.1). A least-square linear fit was used for each data set to calculate outgassing rates.

2.2.4. Coating analysis

Test coupons coated with the TiN coating and the Silco coating were compared to a bare sample of the material used to fabricate the vacuum chambers. A Dektak-3-ST surface profilometer (2.5 μm radius diamond tip stylus, 3 mg tracking force) was used to measure surface roughness, and a JEOL JSM-6060 LV SEM equipped with EDS with a 20 kV electron beam

provided 1000 times magnification to evaluate surface morphology and chemical composition.

2.3. RESULTS

2.3.1. Bare stainless steel

The outgassing rates measured for the SS1 chamber are listed in Table 2.1. The initial bake at 250 °C yielded an outgassing rate of $3.560(\pm0.0005) \times 10^{-12}$ Torr L s^{-1} cm^{-2} (at 20 °C), consistent with previous work at Jefferson Lab [47]. The extended heat treatment of the evacuated chamber at 400 °C in a hot air oven improved the outgassing rate by nearly a factor of 20, also consistent with past observations at Jefferson Lab and elsewhere [47,51–53,79].

TABLE 2.1. Uncoated chamber (SS1) bake history and corresponding outgassing rate at 20 °C.

Bake temperature (°C)	Bake time (h)	Outgassing rate (Torr L s^{-1} cm^{-2})
250	30	$3.560(\pm0.005) \times 10^{-12}$
400	100	$1.79(\pm0.05) \times 10^{-13}$
150	30	$1.01(\pm0.05) \times 10^{-13}$
250	30	$2.79(\pm0.05) \times 10^{-13}$
150	30	$2.16(\pm0.05) \times 10^{-13}$
360	150	$1.00(\pm0.05) \times 10^{-13}$

To determine the effects of venting a chamber for assembly following a 400 °C heat treatment, the chamber was vented to air, re-evacuated, then baked first to 150 °C, and then at 250 °C with the outgassing rate evaluated after each bake. The 150 °C bake reduced the outgassing rate ~40% below that measured following the 400 °C bake. The reduction in outgassing rate due to the

150 °C bake is larger than would be expected due to hydrogen depletion through diffusion during the low temperature bake. Similar behavior seen elsewhere [58,80,81] is postulated to be a result of an oxide-layer diffusion barrier that forms after venting, evacuation and baking. The outgassing rate following the 250 °C bake increased to 2.79(±0.05) × 10^{-13} Torr L s^{-1} cm^{-2}, higher than the rate following either the 400 °C or the 150 °C bake. This behavior has also been reported in the literature [58,82] where it is believed that 250 °C provides sufficient thermal energy to liberate hydrogen atoms from strongly bound defect states. Once liberated, these hydrogen atoms serve to repopulate the reservoir of mobile hydrogen in the chamber walls, resulting in higher outgassing. A subsequent bake at 150 °C did not fully recover the best outgassing rate, but a final heat treatment at 360 °C for 150 h was effective in restoring the outgassing rate to its best measured value of 1.0(±0.5) × 10^{-13} Torr L s^{-1} cm^{-2}, almost a factor of 40 lower than the initial outgassing rate of the system.

The outgassing rates following each bake were measured at room temperatures from 15 to 30 °C, shown on the Arrhenius plot in Fig. 2.3. The variation in outgassing rate with chamber temperature can be used to determine information about the thermally dependent hydrogen diffusion in the system [51,53,65]. The slope of the line in Fig. 2.3 yields the hydrogen diffusion activation energy, E_D, as shown in Eq. (2.2), where $\log A$ is a constant that is correlated to the initial concentration of hydrogen in the material, R is the gas constant, and T is the chamber temperature in Kelvin

$$\log q = \log A - \left(\frac{E_D}{R}\right)\frac{1}{T}. \tag{2.2}$$

For bare stainless steel, the activation energy calculation following the initial 250 °C bake yields

a value of E_D = 60.3 kJ/mol (= 14.4 kcal/mol = 0.63 eV) in agreement with results presented in the literature [51,83]. This will be discussed further in Sec. 2.4.

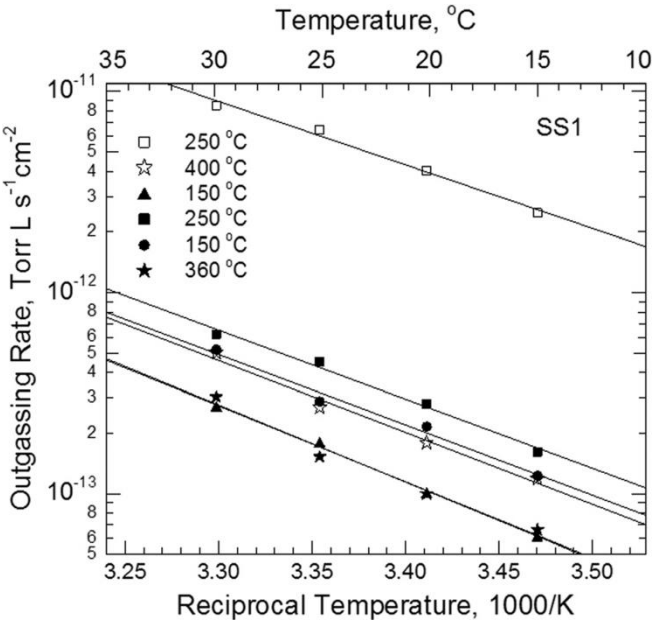


FIG. 2.3. Outgassing rates for the bare stainless steel (SS1) chamber as a function of inverse room temperature, with each data set obtained following a bake at the temperature noted in the legend. The error bars for statistical and systematic errors are smaller than the data points for these data. The slope yields the temperature dependent activation energy as described in the text.

2.3.2. Amorphous Si coating

Amorphous silicon has been investigated as a surface coating to reduce pump-down times for systems in the high to ultrahigh vacuum regime [71,72], but its applicability for baked UHV and XHV applications has not been evaluated. The a-Si chamber was coated prior to any heat treatment, while the SS1:a-Si chamber was coated following the extensive series of bakes and outgassing rate measurements described in Sec. 2.3.1 for the SS1 chamber. The a-Si chamber was first baked at 90 °C, which is largely ineffective for removing water from bare stainless steel. The

outgassing rate following this bake (see Table 2.2) was a factor of two lower than the outgassing rate of the SS1 chamber following its initial 250 °C bake, which indicates that this a-Si coating provides a low outgassing rate following a bake at relatively low temperature.

TABLE 2.2. Amorphous silicon coated (a-Si) chamber bake history and corresponding outgassing rates at 20 °C.

Bake temperature (°C)	Bake time (h)	Outgassing rate (Torr L s^{-1} cm^{-2})
90	30	$2.355(\pm0.005) \times 10^{-12}$
150	30	$2.138(\pm0.005) \times 10^{-12}$
250	30	$1.556(\pm0.005) \times 10^{-12}$
400	100	$3.617(\pm0.005) \times 10^{-12}$
150	30	$2.806(\pm0.005) \times 10^{-12}$
250	30	$1.860(\pm0.005) \times 10^{-12}$

However, subsequent bakes at 150 and 250 °C reduced the outgassing rate for the a-Si chamber only moderately (15 and 30%, respectively). The heat treatment at 400 °C, which was effective in reducing outgassing in the SS1 chamber, instead increased the outgassing rate of the a-Si chamber by a factor of approximately two. This increase could arise from hydrogen diffusion from the steel into the coating during heat treatment, leading to a higher room temperature hydrogen concentration in the coating and resulting in higher outgassing rate, or alternately could be due to changes in the composition of the hydrogen compounds [84] (SiH_x, with x = 1, 2, 3) within the a-Si coating at temperatures above 350 °C. The chamber underwent additional 30 h bakes at 150 °C and then 250 °C. Following this lengthy bake history, the outgassing rate of the silicon-coated chamber was approximately the same as that obtained following the initial 90 °C bake. These results indicate that once a chamber is coated with amorphous silicon, heat

treatments at temperatures up to 400 °C are ineffective at reducing the outgassing rate.

The next series of tests was designed to determine if the amorphous silicon coating would preserve a markedly low outgassing rate. The SS1 chamber that exhibited an outgassing rate of $1.0(\pm 0.5) \times 10^{-13}$ Torr L s^{-1} cm^{-2} was sent for coating with amorphous silicon. After coating, the chamber, now referred to as SS1:a-Si, was solvent cleaned and then baked at 90, 150, and 250 °C, with outgassing rates evaluated and compared to precoating values (see Table 2.3). The 90 °C bake resulted in an outgassing rate of $1.004(\pm 0.005) \times 10^{-12}$ Torr L s^{-1} cm^{-2}, similar to the 90 °C bake of the other a-Si coated chamber. Outgassing rates of 1.26 and $1.46(\pm 0.05) \times 10^{-13}$ Torr L s^{-1} cm^{-2} were obtained following bakes at 150 and 250 °C and increases of 26% and 46%, respectively, over the prior outgassing rate, which is significantly smaller than the ~280% increase in the bare steel outgassing rate following its 250 °C bake (fourth in the series).

The results from both of the a-Si chambers suggest the coating is hydrophobic compared to bare stainless steel, with outgassing rates in the low 10^{-12} Torr L s^{-1} cm^{-2} range obtained

TABLE 2.3. Chamber coated with amorphous silicon following heat treatment (SS1:a-Si) bake history and corresponding outgassing rate at 20 °C. The outgassing rate of SS1 prior to coating with a-Si was 1×10^{-13} Torr L s^{-1} cm^{-2}.

Bake temperature (°C)	Bake time (h)	Outgassing rate (Torr L s^{-1} cm^{-2})
90	30	$1.004(\pm 0.005) \times 10^{-12}$
150	30	$1.26(\pm 0.05) \times 10^{-13}$
250	30	$1.46(\pm 0.05) \times 10^{-13}$

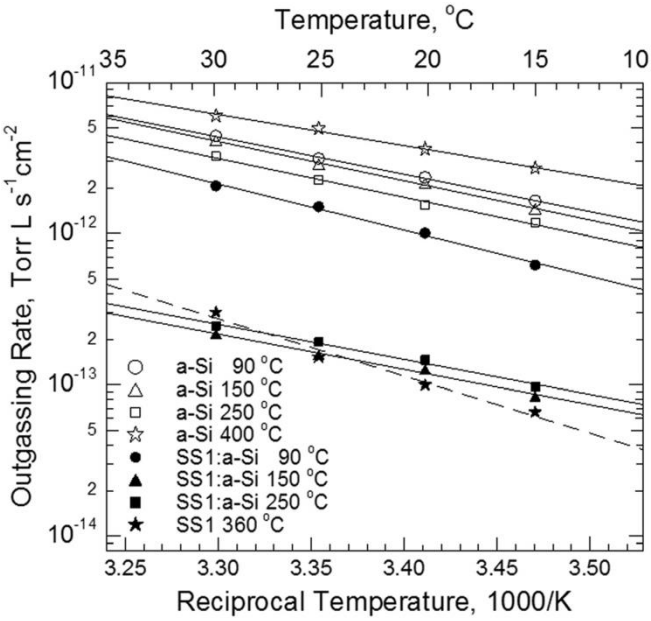


FIG. 2.4. Outgassing rates for the a-Si and the SS1:a-Si chambers as a function of inverse room temperature, with each data set obtained following a bake at the temperature noted in the legend. The low outgassing rate of the heat treated SS1 chamber (solid stars) was largely preserved following coating the chamber with a-Si and baking. The error bars for statistical and systematic error are comparable in size to the data points shown for these data.

following bakes at only 90 °C. The results also indicate that once the chamber has been coated with amorphous silicon, additional heat treatment does not reduce the outgassing rate; however, a chamber that was heat treated prior to coating preserves the reduced outgassing rate following coating much better than uncoated steel.

The outgassing rates of the amorphous silicon-coated chambers were evaluated at a series of room temperatures (Fig. 2.4), and the decrease in outgassing rate with reduced temperature illustrates expected behavior associated with outgassing due to a thermally dependent outgassing rate.

2.3.3. TiN coating

The initial outgassing rate for the TiN coated chamber, measured following a 90 °C bake,

yielded an excellent outgassing rate of $6.44(\pm 0.05) \times 10^{-13}$ Torr L s^{-1} cm^{-2}, which is lower than stainless steel following repeated 250 °C bakes, such as found in Ref. 47. The next three bakes in the series (150, 250, and 400 °C) had outgassing rates measured at various room temperatures, but these data did not follow the expected room temperature dependence. This is believed to be due to a leak in the isolation valve, so these data have been disregarded. After replacement of the isolation valve, a remarkably low outgassing rate of $4(\pm 2) \times 10^{-15}$ Torr L s^{-1} cm^{-2} was obtained following the 150 °C bake (fifth in the series shown in Table 2.4), and this value decreased to $2(\pm 20) \times 10^{-16}$ Torr L s^{-1} cm^{-2} following the final bake at 250 °C. The room temperature dependence of these data sets followed the expected trend for thermally dependent outgassing behavior, with a decreased room temperature leading to a decrease in outgassing rate (see Fig. 2.5).

These remarkably low outgassing rates, though similar to some published values (5.3×10^{-15} and 1×10^{-16} Torr L s^{-1} cm^{-2} from Refs. 65 and 68, respectively), require scrutiny. The pressure within the TiN chamber remained near the bottom of the SRG measurement capability for days (pressure $\sim 10^{-7}$ Torr). Repeated measurements of the outgassing rate for times up to 200 h reduced the statistical error in the measurements, but still lead to statistical and systematic error bars with magnitude similar to, or larger than, the measured value of the outgassing rate. If the pressure in the system were below the measurement capability of the SRG, the calculated outgassing rate could be dominated by a baseline drift of the gauge, though the noted room temperature dependence lends credibility to the measurements. It also must be noted that any pump speed in the system invalidates outgassing rate measurements because the accumulation method applies only to systems with no pumping. Elemental titanium is known to be effective in

pumping gases such as hydrogen, and the presence of such pumping would yield an artificially low outgassing rate: it would require only 0.003 L/s pump speed and a typical

TABLE 2.4. Titanium nitride coated chamber (TiN) bake history and corresponding outgassing rate at 20 °C. Outgassing rates may be artificially low if there is any pump speed in the system, and the inhomogeneity found in the EDS analysis suggests the presence of some elemental Ti.

Bake temperature (°C)	Bake time (h)	Outgassing rate (Torr L s^{-1} cm^{-2})
90	30	$6.44(\pm0.05) \times 10^{-13}$
150	30	not reliable
250	30	not reliable
400	100	not reliable
150	30	$4(\pm2) \times 10^{-15}$
250	30	$2(\pm20) \times 10^{-16}$

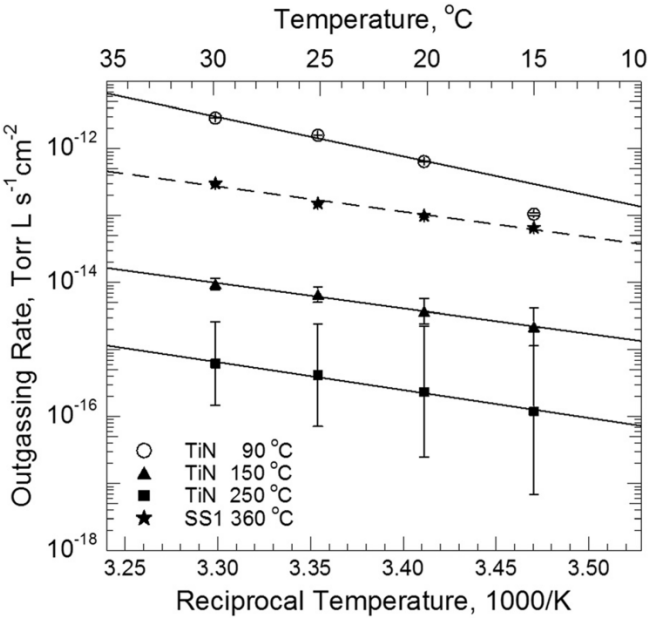


FIG. 2.5. Outgassing rates for the TiN-coated stainless steel chamber as a function of inverse room temperature, with each data set obtained following a bake at the temperature noted in the legend. The best outgassing rate for the SS1 bare stainless steel chamber is plotted for reference. Systematic and statistical errors, though small at larger outgassing rates, become significant at the lowest measured outgassing rates.

outgassing rate of 1×10^{-12} Torr L s^{-1} cm^{-2} to achieve apparent outgassing rates such as those found in this system. A recent study reported by Marcy *et al*. [85] supports this small pump speed hypothesis which was evidenced by the observed four orders of discrepancy between the expected and measured base pressure in the TiN coated system.

2.3.4. Coating analysis

Coating analysis was performed on one bare and two coated test coupons, all cut from the same material as the chambers, and with two coated by the manufacturers using the same parameters as during the test chamber coating processes. The bare stainless steel sample had an RMS roughness of 740 nm and the SEM image of this surface [Fig. 2.6(a) inset] shows characteristic roughness of a machined stainless surface as expected. Application of the a-Si coating served to smooth the surface, with 250 nm RMS roughness, and the SEM image of the coating appeared very uniform [Fig. 2.6(b) inset]. The application of the TiN coating also served to smooth the bare stainless steel surface, with 510 nm RMS roughness, but the SEM image [Fig. 2.6(c) inset] shows obvious particulate matter on the surface. The particulate was also notable in the TiN coated chamber and was easily dislodged during handling, particularly after the bake. The surface roughness and coating thicknesses are summarized in Table 2.5 for bare, a-Si, and TiN surfaces.

The EDS measurements made in conjunction with the SEM images illustrate the chemical composition of the three coated chambers (see Fig. 2.6). The EDS spectrum from the bare stainless steel coupon [Fig. 2.6(a)] shows the expected composition of 304L steel, with an additional carbon peak attributed to residual solvents from cleaning. The a-Si coated test coupon [Fig. 2.6(b)] shows

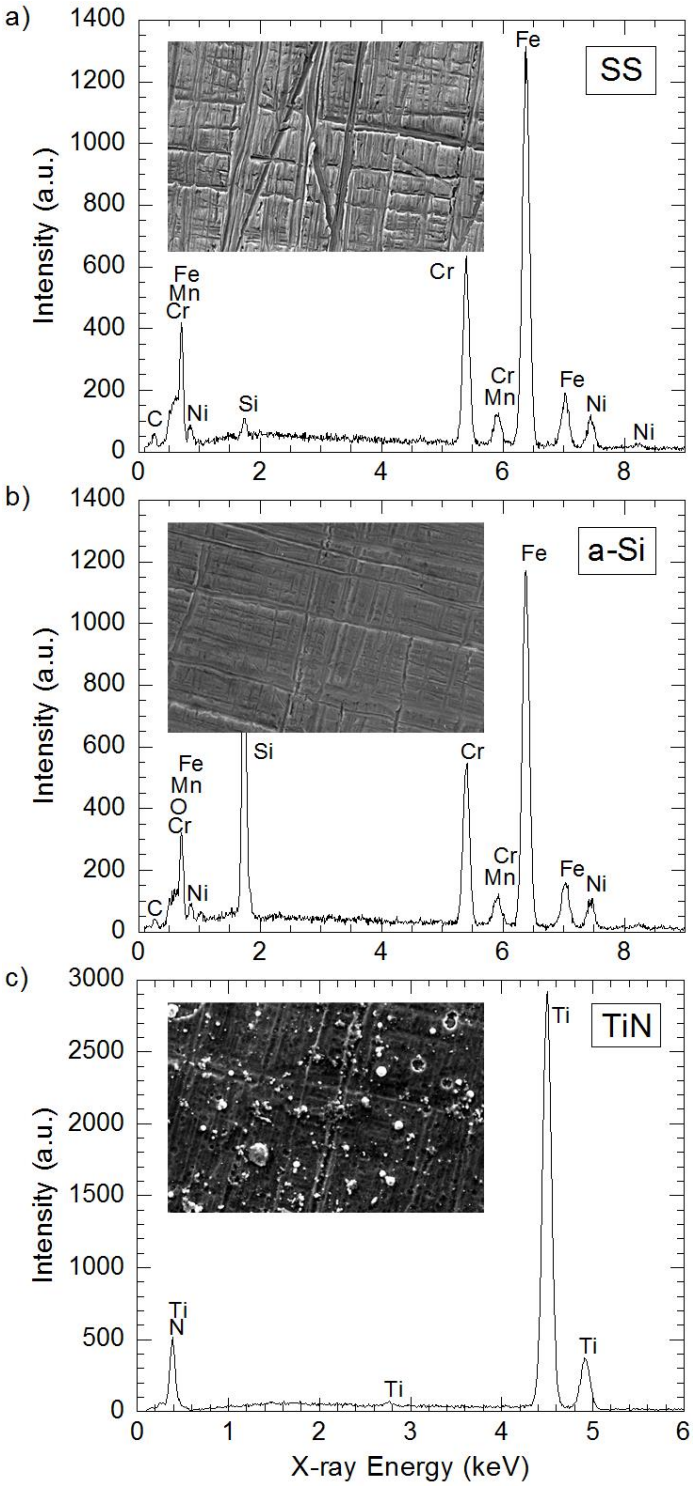


FIG. 2.6. EDS and SEM data show coating composition and morphology for (a) bare stainless steel, showing expected composition and morphology, (b) a-Si on stainless steel, with a Si peak evident in conjunction with the steel substrate, and (c) TiN coating with approximately 1:1 atomic ratio of Ti and N, but obvious particulate matter and pores visible across the surface. Inset SEM images each show a 120 μm × 80 μm area.

TABLE 2.5. Coating thickness and RMS roughness values for bare steel, TiN coated and a-Si coated test samples.

Sample	Coating thickness	RMS roughness (nm)
SS	None	740
a-Si	800 nm	250
TiN	10 μm	510

strong peaks for both the underlying stainless steel and the silicon coating, consistent with the thin, interdiffused silicon coating and the EDS technique, which is sensitive to the first ~1 μm of material. The EDS analysis of TiN [Fig. 2.6(c)] shows Ti and N peaks with an atomic ratio of approximately 1:1 (50.4% N and 49.6% Ti). However, careful EDS examination of smaller features in the TiN coating show inhomogeneity in the film, with Ti:N atomic ratios ranging from 0.58:1 to 1.17:1, suggesting the possible presence of elemental Ti in some areas. The TiN coating is much thicker than the a-Si coating (9 μm compared to 0.8 μm); thus, the surface sensitive EDS measurements show minimal characteristics of the underlying stainless steel substrate.

2.4. DISCUSSION

The outgassing rate of a newly manufactured stainless steel vacuum system is initially governed by the rate at which hydrogen atoms diffuse through the chamber walls to the surface, where the concentration is depleted due to outgassing of hydrogen into the vacuum. This process, known as diffusion limited outgassing, is described by Fick's diffusion equation. However, as the hydrogen concentration is reduced through repeated bakes or extended heat treatment, less hydrogen arrives at the surface per unit time due to diffusion. Eventually, the rate at which

hydrogen atoms at the surface combine and desorb as H_2 molecules, known as recombination, becomes the dominating factor in the outgassing rate of the material rather than the diffusion rate to the surface [50,83,84,86,87].

Qualitatively, the transition from diffusion to recombination limited outgassing behavior can be seen on a graph of the outgassing rate as a function of heat treatment. The combination of time and temperature associated with a chamber's heat treatments can be described using the dimensionless Fourier number, F_0

$$F_0 = 4D_H\left(\frac{t}{d^2}\right), \tag{2.3}$$

where t is the processing time and d is the thickness of the chamber wall. The temperature dependent diffusion constant, D_H, in Eq. (2.3) is related to the hydrogen diffusion activation energy in stainless steel, E_D, by the following expression:

$$D_H(T) = D_0 \exp\left(\frac{-E_D}{RT}\right), \tag{2.4}$$

where D_0 is termed the pre-exponential diffusion constant and assigned [88] a typical value of 0.012 cm^2s^{-1} for 304 L stainless steel, R is the ideal gas constant, and T corresponds to temperature in Kelvin. The value of $E_D =$ 60.3 kJ/mol, determined in Sec. 2.3.1 for diffusion of hydrogen in bare steel after the initial 250 °C bake where bulk diffusion dominates the outgassing process, was used to determine $D_H(T)$ and F_0 for all systems.

The outgassing rate of each test chamber is plotted versus F_0 in Fig. 2.7. The straight line in Fig. 2.7 shows the modeled outgassing rate of a vacuum chamber based solely on diffusion per Fick's Law, yielding a straight line on a log scale, with outgassing rate falling continuously with

increasing F_0.

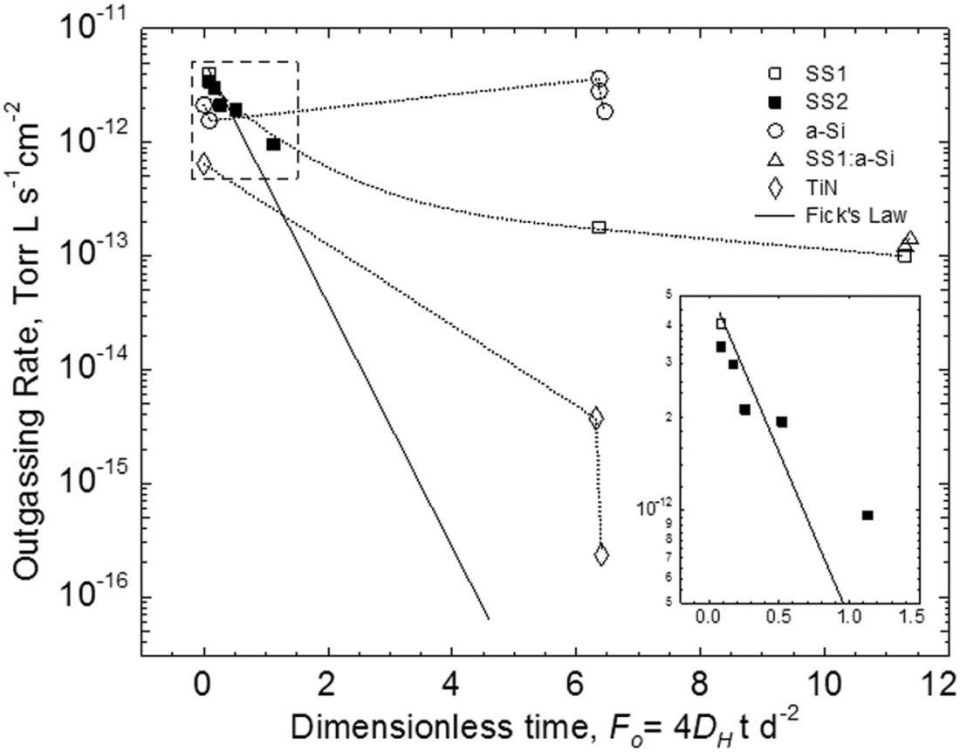


FIG. 2.7. Outgassing rates for each chamber are plotted vs the Fourier number, F_0. The straight line represents the calculated outgassing rate for the systems using Fick's law, disregarding surface effects. For the steel chambers, the transition from diffusion limited reduction in outgassing rate to recombination limited behavior occurs near $F_0 = 1$, with the outgassing rates vs F_0 in close agreement with Fick's law at low F_0 (see inset), and diverging from Fick's law toward recombination limited behavior at higher F_0 values. The a-Si chambers have outgassing rate largely independent of F_0 suggesting that the surface effects of the system dominate the outgassing, and diffusion of hydrogen from the material during bakes is not significant. The steep slope of the TiN indicates either an excellent diffusion barrier or a slight pumping speed in the coating that increases with additional heat treatment. Note: data labeled SS2 is from previously published data (Ref. 47).

The data for bare stainless steel support two regimes of outgassing. Initial bakes at 250 °C on the SS1 chamber and previously published data [47] (labeled as SS2 in Fig. 2.7) yield outgassing rates in good agreement with Fick's law for $F_0 < 1$ (see Fig. 2.7 inset). However, for $F_0 > 1$, the outgassing rates deviate from Fick's law, indicating that the outgassing rate has undergone the

expected transition to recombination limited behavior, with surface effects, rather than diffusion, dominating the outgassing rate process.

For the a-Si chamber, the graph of q versus F_0 shows comparatively flat behavior. Recombination limited systems (such as the stainless steel chambers at $F_0 >> 1$) exhibit little change in q versus F_0, suggesting that the outgassing rate for the a-Si chamber is strongly dominated by surface effects rather than by the rate of diffusion of hydrogen in the bulk stainless steel. The SS1:a-Si chamber was not heated to 400 °C following coating in order to preserve a known low outgassing rate for future experiments, and although the data are shown in the graph, dependence on F_0 is not clear from the limited data set.

The slope of the TiN outgassing rates versus F_0 is quite steep, with the outgassing rate falling faster than Fick's law predicts due to diffusion from steel. Two possible explanations exist: either this TiN coating is an excellent diffusion barrier for hydrogen, and the bakes at even 90 and 150 °C are sufficient to deplete the hydrogen from the TiN coating itself, yielding exceptionally small outgassing rates, or alternatively the TiN coating may have a small pump speed, and the pump speed increases with additional heat treatments. Marcy *et al*. [85] conducted a complementary experiment by using the TiN coated chamber, pumped by nonevaporable getter and ion pumps, to determine if the low apparent outgassing rate yields a markedly lower base pressure compared to that obtained using a bare stainless steel chamber. The measured outgassing rate from their investigation appeared to be four orders higher than the expected outgassing rate which indicates the small pump speed of TiN coating due to presence of elemental titanium in the coating.

2.5. SUMMARY

These studies used a bare stainless steel chamber to verify prior results and to validate the experimental setup for outgassing rate measurements of coated chambers. A 100 h bake at 400 °C reduced the outgassing rate of a bare stainless steel vacuum chamber from $3.560(\pm0.005) \times 10^{-12}$ to $1.79(\pm0.05) \times 10^{-13}$ Torr L s^{-1} cm^{-2}. Subsequent bakes were far less effective at reducing the outgassing rate, indicating a transition from diffusion limited to recombination limited outgassing behavior. Following venting to air and rebaking at 150 °C bake, the outgassing rate decreased modestly, but following a 250 °C bake, the outgassing rate increased by nearly a factor of 3 (from 1.01 to $2.79(\pm0.05) \times 10^{-13}$ Torr L s^{-1} cm^{-2}). These studies suggest that once low outgassing rates have been achieved, baking a stainless steel vacuum chamber at 250 °C in the recombination limited regime is detrimental to the outgassing rate.

This is the first investigation of the performance of amorphous-silicon coated chambers subjected to repeated bake cycles and heat treatments. The a-Si chamber had an outgassing rate of $2.355(\pm0.005) \times 10^{-12}$ Torr L s^{-1} cm^{-2} following a 90 °C bake, which can typically only be reached with a 250 °C bake of a bare steel chamber, and is consistent with the hydrophobic nature of the surface advertised by the manufacturer. However, subsequent bakes at 150 and 250 °C reduced the outgassing rate minimally, and the extended heat treatment at 400 °C increased the rate above the initial value obtained following the 90 °C bake, leading to the conclusion that heat treatment following coating is not effective in reducing the outgassing rate for a-Si coated chambers. Low outgassing rates were preserved for the chamber coated with a-Si after heat treatment (SS1:a-Si), indicating that coating a degassed chamber with a-Si can be beneficial for

systems where a low outgassing rate is needed. Energy-dispersive x-ray spectroscopy data confirm the expected combination of silicon and 304 L stainless steel in the spectrum.

The test results of the TiN coated chamber yielded the smallest outgassing rate of all the chambers: $6.44(\pm 0.05) \times 10^{-13}$ Torr L s^{-1} cm^{-2} following an initial 90 °C bake and $2(\pm 20) \times 10^{-16}$ Torr L s^{-1} cm^{-2} following the final bake in the series. The pressure, as measured by the SRG, remained at values near the gauge's measurement limit throughout the accumulation measurement. Thus, the uncertainty in the TiN outgassing rate is large and cannot preclude a small pumping effect of the TiN coating.

2.6. CONCLUSION

The operating lifetime of a photocathode within a DC high voltage photogun is limited by vacuum, which is determined in part by the outgassing rate of hydrogen from the vacuum chamber walls. By reducing the outgassing rate, the vacuum level improves proportionally and similarly, the operating lifetime of the photocathode. This individual study investigated thin films of a-Si and TiN applied to surfaces of the vacuum chambers to reduce the outgassing rate for achieving superior vacuum. Results from this study suggests that a-Si coating on a bake chamber can permanently retain the low outgassing rate of a photogun vacuum system and can eliminate further high temperature bakes if the system needs to be vented to air. This study also suggests that TiN coating seemed to act as a small pump, which can improve vacuum when degassed with heat treatment. Thus, these two films can be employed effectively to lower the gas load and retain the improved vacuum to meet the stringent vacuum requirement of the next generation ultra-bright accelerator electron sources.

CHAPTER 3

TIN COATED ALUMINUM ELECTRODES FOR DC HIGH VOLTAGE ELECTRON GUNS

3.1. INTRODUCTION

Particle accelerators are important tools used in many applications ranging from cancer therapy and industrial linear accelerators and synchrotron light sources, to high energy colliders that are used to investigate nature's fundamental building blocks and forces. The performance of many present and future particle accelerators is limited by the maximum operating voltage supported by the direct current (DC) high voltage (HV) photoelectron gun that provides the electron beam for the accelerator. Too often, the operating voltage of the photogun is limited by field emission from the cathode electrode, which degrades vacuum via electron stimulated desorption, leading to reduced photoelectron yield (or quantum efficiency, QE) via ion bombardment. At high levels (>1 μA), field emission can open flange joints and damage high voltage insulators. Cathode electrodes for electron guns are typically manufactured from physically hard metals like stainless steel, titanium, and molybdenum [19,89-91]. Table 3.1 lists common electrode materials, with relevant properties. Once fabricated at the machine shop, the relatively rough surface of the electrode must be mechanically polished by hand using silicon carbide paper and diamond grit, to obtain a smooth surface free of protrusions [28]. This is a time-consuming and labor-intensive process. At least one photogun group has implemented

Major content of this chapter is reprinted with permission from M.A. Mamun, A. A. Elmustafa, R. Taus, E. Forman, and M. Poelker, "TiN Coated Aluminum Electrodes for DC High Voltage Electron Guns," Journal of Vacuum Science & Technology A 33 (3), May/Jun 2015, 031604 (10 pages). Copyright 2015, American Vacuum Society.

electropolishing as a means to speed electrode preparation [31,102]; however, our recent tests indicate electropolished electrodes do not respond to gas conditioning as favorably as mechanically polished electrodes [103,104]. Niobium electrodes perform well at a high voltage when surfaces are etched with a mixture of strong acids—a technique known as buffered chemical polishing (BCP) [92]. The BCP process significantly reduces electrode preparation time but not everyone has access to BCP facilities.

Another important consideration is effective heat removal from the photocathode during high current applications. Only a small portion (few percent) of absorbed laser light produces the desired electron beam. Most of the light simply serves to heat the photocathode and cathode electrode. For high current applications, where many watts of laser light are required, it is important to maintain the photocathode at temperatures below some limit to ensure that the photocathode does not decompose. Hence, the heat must be removed, which is a complicated task because the cathode is biased at high voltage. Passive heat removal is preferred.

TABLE 3.1. Relevant characteristics of candidate electrode materials at room temperature.

Material	Work function φ (eV)	Thermal conductivity (W/m-K)	Electrical resistivity $\mu\Omega$ cm	Hardness (GPa)	Elasticitymodulus (GPa)	Density (g/cc)
SS316L	4.5 (Ref. 92)	16.3 (Ref. 93)	74 (Ref. 90)	1.5 (Ref. 93)	193 (Ref. 93)	8.0 (Ref. 93)
Niobium	4.3 (Ref. 94)	52 (Ref. 95)	14 (Ref. 95)	1.3 (Ref. 95)	104 (Ref. 95)	8.6 (Ref. 95)
Molybdenum	4.6 (Ref. 94)	142 (Ref. 95)	5.7 (Ref. 95)	2.2 (Ref. 95)	310 (Ref. 95)	10.9 (Ref. 95)
Ti-6Al-4V	4.5 (Ref. 19)	6.7 (Ref. 96)	178 (Ref. 96)	3.4 (Ref. 96)	114 (Ref. 96)	4.4 (Ref. 96)
Al6061	3.5 (Ref. 97)	167 (Refs. 96 and 98)	4 (Refs. 96 and 98)	1.47[a]	70[a]	2.7 (Refs. 96 and 98)
TiN coating	5.0 (Ref. 99)	11-67 (Ref. 100)	14 (Ref. 100), 270 (Ref. 101)	18.2[a]	270[a]	3.3 (Ref. 100)

[a]Properties of ion-beam enhanced deposition grown TiN coating on Al were measured in the present work.

Bare aluminum is not considered a good candidate material for high voltage electrodes. Bare aluminum electrodes—with soft, porous, and oxidized surfaces—exhibit high levels of field emission at modest voltages and field strengths, as we illustrate below. However, aluminum is easy to machine and polish, and it provides a high degree of thermal conductivity, which could be exploited for passive heat removal from the photocathode, for high current applications. Thus, the goal of this individual study was to find a suitable thin film that can be applied on aluminum electrodes to improve their field emission suppression capacity to meet the very high voltage requirement of future ultra-bright accelerator electron sources. The objective of this work was to evaluate the high voltage performance of bare aluminum electrodes coated with titanium nitride, a commercially available coating commonly used to harden the surface of metals, and with significantly higher work function compared to other materials. On this end, the performance of three TiN-coated aluminum electrodes was compared to that of bare aluminum electrodes, and electrodes manufactured from titanium-alloy (Ti-6Al-4V). The titanium-alloy electrodes provide a benchmark-level of performance, representative of mechanically polished electrodes prepared in a traditional manner with silicon-carbide paper and diamond paste polishing (DPP) compound.

As presented below, the TiN-coated aluminum electrodes performed significantly better than bare aluminum electrodes, and exhibited performance comparable to the Ti-alloy electrodes. All of the TiN-coated aluminum electrodes reached —225 kV with cathode/anode gap of 50 mm without measureable field emission (<10 pA), following gas conditioning using helium. The best TiN-coated aluminum electrode exhibited less than 100 pA of field emission at 22.5 MV/m.

The Fowler–Nordheim theory of field emission suggests that smooth electrode surfaces, made of materials with a large work function, exhibit smaller levels of field emission. However, in practice, few people use the Fowler–Nordhiem theory to predict the onset of field emission from individual test samples. It is not uncommon for nominally identical electrodes to exhibit markedly different performance. Part of the problem in predicting the performance of an electrode is that DC field emission involves a complex mixture of macroscopic and microscopic effects, which are determined by the geometry, metallurgy, and surface preparation techniques which can introduce contamination. In this work, gas conditioning was implemented as a means of process control [27] to minimize the variability of results between nominally identical electrode samples, and to provide a significantly more reliable assessment of high voltage performance. For most of the work reported here, helium was used for gas conditioning, but when stubborn field emitters were encountered, krypton gas was sometimes used.

Excessive field emission often leads to permanent damage on the electrode surface. Therefore, the surface topography of each electrode was investigated at every step of the polishing process, the coating process, and following each step of the high voltage evaluation, using a JEOL JSM-6060 LV scanning electron microscope (SEM). In addition, the surface roughness of the aluminum electrode was inferred based on measurements of small test coupons (2 cm × 2 cm × 0.5 cm), before and after TiN coating, using a Digital Instruments Dimension 3100 atomic force microscope (AFM) in the tapping mode. It was anticipated that a harder electrode surface was less prone to surface damage due to handling and HV processing. Thus, the mechanical properties of the TiN coating, hardness and modulus, were evaluated using nanoindentation measurement and compared to those of stainless steel, niobium, and titanium-alloy coupons. A

Nanoindenter XP from Agilent Technologies (Agilent Technologies, Inc., Santa Clara, CA) equipped with a three-sided diamond Berkovich indenter tip was employed to test the coupons in the continuous stiffness measurement (CSM) protocol.

3.2. EXPERIMENT

3.2.1. Apparatus

A total of seven electrodes were evaluated: two bare aluminum electrodes, three TiN-coated aluminum electrodes, and two Ti-alloy electrodes. Two of the TiN-coated aluminum electrodes were first evaluated in the uncoated state. Each electrode had a Pierce-type geometry with 25° focusing angle (6.35 cm diameter, 2.85 cm thick) [Fig. 3.1(a)], identical to electrodes used at the continuous electron beam accelerator facility for many years [14]. A piece of polished stainless steel was used in place of the GaAs photocathode.

Electrodes were evaluated using two vacuum test chambers TS1 and TS2 [Figs. 3.1(b) and 3.1(c)], identical in function but with different vacuum pumping technology. One chamber (TS1) relied on nonevaporable getter pump (SAES GP500) and a 220 l s^{-1} ion pump. After installing a test electrode, the entire vacuum chamber was baked at 200 °C for 30 h to eliminate water from the vacuum chamber and provide partial activation of the nonevaporable getter pump.

The base pressure inside the test chamber was $\sim 1 \times 10^{-11}$ Torr (1.33×10^{-9} Pa) during electrode evaluation. The other test stand (TS2) was pumped using a cryopump (CTI, 2000 l s^{-1} rated pumping speed) and 50 l s^{-1} ion pump. An electrode was installed, the system was pumped using a small turbo, and then the valve to the cryopump opened. The system was allowed to pump

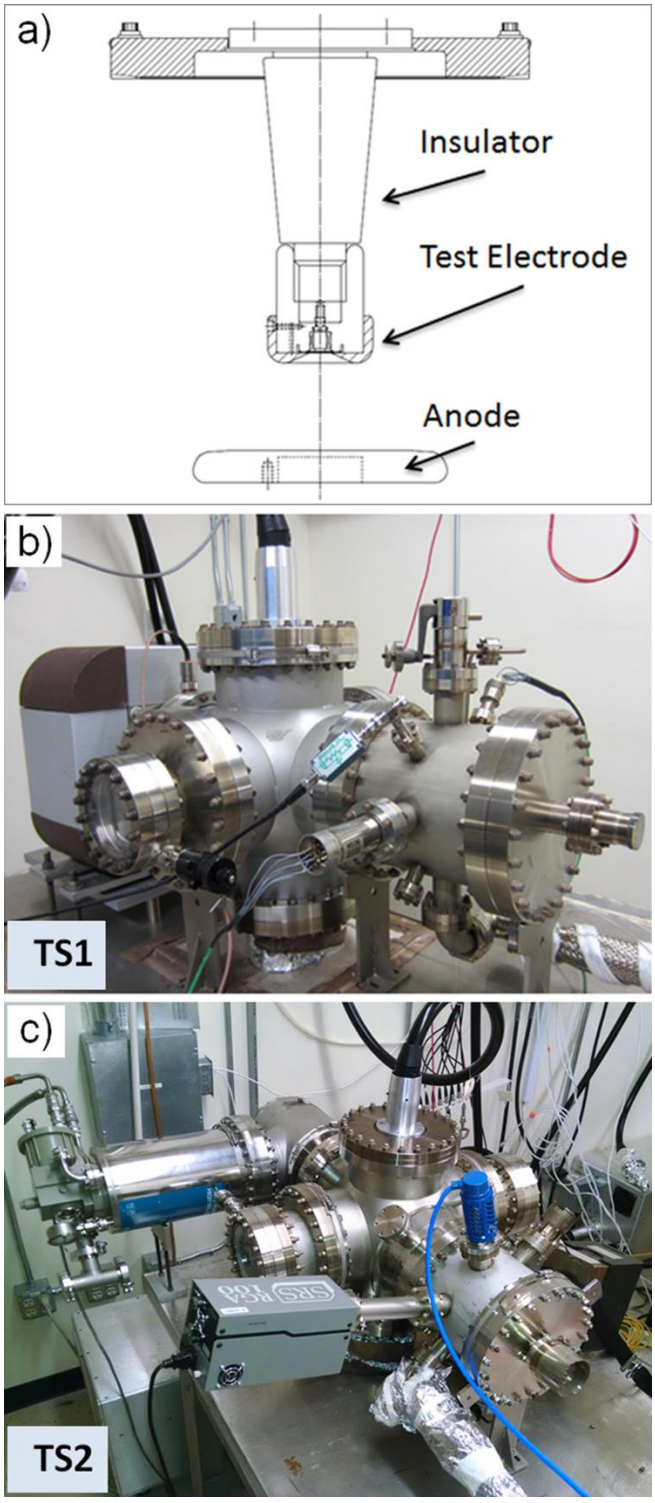


FIG. 3.1. (a) Schematic of the insulator, test electrode and anode used to collect the field emission. Photographs of the dc high voltage field emission test stands—(b) baked chamber TS1 and (c) unbaked chamber TS2 used to evaluate each cathode electrode.

overnight. The next day, the electrode was heated to 200 °C for 8 h using a smaller heater inserted into the tapered opening of the high voltage insulator to liberate loosely bound adsorbed gasses from the insulator and electrode surfaces. The base pressure in this test stand during electrode evaluation was typically ~1×10^{-10} Torr (1.33×10^{-8} Pa). A comparison of the field emission characteristics of three electrodes evaluated in both test stands indicated that field emission results were independent of the vacuum test chambers as long as the vacuum preparation protocols and degassing of the electrodes were conducted in a consistent manner for each chamber.

Details of the test apparatus can be found in Ref. 92; an abbreviated description is provided here. Cathode electrodes were suspended from a tapered conical insulator that extended into each test chamber (Fig. 3.1). The anode was made from a stainless steel (304L) flat plate with a Rogowski edge profile, polished using 600 grit silicon carbide paper, electrically isolated from ground and attached to a sensitive current meter (Keithley electrometer model 617). The anode could be moved up or down to vary the cathode/anode gap and therefore the field strength. Further details of the cathode electrodes geometry, gap separation, and maximum field strength can be found in Ref. 92.

A —225 kV commercial high voltage power supply was used for the experiment. The high voltage power supply and the ceramic insulator accommodate "industry standard" high voltage cables with R-28 connectors. A 100 MΩ conditioning resistor was placed in series with the cathode electrode via an oil tank and served to protect the apparatus in case of sudden discharge of stored energy. The resistor also serves to protect the electrode via a negative feedback mechanism— as

current increases, a larger voltage drop occurs across the resistor, reducing voltage at the electrode.

An assessment of the field emission properties of each test electrode involved monitoring vacuum level inside the apparatus, x-ray radiation near the apparatus, and anode current while increasing the voltage applied to the cathode electrode. High voltage was first applied to the electrode using the largest cathode/anode gap of 50 mm. Upon successful high voltage processing (defined below), the gap could be decreased to achieve higher field strength. However, small gaps sometimes produced catastrophic breakdown and electrode damage, so small gap evaluation was approached with caution and only if very little field emission was observed at a larger gap of 20 mm.

Electrodes were first evaluated under the best vacuum conditions each vacuum chamber could possibly provide. Voltage was applied to the electrode and was gradually increased while maintaining the anode current less than ~100 nanoamperes (nA). As the voltage was increased, field emission would be observed, and sometimes field emission sites would "burn off," as evidenced by lower levels of current measured at the anode. Frequently, stubborn field emitters were encountered, and gas conditioning was employed [19]. Gas conditioning involved introducing helium into the vacuum chamber at pressure between 1×10^{-6} and 1×10^{-4} Torr (1×10^{-4} to 1×10^{-2} Pa), while the cathode electrode was biased at a voltage high enough to produce significant levels of field emission (approximately few μA). Under these conditions, the inert gas can be ionized by the field emission and these ions are then attracted to the negatively biased cathode electrode, bombarding the electrode in the vicinity of the field emitter. Recent work has revealed that field emission sites are eliminated via two mechanisms [27]: sputtering

and ion implantation, which serves to increase the localized work function. Gas conditioning typically was performed for 30–60 min and repeated multiple times, depending on the performance of the test electrode in the field emission reduction process. An electrode was considered fully processed when field emission current was stable to within a few percent of the average value. Specific details on how to implement gas conditioning are given in Refs. 27 and 92. During gas conditioning, ion pumps were not energized, and the valve to the cryopump was closed. Nonevaporable getter pumps do not pump inert gas. An overboard turbo pump was used to remove the gas from each system during gas conditioning and for approximately 30 min once the supply of gas was terminated. The pressure inside the vacuum chamber typically recovered to nominal static vacuum level in just 24 h.

3.2.2. Polishing and preparing the electrodes

Two electrodes were manufactured from Ti-6Al-4V titanium alloy, and represent the "hard metal" benchmark for comparing the performance of "soft metal" aluminum and TiN-coated aluminum electrodes. The Ti-alloy electrodes were cut to shape using hydrocarbon-free lubricants, and polished on a potter's wheel with silicon carbide paper of increasingly finer grit (300 and then 600 particles/in.^{2}) followed by polishing with diamond grit (6, 3 μm), to obtain a mirror-like finish. Between each polishing step, the electrodes were cleaned in an ultrasonic bath using a detergent alkali solution. After mechanical polishing, the electrodes were high-pressure rinsed (1200 psi) for 20 min with ultrapure deionized water with resistivity >18 MΩ cm.

Aluminum electrodes were manufactured from Al6061-alloy. After being cut to shape with hydrocarbon-free lubricants, each electrode was polished on a potter's wheel with silicon carbide

paper of increasingly finer grit: 400, 600, and 800 particles/in.^{2}. Two electrodes were further polished using 1200 particles/in.^{2} paper (a minor goal was to determine if polishing with 1200 grit paper was necessary). Polishing with silicon carbide paper produced a mirror-like, submicron surface finish. Between each polishing step, the electrodes were cleaned in an ultrasonic bath of acetone and then methanol. Aluminum electrodes required only hours of mechanical polishing using silicon carbide paper, compared to weeks of polishing time for relatively harder materials like stainless steel and titanium alloy.

Two bare aluminum electrodes were tested at high voltage. Afterwards these electrodes received additional polishing to remove defects introduced as a result of field emission and gas conditioning, as described below in Sec. 3.3.1. A total of three bare-aluminum electrodes were then sent to the commercial vendor Beam Alloy Technology LLC for coating with titanium nitride, using an ion-beam enhanced deposition process at low temperature (<93 °C) [105]. According to the vendor, the independently controlled ion beam provides precise control of film growth, and results in a tight metallurgical bond between the coating and the substrate material. The coating thickness was controlled to 2.5 μm. Upon return, the electrodes were cleaned in an ultrasonic bath of methanol.

3.3. HIGH VOLTAGE TEST RESULTS

The evaluation of seven test electrodes at high voltage required several months of effort. Similar to past studies [27,92], it was not uncommon to observe completely different field emission behavior from nominally identical test samples, upon the first application of high voltage. The variability in results associated with initial high voltage processing of electrodes of

the same material and treatment was attributed to undetectable levels of contamination and/or subsurface variations from sample to sample. Credible results were typically obtained subsequent to gas conditioning, which represented an important aspect of the process control. With some exceptions, most of the results presented below represent post-gas conditioning results.

In Fig. 3.2, field emission current for a subset of the electrodes is plotted versus the applied voltage and field strength. The error bars represent one standard deviation in this figure. The field strength for each gap setting was estimated using the electrostatic field mapping program POISSON [105]. Field strength values required to produce 100 pA of field emission for different cathode/anode gaps and for all electrodes are shown in Table 3.2. All values correspond to performance following gas conditioning, with the exception of titanium-alloy sample 2, which exhibited small levels of field emission without gas conditioning. Entries with greater-than sign (>) indicate the electrode did not produce 100 pA of field emission for that gap setting.

TABLE 3.2. Field strength required to produce 100 pA of field emission, following helium gas conditioning, except titanium alloy sample TA2, which did not require it. For entries with (>) symbol, field emission current did not exceed 100 pA at −225 kV bias voltage, the maximum voltage available.

	A1 (He) 1200 grit	A2 (He) 1200 grit	TN1 (He) 800 grit	TN2 (He) 1200 grit	TN3 (He) 1200 grit	TA1 DPP	TA2 DPP
50mm	9.0	9.1	>12.8	>12.8	>12.8	10.9	>12.8
40mm	8.5	9.5	>13.7	>13.7	>13.7	10.5	>13.7
30mm	9.0	12.0	>15.4	>15.1	15.2	11.0	>15.4
20mm	10.0	11.8	17.6	18.4	18.4	13.0	>18.7

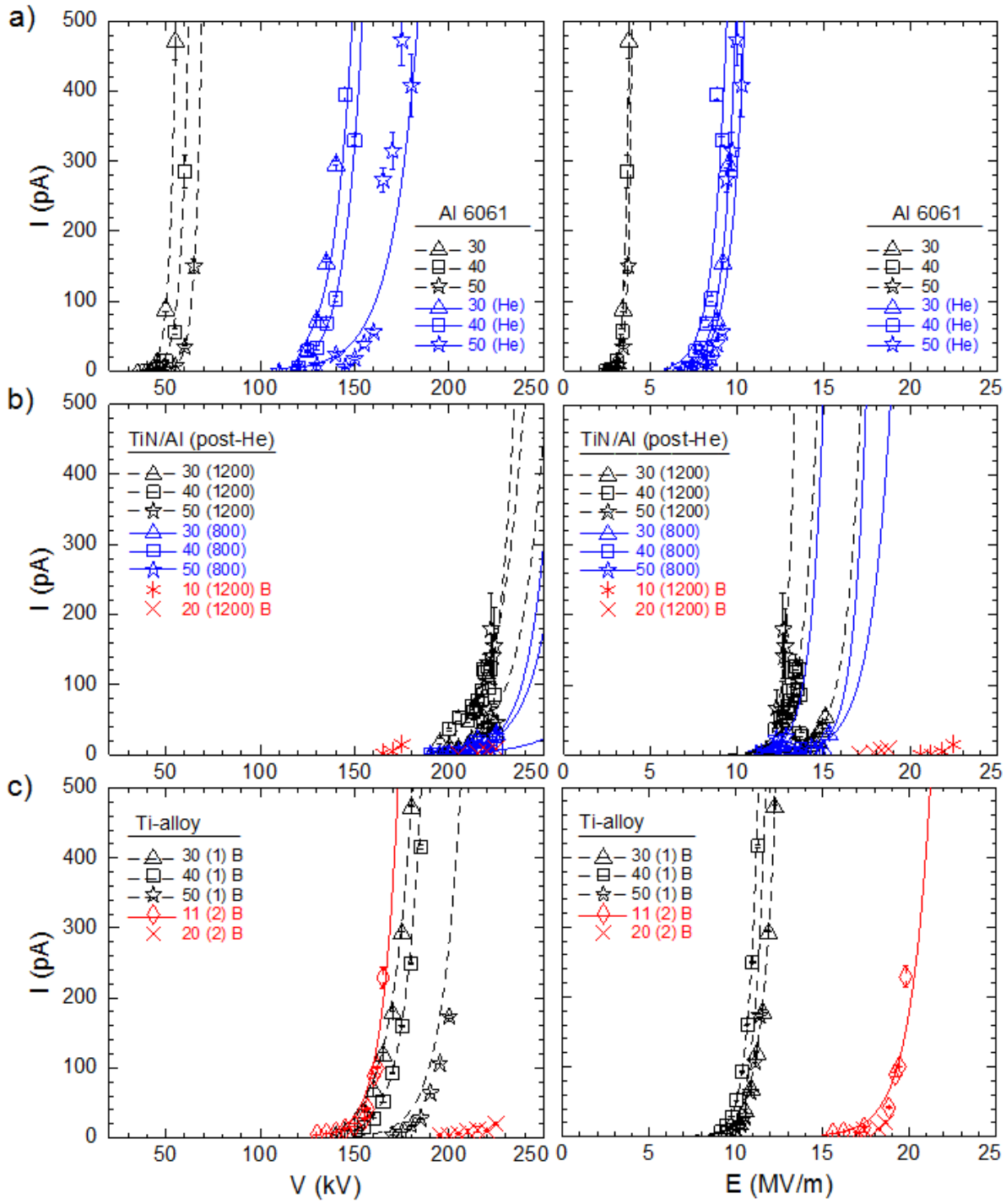


FIG. 3.2. Field emission current vs bias voltage and field strength for different cathode/anode gaps for (a) bare aluminum, (b) TiN-coated aluminum, and (c) titanium alloy electrodes. Labels with "B" represent electrodes that are tested in the baked chamber TS1.

3.3.1. HV characterization results of bare aluminum electrodes

Two uncoated aluminum electrodes were evaluated at high voltage, before and after helium gas conditioning. Because aluminum is so soft, helium was chosen over a heavy gas species like krypton, which can actually create field emission sites due to a comparatively enhanced sputtering rate. In contrast, the benefits of helium gas conditioning stem largely from implantation, rather than sputtering. Based on previous work, helium gas conditioning was shown to be more effective at suppressing field emission when the test sample was biased at lower voltages and for smaller cathode/ anode gaps—conditions that ensure ions are implanted at shallow depths, thereby serving to most effectively increase the work function of the surface. After helium gas conditioning, electrodes were recharacterized under the best vacuum conditions. A representative collection of results is shown in Fig. 3.2(a), for one bare-aluminum test electrode, corresponding to sample A1 in Table 3.2.

Before helium gas conditioning, bare aluminum electrode A1 exhibited 100 pA of field emission at voltages between −64 and −36 kV, for cathode/anode gaps between 50 and 20mm, corresponding to field strengths of 3.0 and 3.6 MV/m. Bare aluminum electrode sample A2 performed better, with 100 pA of field emission observed at voltages between −90 and −65 kV and field strengths 5 and 5.4 MV/m, for the same range of cathode/anode gaps. The high voltage performance of both electrodes improved significantly upon helium gas conditioning, with 100 pA of field emission observed at voltages between −158 and −121 kV and field strengths between 8.5 and 12.0 MV/m. However, it must be noted that for both bare aluminum electrodes, improved performance could be short lived. Gas conditioning could once again be implemented to minimize field emission, but the back and forth process between poor and improved

performance would repeat, sometimes because voltage was pushed too high but also sometimes without warning, with high levels of field emission observed at a voltage that earlier provided zero field emission current.

3.3.2. HV characterization results of TiN coated aluminum electrodes

The three TiN-coated aluminum electrodes, polished with 1200 and 800 grit silicon carbide paper, exhibited dissimilar high voltage performance prior to helium gas conditioning; however, they behaved similarly afterwards. Only the post-gas conditioning results are shown in Fig. 3.2(b), which shows the performance of two TiN-coated electrodes. The results for the third TiN-coated aluminum electrode were similar, but they were omitted from the graph to provide clarity. Field emission current did not reach 100 pA even at the maximum voltage of −225 kV for cathode/anode gaps 30mm and larger. This clearly represents a significant improvement over the uncoated-aluminum electrode performance. For cathode/anode gaps in the range of 30–20 mm, 100 pA of field emission was observed at voltages between −222 and −212 kV, corresponding to field strength between 15.1 and 18.4 MV/m.

TiN-coated aluminum electrode sample TN2 was studied further in the baked high voltage test stand, TS1, which could accommodate cathode/anode gaps smaller than 20 mm, and hence subjecting the electrode to higher field strength. These data are plotted in Fig. 3.2(b), with suffix designation “B” for baked. No measurable field emission current was observed (<10 pA) at the maximum voltage of −225 kV for gap settings 20 mm and larger. The electrode produced less than 15 pA of field emission current at −175 kV for a 10 mm cathode/anode gap, which corresponds to field strength of 22.5 MV/m. This level of performance was achieved without gas

conditioning. At higher voltage, breakdown was observed, i.e., field emission current suddenly went from small to large, and the field emitter(s) could not be processed-out via gas conditioning. Upon inspection, the electrode possessed a noticeable visual defect. Breakdown occurred at a voltage consistent with the predictions of P. Slade, as shown in Ref. 107.

Of the three TiN-coated aluminum electrodes, sample TN2 performed the best, reaching the highest voltages and field strengths while exhibiting the smallest levels of field emission. But as Table 3.2 suggests, the other TiN-coated aluminum electrode samples performed similarly. The other samples (TN1 and TN3) were pushed to higher voltages and field strengths similar to sample TN2 to evaluate coating limitations. Although neither of the other two samples suffered breakdown, they both suffered reduced performance that could not be recovered with further gas conditioning, at least not as it was implemented. At this point, field emission was observed from TiN-coated electrode samples TN1 and TN3 at voltages and field strengths approximately 50% of values as indicated in Fig. 3.2(b) and Table 3.2. Upon inspection, no obvious defects were visible to the naked eye, or using a microscope.

3.3.3. HV characteristics results of diamond paste polished Ti-alloy electrodes

Two Ti-alloy electrodes were painstakingly polished to a mirror like surface finish using diamond grit and characterized at high voltage [Fig. 3.2(c)]. As often happens when evaluating nominally identical electrodes, dissimilar performance was observed for the two Ti-alloy electrodes, but in this case, dissimilar performance was maintained even after gas conditioning. Before gas conditioning, Ti-alloy electrode sample TA1 generated 100 pA of field emission at voltages between −192 and −153 kV for cathode/anode gaps between 50 and 20 mm,

corresponding to field strengths of 10.9 and 13.0 MV/m. This performance is comparable to that of traditional diamond-paste polished stainless steel [92]. Ti-alloy electrode sample TA1 was subjected to helium gas conditioning, which actually resulted in degraded performance. The post-helium gas conditioning data are not included in Fig. 3.2(c).

In sharp contrast, Ti-alloy electrode sample TA2 performed far superior to sample TA1, exhibiting less than 20 pA of field emission at the maximum voltage —225 kV for cathode/anode gaps between 20 and 50 mm. This electrode was studied at higher field strengths using smaller gaps of 17, 14, and 11 mm, where 100 pA of field emission was observed at voltages between —200 and —153 kV, corresponding to field strengths of 18.4 and 21.2 MV/m.

3.4. SURFACE EVALUATION

3.4.1. Topography and chemical composition

Surface characterization of the electrodes was performed using a Joel 6060LV SEM with 3 nm resolution. Surface images for an aluminum electrode polished with 1200 grit silicon carbide paper are shown in Fig. 3.3. Tooling marks could be seen on the polished, uncoated bare aluminum electrode surface [Fig. 3.3(a)], which exhibited numerous defects including pits and protrusions. No evidence of residual silicon carbide particulate contamination was observed. It is reasonable to assume tooling marks and defects represent potential field emission sites. Gas conditioning of the bare aluminum electrode introduced additional defects, like the one displayed in Fig. 3.3(b). Thus, although helium gas conditioning served to reduce overall field emission

from both of the bare aluminum electrodes that were studied, ion bombardment and surface sputtering lead to significant transformation of surface topography.

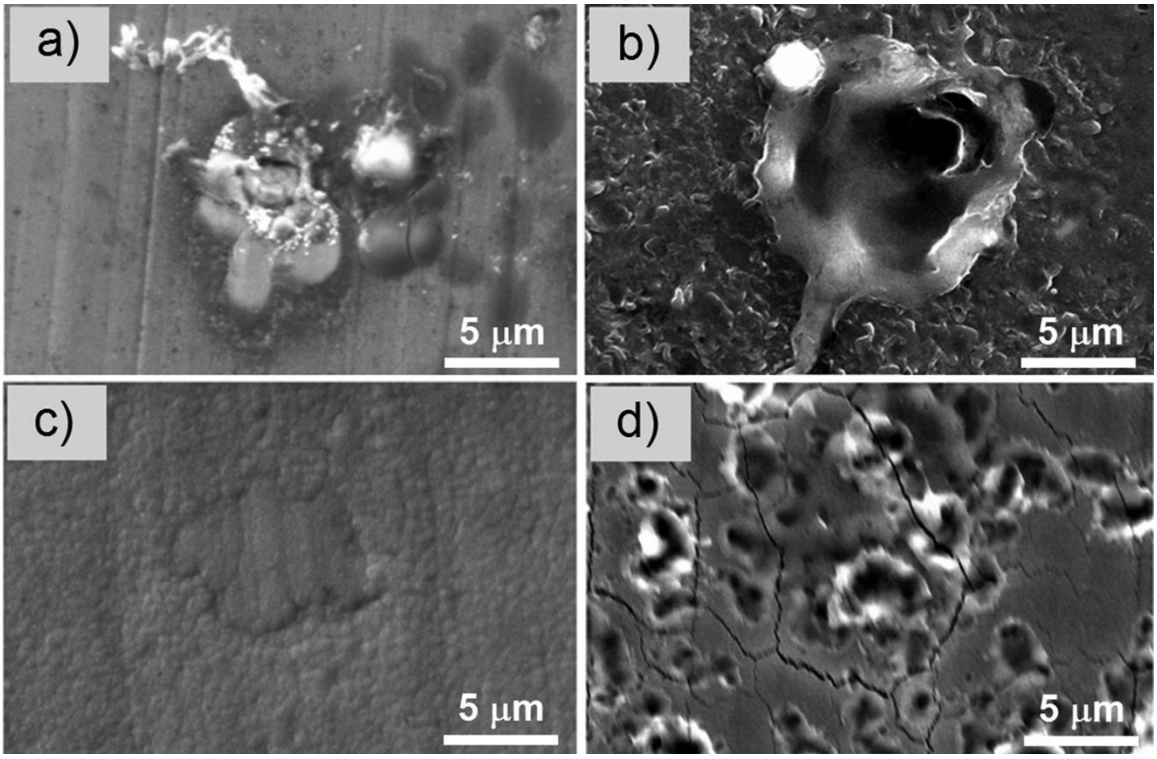


FIG. 3.3. SEM images of bare and TiN-coated aluminum electrode surface, (a) bare aluminum electrode surface showing a typical defect, (b) bare aluminum electrode surface showing a defect produced as a result of helium gas conditioning, (c) TiN-coated aluminum electrode surface showing a subsurface defect covered by TiN coating, and (d) TiN-coated electrode surface subjected to high field strength, and damaged postbreakdown.

The TiN coating served to smooth the bare aluminum electrode surface, concealing defects like the one barely visible in the center of the photo in Fig. 3.3(c). No change in TiN coating surface morphology was observed, before and after gas conditioning. The image in Fig. 3.3(d) depicts a damaged TiN coating that resulted when TiN-coated aluminum electrode sample TN2 was exposed to very high field strength, incurring breakdown.

The surface morphology and film thickness was characterized using a 2D surface profilometer and an AFM on small coupons representing prior and post-coated electrode surfaces. The RMS surface roughness was 20 and 16 nm, for the 800 and 1200 grid polished bare aluminum samples, as measured using the profilometer with a 2 mm line scan. The surface roughness decreased from 16 to 13 nm after application of the TiN coating (for the 1200 grit polished coupon). Two and three dimensional AFM images of the surface morphology of the TiN coating on the 1200 grit polished coupon are presented in Fig. 3.4. From a scan area of 1 μm × 1 μm, the average values of the RMS roughness and grain height were measured as 7 and 20 nm, respectively. These independent measurements of the roughness (using profilometer and AFM) are reasonably consistent and indicate a very smooth TiN coating, smoother than metal surfaces that are polished with diamond paste, or chemically etched [92]. The film thickness of the TiN coating on a 1200 grit polished Al electrode was also measured as ~2.5 μm using step-height profilometry.

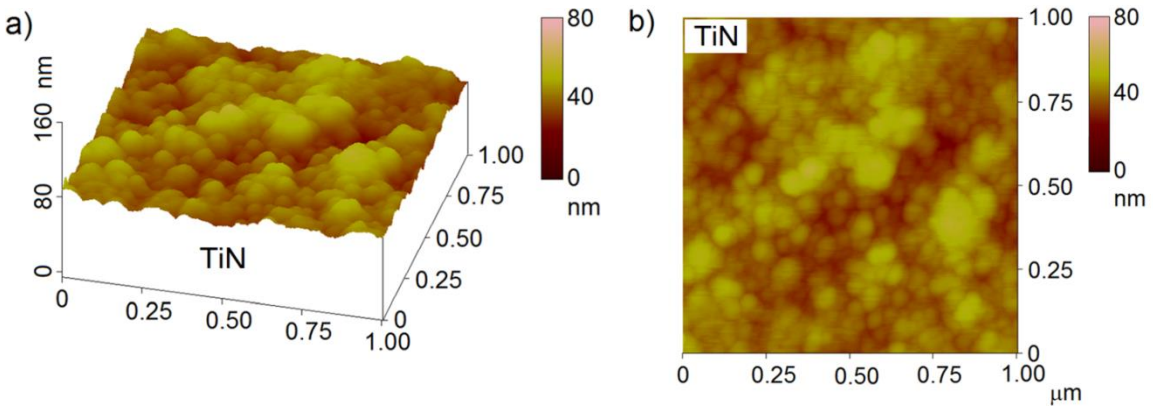


FIG. 3.4. Surface morphology of the TiN coated 1200 grit polished Al6061 coupon revealed by AFM with (a) 3D and (b) 2D displays. RMS roughness and average grain height were measured as 7 and 20 nm, respectively, for the scan area of 1 μm × 1 μm.

3.4.2. Hardness measurement

Nanomechanical properties of aluminum test coupons were evaluated before and after the TiN coating. Nanoindentation experiments were performed using an XP nanoindenter from Agilent in conjunction with the CSM in depth control mode to measure the hardness of the TiN thin films. Using the CSM technique, the hardness was continuously measured as a function of penetration depth into the surface by superimposing a small harmonic force oscillation (usually resulting in a harmonic displacement oscillation of 2 nm or less) on the tip during the loading cycle. This allowed the stiffness of contact, and subsequently the mechanical properties of the sample to be constantly evaluated by analyzing the harmonic force and harmonic displacement data, as detailed elsewhere [108,109]. A total of 15 indents with maximum indentation depth of 1 μm were performed on each sample. The allowable drift rate and the strain rate for loading were specified as 0.05 nm/s and 0.05 s^{-1}, respectively.

The results are indicated in Fig. 3.5, where the hardness and modulus are plotted versus contact depth. The TiN coating hardness and modulus were 18 and 270 GPa, respectively, at 50 nm depth of indentation. In comparison, the hardness and modulus of bare aluminum were 2 and 70 GPa, respectively. Clearly, the TiN coating served to harden the surface. Hua and Li [110] concluded that the mechanical properties such as the yield strength, modulus, and hardness strongly affect the work function to the sixth power. Based on the dependence of the elastic modulus on the electron work function and the Peierls–Nabarrow model, they also correlated the yield strength and hardness of metals with the electron work function and concluded that the established intrinsic sixth-power correlations are consistent with reported experimental measurements [110]. In general, electrodes with higher work function are

anticipated to demonstrate higher high voltage standoff; therefore, TiN-coated aluminum electrodes with superb hardness and elastic modulus likely lead to enhanced electron work function.

To qualitatively assess the adhesion of the TiN coating to the bare aluminum, SEM microscopy scans were conducted on the residual impressions left by the indenter for different depths of indentation (Fig. 3.6). The images of 500 nm to 3 μm deep Berkovich indents on the

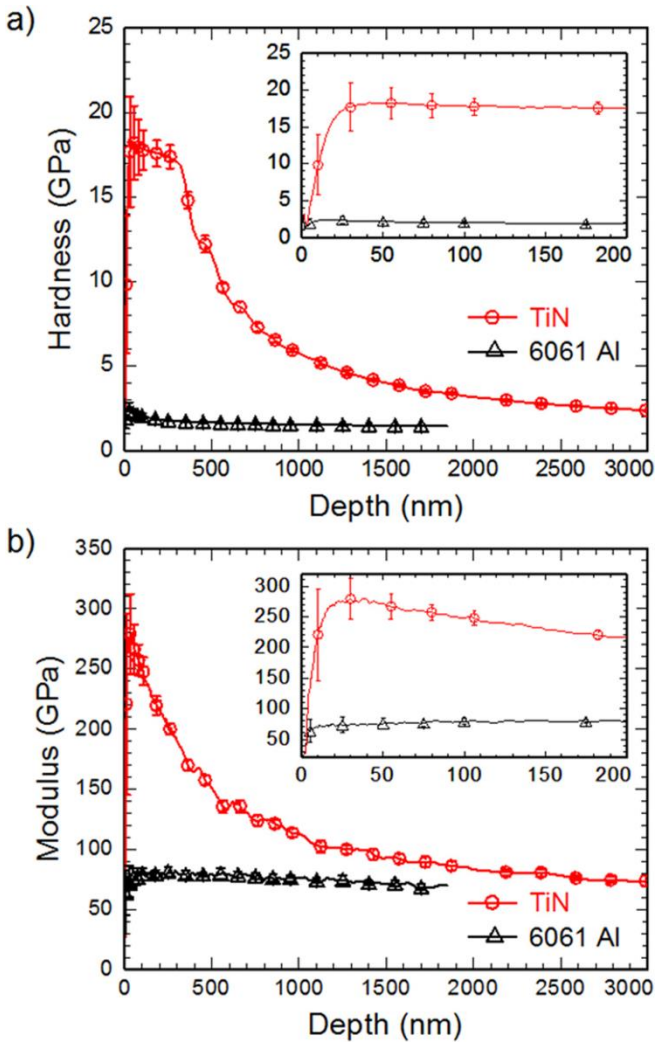


FIG. 3.5. (a) Hardness and (b) modulus as a function of contact depth of indentation for uncoated and TiN coated Al6061. The error bars represent three standard errors.

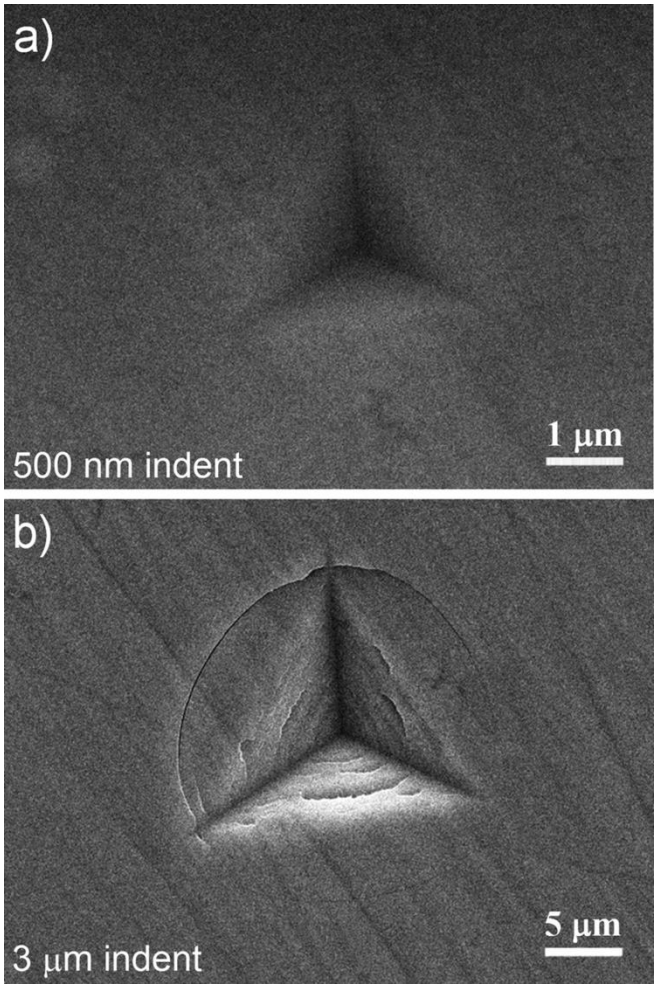


FIG. 3.6. SEM images of the residual impressions of (a) 500 nm and (b) 3 μm Berkovich indents on the TiN coated 1200 grit polished Al6061 coupon. The occurrence of cracks for the larger indent was observed as pop-in events during indentation.

TiN coated 1200 grit polished aluminum sample indicate no signs of delamination or peeling of the film from the substrate. However, nonradial fracture mode was observed for the larger indents [Fig. 3.6(b)]. For a hard-on-soft film system like TiN on Al6061, the film experienced successive fracture events at indentation depths larger than 500 nm, which was observed as pop-in events during the loading cycle of indentation test, as depicted in Fig. 3.7.

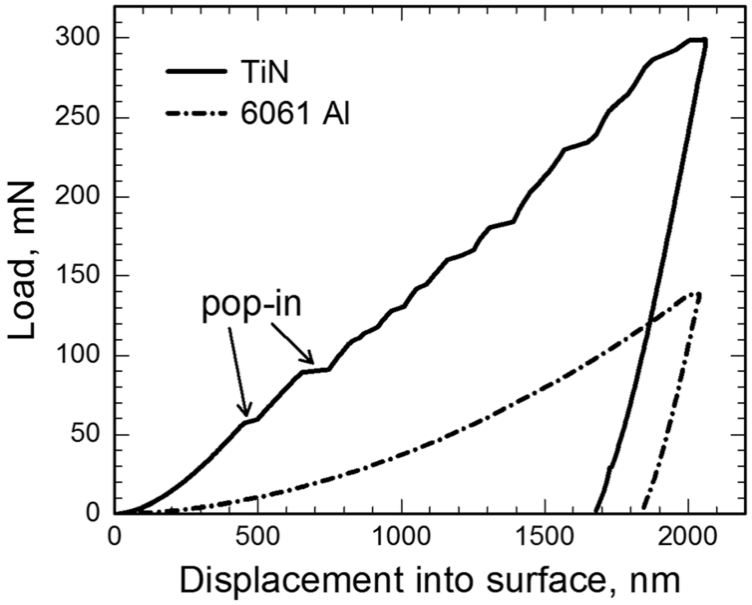


FIG. 3.7. Load vs displacement into surface for 2 μm indents on uncoated and TiN coated Al6061 coupons with 1200 grit surface finish. Pop-in events observed for indenter penetration depth of >450 nm indicate fracture incidences.

3.5. SUMMARY

We have shown that aluminum electrodes, coated with TiN, can be used inside DC high voltage electron guns. The aluminum electrodes required less time and money to prepare, compared to electrodes manufactured from harder materials. The application of the hard TiN coating serves to protect the soft aluminum electrode from scratching and produces a surface finish superior to a diamond-paste polished surface. Also when biased at high voltage and exposed to high field strength, the TiN-coated aluminum electrodes exhibited comparatively low levels of field emission. All three TiN-coated aluminum electrodes reached —225 kV without field emission at 50 mm cathode/anode gaps, corresponding to field strength of ~13.0 MV/m. The best performing TiN-coated aluminum electrode produced 100 pA of field emission at field strength of 22.5 MV/m. We attribute the superb performance of the coated electrodes to the hard and

uniform TiN coating, with a high work function, and the ability of the TiN coating to limit the undesirable effects of the underlying impurities and defects of the aluminum surface.

The surface finish of TiN-coated aluminum coupons, polished with 800 and 1200 grit silicon carbide paper was ~7 nm. This is smoother than electrode surfaces created using conventional polishing techniques at Jefferson Lab. The mechanical properties of the TiN electrode, hardness and modulus, were far superior to bare aluminum, and to stainless steel, niobium, and titanium-alloy, based on the literature. The hardness and modulus were measured as 18 and 270 GPa, respectively. SEM microscopy scans of the residual impressions indicated no signs of delamination or peeling of the film from the substrate.

Aluminum electrodes, coated with TiN, could simplify the task of implementing photocathode cooling, which is required for future high current electron beam applications. For example, two designs for a future electron-ion collider [15,16] require electron guns that provide ~100 mA average current to implement electron cooling of proton beams. The other accelerator applications, like the search for the proton electric dipole moment, could benefit from TiN-coated aluminum electrodes. One experiment [111,112] hopes to search for a proton EDM using spin-polarized and counter-propagating proton beams traveling inside an all-electric storage ring composed of hundreds of capacitor plates with a cumulative electrode path length of over 1 km. capacitor plates, made of aluminum and coated with TiN, could satisfy the electrostatic requirements of the storage ring, while costing considerably less than plates made of stainless steel. We speculate that the added cost of the TiN coating would be smaller than the cost savings associated with purchasing less expensive aluminum and significantly reduced labor charges for polishing.

3.6. CONCLUSION

Successful operation of a DC high voltage photogun at high bias voltage requires that field emission be eliminated from the cathode electrode. A hard TiN coating with better work function was applied on inexpensive aluminum electrodes to prevent field emission under very high voltage. The TiN coated aluminum electrode demonstrated no field emission at 175 kV with ~22.5 MV/m at 10 mm cathode/anode gap. This performance is satisfactory to meet the field emission suppression requirement in a very high voltage accelerating ultra-bright electron source. The TiN film resulted in a surface finish of the electrodes superior to the diamond paste polished surface and demonstrated superior mechanical properties to the traditional electrode materials. These features contributed to the improved high voltage performance of the TiN coated aluminum electrodes and performed better than our benchmark traditional electrodes made of Ti-alloy.

CHAPTER 4

EFFECTS OF ANTIMONY THICKNESS ON THE PERFORMANCE OF BIALKALI-ANTIMONIDE PHOTOCATHODES

4.1. INTRODUCTION

Among semiconducting photocathodes, the alkali-antimonides have attractive characteristics [34,36,37,113], namely, high quantum efficiency (QE) and robust operation under relatively modest vacuum conditions, which makes them ideal for high current photogun [41,42,114,115] applications. The first successful demonstration of CsK_2Sb photocathodes in a normal conducting radio frequency gun was reported in the 1990s by Dowell *et al.*, which demonstrated QE of ~12% and then-record-level current production [36]. New light source initiatives [116-118], proposed nuclear physics experiments such as DarkLight [38], and electron cooling of proton beams for electron ion collider proposals [39,119] depend on high average current energy recovery linacs. These projects have generated renewed interest in alkali-antimonide photocathodes, which represent an excellent alternative to delicate negative electron affinity GaAs:Cs photocathodes [14,120], providing similarly high QE but exhibiting less sensitivity to ion back bombardment and surviving under markedly harsher vacuum conditions [36]. Since alkali-antimonide photocathodes possess a positive-electron affinity, they are considered to be prompt emitters and therefore capable of producing shorter bunches, making them more attractive than the GaAs:Cs photocathodes for applications in high-brightness x-ray free electron lasers and fourth generation

Major content of this chapter is reprinted with permission from M.A. Mamun, C. Hernandez-Garcia, M. Poelker, and A.A. Elmustafa, "Effect of Sb thickness on the performance of bialkali-antimonide photocathodes," Journal of Vacuum Science & Technology A 34 (2), Mar/Apr 2016, 021509 (14 pages).

light sources [37,41,121].

Photocathode performance relies on growth conditions defined by photocathode material composition, vacuum condition, and deposition process. The main objective of this individual study is to identify optimum growth conditions for producing photocathodes that exhibit high QE and prolonged photocathode lifetime. Photoguns typically employ front face illumination of the photocathode surface (not transmission mode), in which case, the thickness of the photocathode is not a limiting factor, at least not in terms of how the light is delivered. However, common recipes for alkali-antimonide fabrication rely on sequential deposition of K and Cs onto a relatively thin Sb layer (~15 nm) [122] similar to recipes used for photomultipliers tubes [123] where the Sb layer must transmit light. During photocathode fabrication, the chamber overall vacuum level and presence of water are known to affect the growth and morphology of Sb films [124-127]. To study the effect of these properties on the photocathode QE and lifetime, bialkali-antimonide photocathodes were successfully fabricated using an effusion source [10,128] by codeposition of Cs and K alkali species onto Sb layers of varying thickness. The Sb layer was grown simultaneously on GaAs and Ta substrates in a vacuum chamber following two distinct protocols: (1) photocathodes were prepared and evaluated in a vacuum chamber that was baked at 200 °C for 30 h each time the chamber was vented for loading new substrates (vent-bake protocol), and (2) photocathodes were prepared and evaluated in the same initially baked vacuum chamber, but the chamber was not baked again after venting with clean dry nitrogen when new substrates where installed (vent-no-bake protocol). Under these markedly different vacuum conditions, comparable QE values were obtained even though the Sb films exhibited very different growth characteristics. The highest measured QE values were ~10% at 532 nm. In

contrast, the QE 1/e lifetime at low bias voltage showed a stronger dependence on the Sb layer thickness. In addition, this work demonstrates the practical advantages of using a relatively simple effusion source for codeposition of multiple alkali species, which appears to yield an optimized stoichiometry in a straightforward manner, comparable to sequential deposition of individual alkali species. The present work provides a more detailed description of the experimental techniques previously reported by the authors [45] and adds surface science evaluation of Sb-film surface morphology, thickness, and structure by means of field emission scanning electron microscopy, x-ray diffraction, and atomic force microscopy.

4.2. EXPERIMENTAL

This study was conducted in two phases: first, the Sb-film growth was characterized as a function of film thickness, and second, the Sb deposition processes of the first phase were repeated and followed by a codeposition of K and Cs to fabricate bialkali- antimonide photocathodes. Two groups of photocathodes were fabricated and evaluated for their QE and lifetime performance. Photocathodes within each group were distinct, having different Sb layer thickness, and with different surface morphology that resulted from the vent-bake and the vent-no-bake vacuum protocols. A detailed description of the complete apparatus and experimental techniques is presented below.

4.2.1. Deposition chamber

A dedicated vapor deposition chamber was designed, built, and commissioned for this study (Fig. 4.1). The bialkali-antimonide photocathodes were grown and evaluated at a low bias voltage

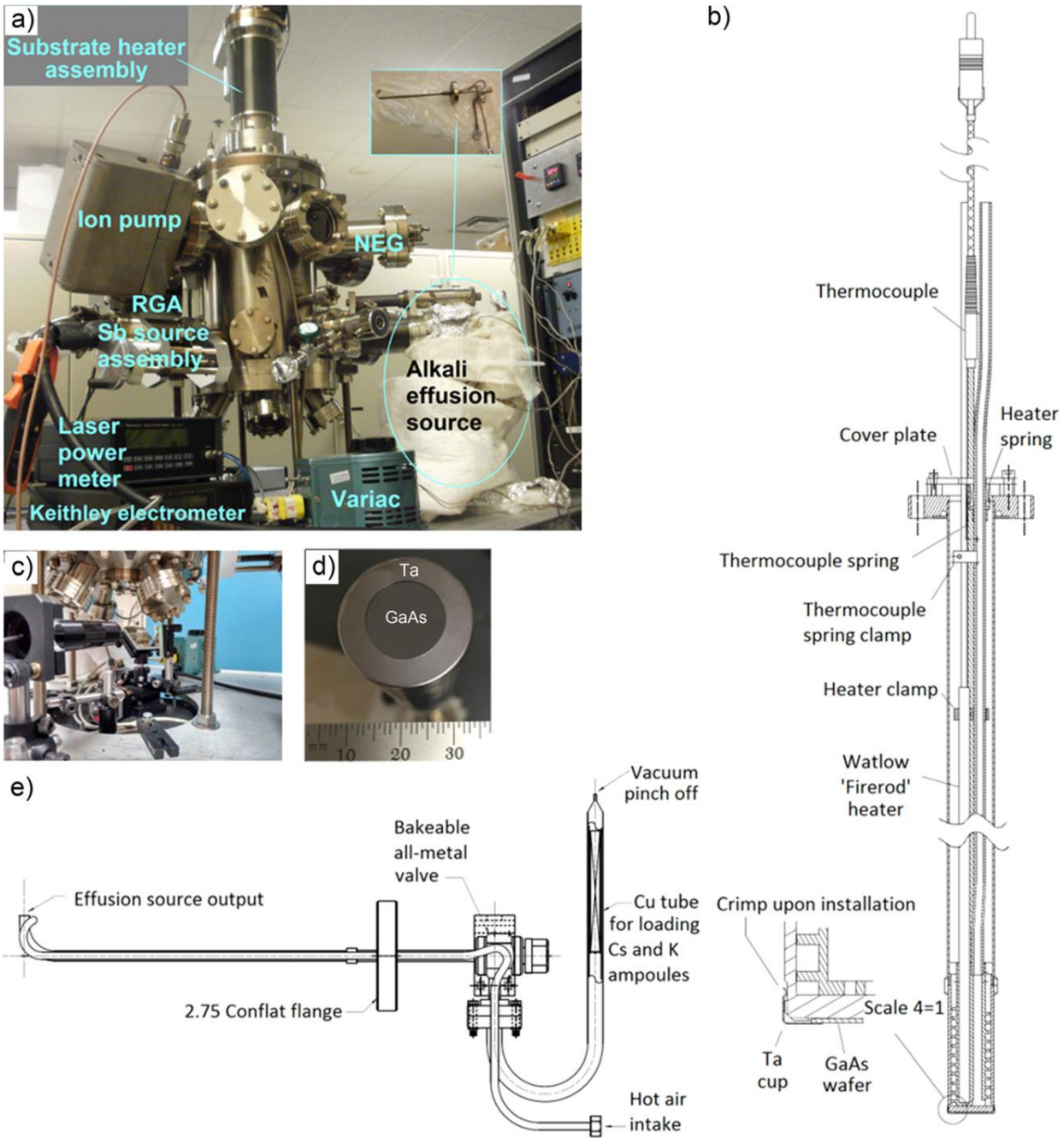


FIG. 4.1. (a) Photograph of the bialkali-antimonide photocathode deposition chamber with effusion-type alkali dispenser (shown in the inset), (b) schematic of the substrate holder assembly with substrate heater, (c) photograph of the laser system with the mirrors attached to the stepper-motor-controlled translation stages, (d) photograph of the GaAs substrate secured to the sample holder using an annular Ta cup, and (e) schematic of the effusion-type alkali dispenser used for coevaporation of K and Cs species (with permission from Lawrence S. Cardman).

of 284 V inside the vacuum chamber capable of operating in the UHV regime. The vacuum chamber, 20.3 cm in diameter and 38.1 cm long, was made from 304L stainless steel sheet, 0.48 cm thick with a 0.8 μm root mean square (RMS) surface finish that was rolled into a cylinder and welded. After manufacturing, the chamber was cleaned with a detergent [75] and solvents prior to assembly. The chamber included ports to accommodate pumps, a residual gas analyzer (RGA), source materials, the substrate holder with accompanying heater [Fig. 4.1(b)], a shutter to control chemical deposition onto the substrate, and view ports for sample illumination.

The vacuum was maintained using nonevaporable getter (NEG) pumps (two GP100 MK5 flange-mounted pumps and two WP950 NEG modules from SAES® Getters, with a total hydrogen pumping speed of 2780 l s^{-1}) and an ion pump (45 S Titan ion™ pump from Gamma vacuum, with a nitrogen pumping speed of ~40 l s^{-1}). A turbomolecular pump was used to achieve a vacuum level suitable to energize the ion pump, and then valved out. The vacuum was continuously monitored using the ion pump current. The deposition chamber was equipped with an RGA mass spectrometer (SRS model RGA200) to continuously monitor the vacuum gas composition and it also served as a deposition monitor for the photocathode chemical species [45].

A single-side polished, p-doped, single-crystal GaAs (100) wafer of 0.5 mm thickness and 75 mm diameter was procured from AXT Company to use as substrate material. The Zn dopant concentration was in the range of $9.1(\pm 0.6) \times 10^{18}$ cm^{-3}. The wafer was cleaved into square-shaped pieces, 1.5 cm × 1.5 cm, which could be attached to a 2 mm thick molybdenum disk brazed to the end of a long stainless steel tube that served as part of the vacuum enclosure. A heater with K-type thermocouple was inserted into the tubular substrate holder and pressed firmly against

the back surface of the molybdenum disk (i.e., atmosphere side) via an applied spring force [Fig. 4.1(b)]. Calibration measurements indicated that the actual substrate temperature in vacuum was 80.8% that of the thermocouple reading. The GaAs substrate was secured to the sample holder using an unpolished annular Ta cup of 2.54 cm outer diameter (OD) that also served as a second substrate for the photocathode deposition [Fig. 4.1(d)]. A heater controller with feedback mechanism was used to control the substrate temperature. After heating, clean dry N_2 could be applied to the substrate holder (atmospheric side) to increase the substrate cooling rate. The substrate could be moved relative to the chemical sources via a bellows assembly with motorized drive screw. During chemical deposition, the substrate was maintained approximately 5 cm from the chemical sources.

The constituent sources consisted of high-purity (99.9999%) Sb pellets from Alfa Aesar [129], and K (99.95% purity) and Cs (99.9+% purity) in 1 g breakseal ampoules from ESPI metals and Strem Chemicals, Inc., respectively. During deposition, the Sb pellets were resistively heated in a tungsten evaporation basket; whereas both alkali species were dispensed from a single effusion type reservoir [Fig. 4.1(e)]. The chamber was equipped with viewports made of Kodial Glass (alkali borosilicate 7056).

4.2.2. Vacuum protocols

During the course of this work, many Sb films and bialkali-antimonide photocathodes were fabricated. Initially, the entire apparatus was baked each time a substrate was replaced. Then, in the course of these studies, a small vacuum leak appeared in the deposition chamber. The leak was fixed but not before observing the fabrication of photocathodes with high QE under

degraded vacuum conditions, with pressure roughly ten times higher than pre-leak conditions. This observation spurred the evaluation of Sb films and photocathodes under two different vacuum conditions designated as vent-bake and vent-no-bake protocols.

4.2.2.1. Vent-bake protocol

The evacuated chamber was baked for the first time at 200 °C for 180 h and leak checked with helium using the RGA (detectable leak threshold of 6.7×10^{-9} Pa l s^{-1}). At this point, the vacuum reached ~6×10^{-9} Pa; however, the vacuum degraded by approximately 1 order of magnitude following the breaking of alkali ampoules and heating of chemical sources. Each time a new substrate was installed, the apparatus was vented with clean dry N_2 from a large liquid nitrogen dewar and rebaked at 200 °C for 30 h. This vent-bake protocol consistently resulted in vacuum in the range of ~10^{-7}—10^{-8} Pa, with H_2 the dominant gas species, and lower levels of CH_4, CO, and CO_2. The partial pressure of water vapor was always less than 1% of the total pressure.

4.2.2.2. Vent-no-bake protocol

After repairing the small vacuum leak, Sb films and bialkali-antimonide photocathodes were fabricated without baking. Precautions were taken to minimize the amount of water vapor introduced to the system when venting including breaking only one flange joint at a time, and purging with a vigorous flow of clean dry N_2. While pumping the chamber with the turbomolecular pump, current was applied to the NEG pumps to degas them and restore pump speed. It was evident from the RGA spectrum that venting without further baking resulted in degraded vacuum, with pressure values now in the range of ~10^{-6}–10^{-7} Pa. The water vapor content increased by ~1 order of magnitude compared to the vent-bake protocol, although still

representing near 1% of the total pressure. Moreover, water partial pressure reduced following each photocathode activation, which was likely a result of excess alkali deposited on the vacuum chamber walls serving as a getter.

For both vacuum protocols, the pressure within the chamber increased when the chemical sources were heated to operating temperatures. For the vent-bake condition, the chamber pressure during the bialkali deposition typically reached $>5 \times 10^{-6}$ Pa but quickly improved to $\sim 10^{-7}$—10^{-8} Pa once the deposition ended. And for the vent-no-bake condition, the chamber pressure during the bialkali deposition typically reached $>1 \times 10^{-5}$ Pa but quickly improved to $\sim 10^{-6}$ –10^{-7} Pa once the deposition ended.

4.2.3. Antimony deposition and surface characterization

In preparation for Sb deposition, the substrate was moved away from the chemical sources and heat cleaned at 550 °C for 2 h. A shutter mechanism, placed a few centimeters in front of the substrate, prevented contamination of the chemical sources and of the viewport used for transmitting light to the photocathode. At the end of heat cleaning and immediately prior to Sb deposition, the substrate was rapidly cooled to 200 °C and kept behind the shutter while resistive heating of the Sb crucible was initiated. Antimony was evaporated from an aluminum oxide crucible that was resistively heated by applying current to a tungsten wire basket that supported the crucible, from a regulated DC power supply (Electronic Measurements, Inc., TCR 40S45–1D-OV DC power supply 0–40 V, 0–45A, 1800W). The crucible with tungsten evaporation basket was initially loaded with approximately 1 g of high-purity (99.9999%) Sb pellets. The Sb partial pressure detected by the RGA was constantly monitored. The current applied to the tungsten

heater was varied to obtain the desired partial pressure of Sb at which point the shutter was retracted and the substrate was lowered from the parking position to a working distance of 5 cm from the source. To obtain a variety of Sb film thicknesses, the current applied to the Sb heater basket was varied from 31.2 to 33.7 A and the deposition time was varied from 30 to 120 min. Under these conditions, the partial pressure of the Sb vapor varied from $7.3(\pm 0.6) \times 10^{-9}$ to $1.3(\pm 0.3) \times 10^{-8}$ Pa. After Sb deposition, the electrical current applied to the tungsten crucible heater was terminated and the Sb source was retracted to a parking position behind a fixed shutter. At this point, the temperature of the substrate was decreased to 120 °C for alkali deposition, or to room temperature for Sb film characterization.

The Sb film thickness values were determined by repeatedly growing Sb films on the GaAs and Ta substrates inside the deposition chamber. After growing a Sb film, the substrates were removed from the chamber and evaluated using the surface science tools listed below, to determine grain structure, morphology, surface roughness, and porosity as a function of Sb thickness. All of these characteristics represent important metrics that could help improve our understanding of the role of the Sb layer on photocathode performance. For Sb film characterization, no alkali species were evaporated onto the substrates.

The film thickness and surface topography were investigated using a cold emission type high resolution Hitachi S-4700 field emission scanning electron microscope (FESEM), and a JEOL JSM-6060 LV scanning electron microscope (SEM). The SEM was operated at an accelerating voltage of 30 kV with a working distance of 10mm, while the FESEM was operated at an accelerating voltage of 15 kV with a working distance of ~12 mm, resulting in a spatial resolution of up to 1.5 nm. The cross-section FESEM imaging was performed for film thickness evaluation. A Bruker-

AXS (Bruker AXS, Inc., Madison, WI) three circle diffractometer equipped with a SMART Apex II CCD detector and graphite monochromated Cu-K_α a radiation source was used for x-ray diffraction (XRD) measurements, to study film structure. The films were identified in the symmetric $\theta/2\theta$ geometry, ranging from $2\theta = 20°$ to 70°. The surface roughness of the films was examined in tapping mode using a Digital Instruments Dimension 3100 atomic force microscope (AFM) from Veeco.

4.2.4. Effusion source for alkali codeposition

As mentioned previously, many traditional procedures for alkali-antimonide photocathode fabrication employ sequential deposition of K and Cs on a ~15 nm Sb film. However, for photocathodes with a thicker Sb layer, we suggest that codeposition of alkali species provides a more optimized stoichiometry. Our photocathodes [45] were fabricated by codeposition of both alkali species using the effusion source depicted in Fig. 4.1(e). The so-called effusion source was a common device used on dc high voltage photoguns from the 1970s through the 1990s, to fabricate CsO-GaAs photocathodes that possess a negative electron affinity [130]. The effusion source was eventually replaced by the now widely used Cs_2CrO_4 based alkali source [131] for GaAs photocathode applications, in large part because they are easier to use. However, for alkali-antimonide photocathode fabrication, the effusion source offers advantages over other alkali sources. Namely, it is a comparatively high capacity source that readily supports codeposition of multiple alkali species. It is also relatively compact, with a small control valve that can be closed to preserve the alkali supply when the rest of the vacuum system is vented. Or conversely, the

control valve can be closed to allow alkali replacement without venting the rest of the deposition chamber.

For charging the effusion dispenser with alkali species, 1 g breakseal ampoules of K (1 cm OD) and Cs (0.6 cm OD) under argon atmosphere were inserted into the 1.27 cm OD (1.12 cm inner diameter) copper pinch-off tube (CPT-133–050 from Huntington Mechanics Lab) with a 1.33 in. mini-Conflat flange on one side that was attached to the control valve of the effusion dispenser. The copper tube thus served as the alkali reservoir of the effusion dispenser. The open end of the copper tube was pinched-off, to make a vacuum tight seal and heated to desorb water while evacuated through the valve. The glass ampoules were then broken by slightly pinching the outside of the copper tube, cracking the glass ampoules, thus liberating the argon gas that was pumped away. This alkali charging of effusion dispenser was done during the chamber assembly phase and provided enough source chemicals for all the activations performed for this study, and many others not included in this summary. To evaporate alkali metals during photocathode fabrication, hot air was passed through the heating tube that represents a central design feature of the effusion source, with the control valve open. The alkali temperature was kept constant by electrical feedback applied to the hot air source. To terminate the flow of alkali, one simply closed the control valve and retracted the effusion source behind a fixed shield that blocked the line of sight to the substrate.

4.2.5. Photocathode preparation

Photocathodes were fabricated using a two-step deposition scheme: Sb was first deposited onto substrates maintained at 200 °C, followed by codeposition of alkali species with the substrate

at 120 °C and falling to 80 °C during the course of photocathode fabrication. Reducing the temperature of the substrate during alkali deposition helped to optimize QE, by providing more control over the photocurrent rate of rise. Alkali deposition was terminated when the photoemission current reached a maximum. When not in use, the effusion source was retracted beneath the shutter with control valve closed. After photocathode fabrication, the substrate was cooled to room temperature passively or more quickly using a nitrogen purge. It is possible to prepare photocathodes on substrates maintained at room temperature; however, evaporation on a heated substrate enhances diffusion of the alkali materials into the bulk material [132], which becomes critical for thick alkali-antimonide photocathode formation.

Details of Sb evaporation were described in Sec. 4.2.3. Immediately prior to alkali deposition, the substrate temperature was brought to 120 °C, and the substrate was placed in the parking position behind the shutter. At this point, the preheated effusion source was moved to the center of the chamber and the control valve was then slightly opened. Evaporation of combined alkali species was controlled by adjusting the heater power and the hot air flow rate applied to the effusion source, and by regulating the control valve. Fine-tuning the temperature distribution of different parts of the effusion source was achieved through judicious application of thermal insulation. Additional heat could be applied to the reservoir tube using an independently controlled heat tape to increase the alkali flux when required. The partial pressure of the alkali vapors was constantly monitored by the RGA. When the desired partial pressure of alkali was achieved, the substrate shutter was retracted, and the substrate was lowered from the parking position to the deposition plane at a distance of 5 cm from the source plane. The different parts of the effusion source were maintained at stable temperatures during alkali evaporation. To

adjust the alkali deposition rate for different photocathodes, these temperatures were varied over the following ranges: the hot air inlet tube (381–462 °C), the dispensing tube (232–294 °C), and the reservoir tube (153–281 °C). The partial pressure of the alkali vapors was recorded during deposition. As an example, for 387 °C at the inlet tube, 259 °C at the dispensing tube, and 184 °C at the reservoir, the partial pressure for Cs and K was recorded as $1.8(\pm 0.10) \times 10^{-8}$ and $4.2(\pm 0.50) \times 10^{-9}$ Pa, respectively.

4.2.6. Photoemission characterization

During application of alkali species, the electrically grounded substrate and Sb film were illuminated with 4 mW of green light (532 nm) from a temperature stabilized laser with 284 V applied to a nearby anode ring. The anode ring was electrically isolated from ground and attached to a sensitive current meter (Keithley electrometer model 617) to detect the photocurrent. The laser power was never attenuated, and no attempt was made to limit the extracted photocurrent, which for the best photocathodes could reach 200 μA. Following fabrication, the photocathode performance was assessed by measuring QE and QE 1/e lifetime at 532 nm. The QE represents a fraction of the incoming photons that produce photoemitted electrons and can be calculated using the equation [133]

$$\mathrm{QE}(\%) = \frac{Ihc}{\lambda eP} \times 100\% = \frac{124I}{\lambda P}, \tag{4.1}$$

where P (mW) is laser power, I (μA) is the measured photocurrent, λ is the laser wavelength (nm), h is Planck's constant (6.626×10^{-34} J s), e is the electron charge (1.6×10^{-19} C), and c is the velocity of light (2.998×10^{8} m s^{-1}).

In order to map the QE across the photocathode surface, the laser beam could be moved across the substrate using mirrors attached to the stepper-motor-controlled translation stages [Fig. 4.1(c)]. The QE measurements were repeated at different time intervals to evaluate photocathode QE lifetime, a metric describing the length of time required to observe QE decay to 1/e of its initial value. The QE lifetime was determined using a least square fit to the QE decay trend. To map the photocathode spectral response over a broad wavelength range from 425 to 825 nm, the simple low power 532 nm laser was replaced with a wavelength tunable white-light supercontinuum laser [134]. During this measurement, a calibrated Si photodiode power meter was used to measure the incident laser power at each wavelength.

4.3. RESULTS AND DISCUSSION

4.3.1. Effects of vacuum practice on Sb growth

Surface science evaluation of the Sb layers deposited on Ta and GaAs substrates, using different vacuum protocols and deposition conditions, provided morphological and structural information as a function of Sb thickness. FESEM, XRD, and AFM results discussed in this section represent important metrics to improve our understanding of the role of Sb layers on photocathode performance.

4.3.1.1. FESEM results

Variations in deposition time, deposition rate (set by the current applied to the Sb crucible heater, and monitored via the Sb partial pressure with the RGA), and vacuum protocols had a significant impact on Sb-film growth on GaAs and Ta substrates. Figure 4.2 shows FESEM-

generated images of surface topography and cross-section views of Sb layers on Ta and GaAs substrates for two different Sb deposition time intervals and partial pressures [100 and 120 min, $7.33(\pm0.6) \times 10^{-9}$ and $1.33(\pm0.3) \times 10^{-8}$ Pa, respectively] for two different vacuum protocols (vent-bake and vent-no-bake). The right-most column of Fig. 4.2 shows Sb-film cross-sectional views obtained by cleaving the GaAs wafer substrate using a diamond-tipped scribe. It was not possible to cleave the Ta substrate to obtain such cross-sectional views. The Sb grain size and film thickness increased dramatically with increasing the deposition time and deposition rate. The Sb film thickness, defined as the distance from the substrate to the outermost edge of the Sb grains, was measured in the range of 50 nm to ~6.7 μm from the GaAs substrates. In general, grain size and porosity of the Sb films increased significantly with increasing film thickness.

It is evident from Fig. 4.2(a) that Sb growth occurred more favorably on the Ta substrate for the vent-bake protocol at a reduced deposition rate. Under these conditions, granular Sb structure was observed on the Ta substrate whereas Sb grain nucleation was prevalent for the GaAs substrate. As the deposition rate and duration was increased, both substrates depicted granular and porous Sb film structure with similar large grains [Fig. 4.2(b)].

In contrast, for the vent-no-bake protocol, the overall growth of Sb was favored equally on both substrates irrespective of the Sb deposition rate [Figs. 4.2(c) and 4.2(d)]. Moreover, a noticeable increase in grain size and Sb thickness was also observed compared to the vent-bake protocol, which resulted in an enhancement of the grain size and the thickness by factors of ~2 and 7, respectively. Once an initial monolayer of Sb is formed, a subsequent Sb growth can be expected to take place at a similar rate. The grain size and the variations in Sb film thickness on GaAs and Ta substrates became minimized once the Sb film grew thicker.

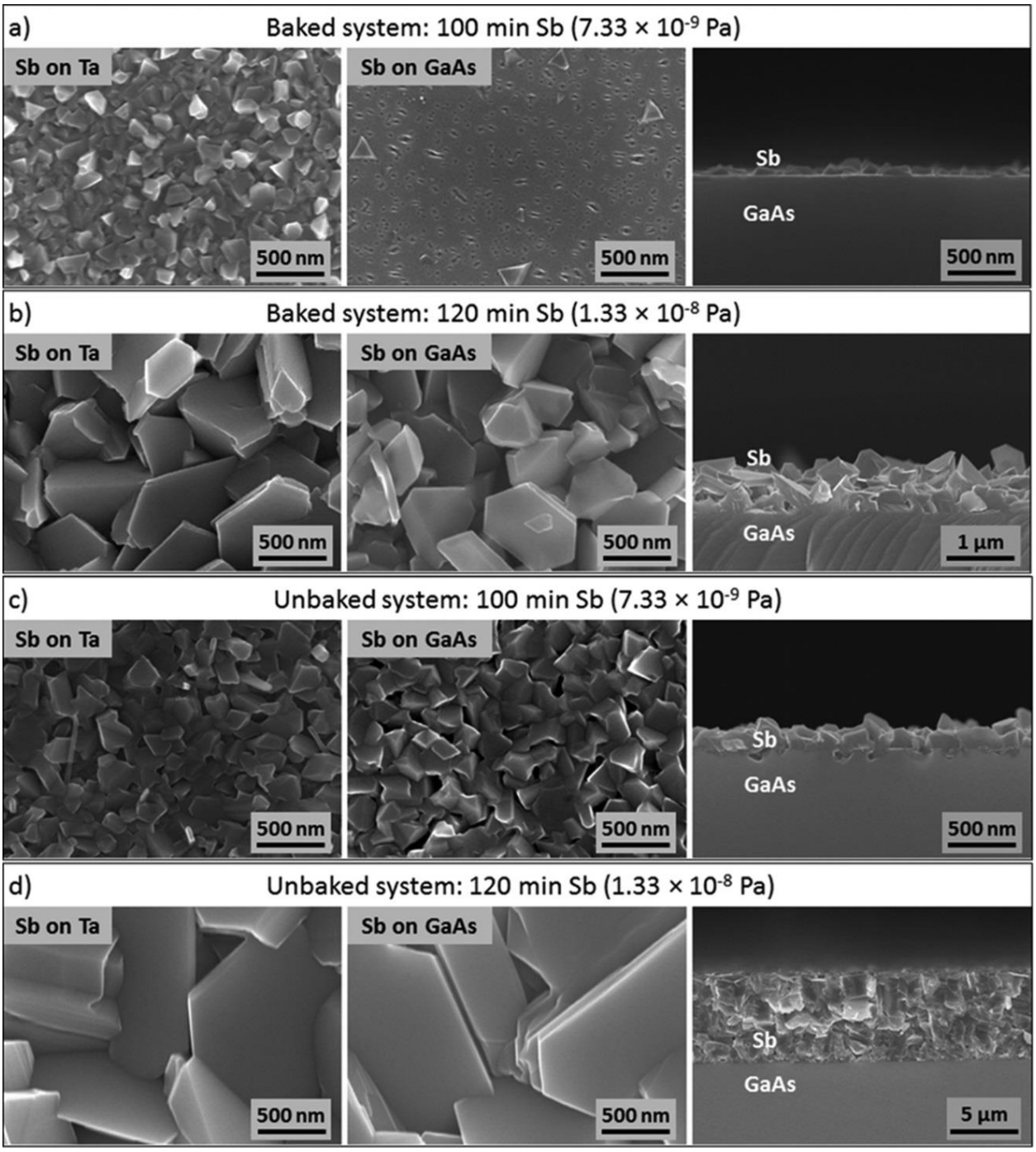


FIG. 4.2. FESEM images illustrating topography and cross-sectional views of Sb films grown on Ta and GaAs substrates for 100 and 120 min deposition times, with 32.7(±0.2) and 33.7(±0.2) A current, respectively, applied to the Sb crucible heater, under two different vacuum protocols: [(a) and (b)] vent-bake and [(c) and (d)] vent-no bake. For vent-bake vacuum protocol, the normal operating pressure was $\sim 10^{-7}$ Pa. For vent-no bake vacuum protocol, the pressure was $\sim 10^{-6}$ Pa.

4.3.1.2. XRD results

X-ray diffraction is a common technique used to study the crystal structure of materials. The crystal structure and the average crystallite size of the Sb films were studied using x-ray powder diffraction. Figure 4.3 shows the XRD patterns of the Sb thin films deposited on GaAs(1 0 0) substrates for 2θ range of 20°–70°. The Sb films exhibited an amorphous structure when very thin, and developed into trigonal [135] and hexagonal [136] polycrystalline phases as they grew thicker. The hexagonal phases are identified in crystallographic planes (1 0 0) and (2 0 0). Similar to the observations reported by Liang *et al.* [137], the diffraction peaks for the Sb films appeared to change as the film thickness and evaporation rate changed. With the emergence of increasing number of nucleation sites as the film thickness increased, the Sb film transitioned from amorphous to crystalline structure. During this transition, the dominant crystallographic plane changed from (2 0 0) to (1 1 6) as indicated by the Sb films with thickness 0.06 and 0.12 μm. A similar change was observed from the thickest Sb film (6.7 μm) where Sb deposition was performed at a higher Sb evaporation rate (by a factor of ~1.9). This was indicated by the emergence of (1 0 4) as the dominant crystallographic plane. The dominant crystallographic planes were identified as (2 0 0), (1 1 6), (1 1 6), (1 1 6), (1 1 6), and (1 0 4) for films with thickness 0.06, 0.12, 0.3, 0.9, 0.95, and 6.7 lm, respectively. The average crystallite sizes of the Sb films were estimated from the dominant peaks using Debye-Scherrer formula [138]

$$D = \frac{K\lambda}{\beta(2\theta)\cos\theta}, \tag{4.2}$$

where D is the mean crystallite size, K is the shape factor, λ is the x-ray wavelength (λ = 1.54 Å for Cu-Ka radiation), $\beta(2\theta)$ is the full width at half maximum (FWHM), and θ is the Bragg

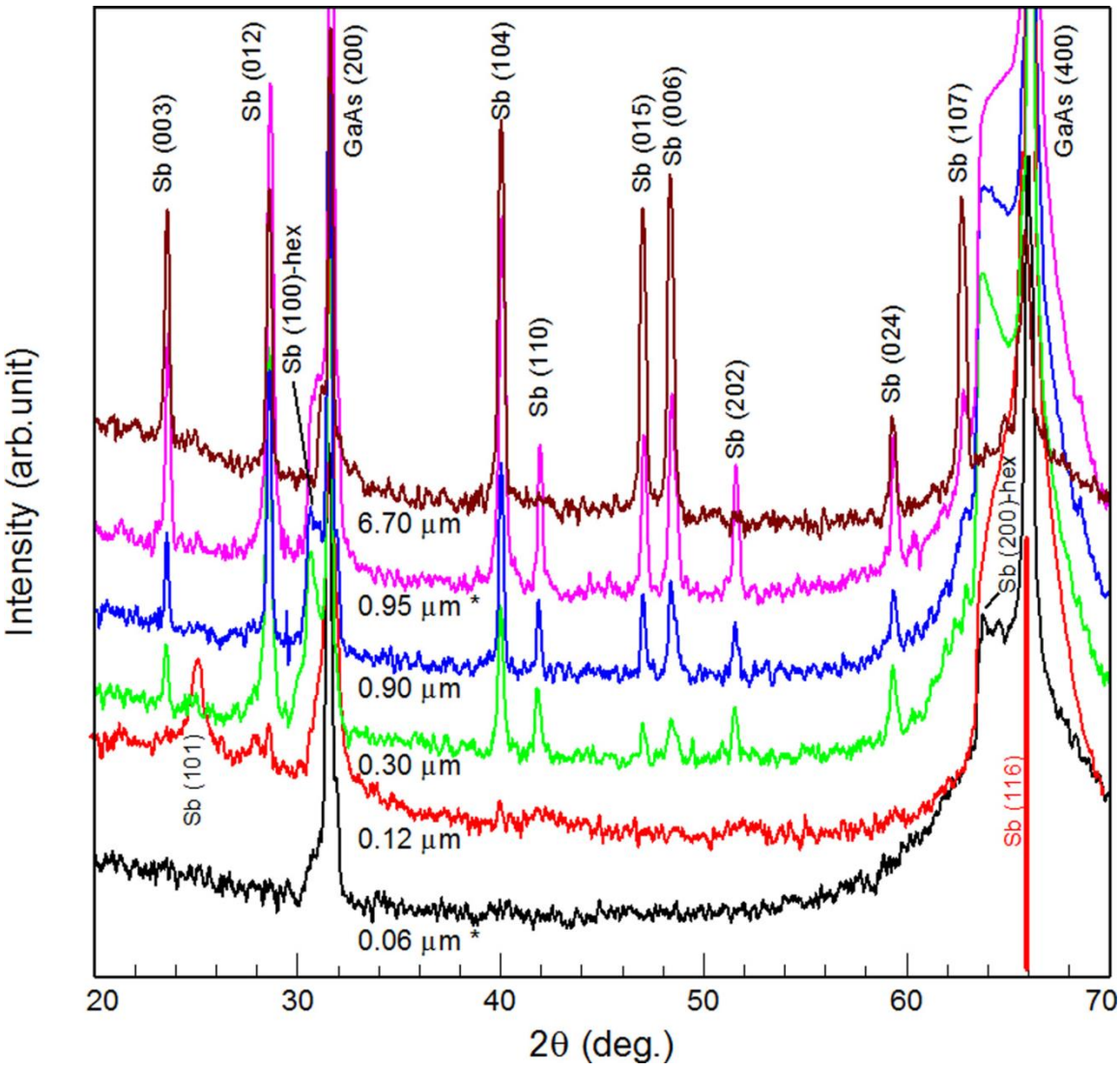


FIG. 4.3. XRD patterns of Sb films with varying thicknesses deposited on GaAs substrate. Antimony films deposited under vent-bake protocol are labeled with asterisk (*).

angle. The FWHM of the dominant crystallographic planes was evaluated as 2484, 1617, 1749, 1677, 1794, and 565 arc sec for 0.06, 0.12, 0.3, 0.9, 0.95, and 6.7 μm Sb films, respectively. The corresponding mean crystallite sizes were evaluated as 13.57, 21.12, 19.47, 20.31, 19.01, and 53.92 nm for the determined dominant planes (2 0 0), (1 1 6), (1 1 6), (1 1 6), (1 1 6), and (1 0 4). These

values indicate that the crystallite sizes of ~13.6, 20.0, and 53.9 nm are dependent on the crystallographic planes (2 0 0), (1 1 6), and (1 0 4). In thin films, crystallite size may affect the microstructural and electrical properties [139]. The increased crystallite size often indicates a decreased level of residual stress and defect density [140] that can result in lowering film resistivity due to reduced grain boundary scattering.

4.3.1.3. AFM results

AFM images illustrated in Fig. 4.4 represent the surface morphology of the Sb films grown on Ta and GaAs substrates using the vent-no-bake protocol. The RMS roughness measured over a 10 μm × 10 μm area of the Sb film increased from 122 to 157 nm on the Ta substrate, and from 42 to 130 nm on the GaAs substrate for the deposition rate and durations of 7.33×10^{-9} to 1.33×10^{-8} Pa and 100 to 120 min, respectively. Under these conditions, the size of the largest Sb grains varied similarly on both substrates, with Sb grain size increasing from 0.6 to 2.6 μm, as measured by the AFM section analysis.

The AFM-measured roughness and maximum grain size of the Sb films grown on GaAs substrate was plotted versus FESEM-measured Sb film thickness, as shown in Fig. 4.5. The Sb grain-size enlargement exhibited a power scaling relationship with the Sb thickness and was not influenced by the evaporation rate of Sb. In contrast, the RMS roughness demonstrated a great influence by the evaporation rate of Sb in addition to the Sb film thickness. This was evidenced by the increasing trend of Sb surface roughness with the Sb thickness and grain size, which ceased when the evaporation rate of Sb was increased by a factor of ~1.9, resulting in a horizontal tail in the graph. This observation reinforces the conclusion made by Liang *et al.* [137] that a high

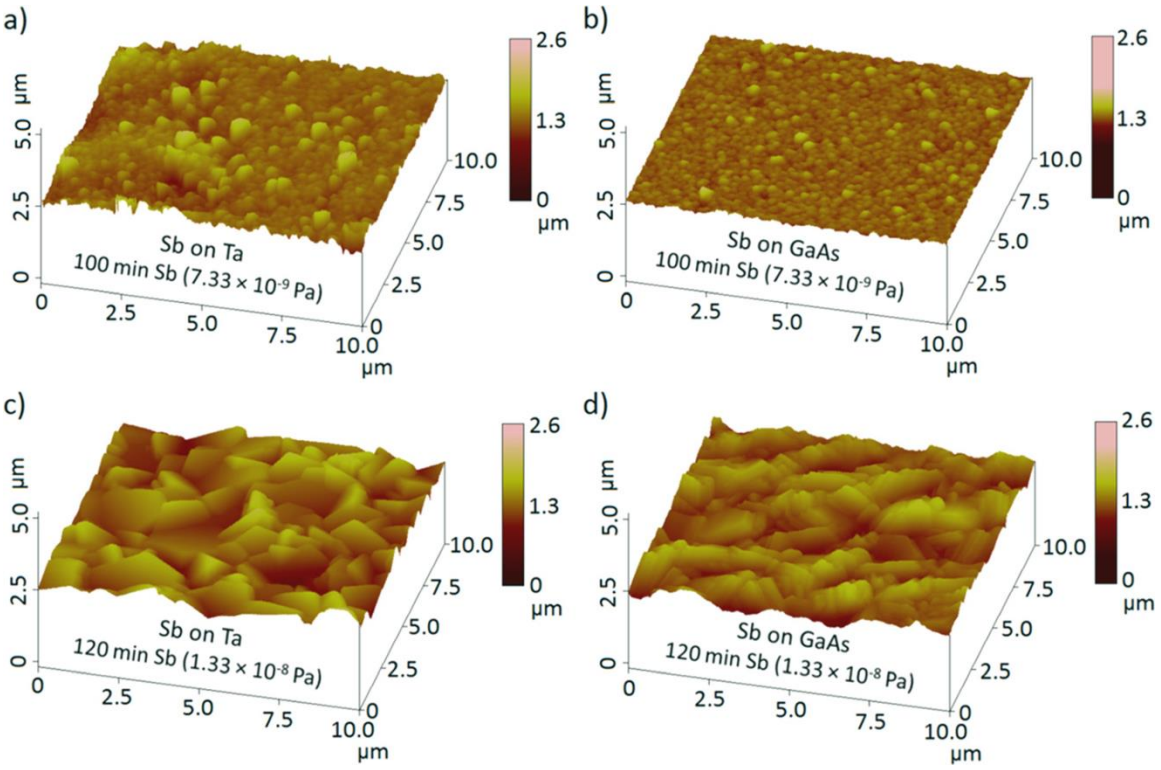


FIG. 4.4. AFM images illustrating surface morphology of Sb films grown on Ta and GaAs substrates for [(a) and (b)] 100 min with 32.7(±0.2) A, and [(c) and (d)] 120 min with 33.7(±0.2) A current applied to the Sb crucible heater following the vent-no bake protocol.

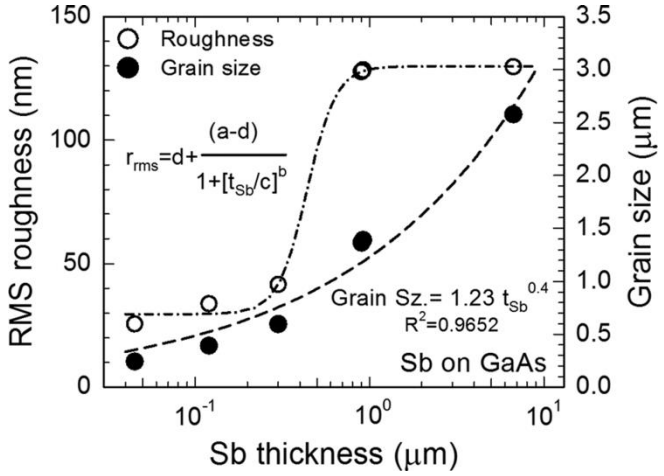


FIG. 4.5. RMS roughness and grain size as function of Sb thickness for Sb films deposited on GaAs substrate. Fitting parameters: a = 29.57444, b = 5.248599, c = 0.4383123, and d = 129.843 (R^2 = 0.9976).

deposition rate of Sb is desirable to avoid a high roughness surface. The least square fit of all-inclusive roughness data resulted in an asymptotic relationship. Assuming similar relationships for Sb films grown on Ta substrates, the grain size and roughness fits were used to estimate Sb film thickness on Ta substrates (Table 4.1), where FESEM cross-sectional views were not possible to obtain.

TABLE 4.1. List of deposition conditions and the corresponding Sb thickness in micrometer. On GaAs substrates, a direct measurement of Sb film thickness was possible via cross-section views using FESEM. For Ta substrates, the Sb film thickness was estimated using the relationship obtained among grain size, roughness, and thickness from Sb films on GaAs.

		Sb thickness, (μm)			
		Vent-bake		Vent-no bake	
Deposition time (min)	PP of Sb in RGA detector (Pa)	GaAs	Ta	GaAs	Ta
30	$7.3(\pm0.6) \times 10^{-9}$	—	0.03[a]	0.045[a]	0.06[a]
70	$7.3(\pm0.6) \times 10^{-9}$	0.06	—	0.12	0.18[a]
100	$7.3(\pm0.6) \times 10^{-9}$	0.10	0.245[a]	0.30	0.31[a]
120	$7.0(\pm0.6) \times 10^{-9}$	—	—	0.90	0.92[a]
120	$1.3(\pm0.3) \times 10^{-8}$	0.95	1.15[a]	6.70	7.27[a]

[a]Estimated values

4.3.2. Quantum efficiency of photocathodes

Literature suggests that the QE of alkali-antimonide photocathodes is highly sensitive to the stoichiometry of the constituent elements [141]. During photocathode fabrication, both substrates were simultaneously exposed to the same amount of evaporated sources, but as the alkali species were deposited subsequent to the Sb deposition, any difference in the Sb layer thickness or morphology on each substrate could lead to dissimilar stoichiometry and QE distribution. Prior

to QE evaluation, photocathodes were cooled to room temperature, and the QE was allowed to stabilize for 6 to 12 h. During this time, it was presumed that excess Cs slowly desorbed from the photocathode surface due to the high vapor pressure even at room temperature. Moreover, the effect of superficial oxidation occurred during this time could significantly enhance the quantum yield of this photocathode [142]. The stabilized QE of each photocathode was then mapped across the entire photocathode surface using the low power green laser, with <1 mm diameter spot size (FWHM), rastered in steps of ~0.5 mm.

QE maps illustrating key observations are shown in Fig. 4.6. The QE maps obtained via the vent-bake protocol [Figs. 4.6(a) and 4.6(b)] indicate that QE could be optimized on one substrate or the other, but not on both simultaneously. In contrast, the QE map obtained via the vent-no-bake protocol [Fig. 4.6(c)] shows relatively uniform QE across both substrates. To facilitate the discussion, representative FESEM topography images and relevant QE maps are shown in Fig. 4.7. It is not surprising to see markedly different QE on the GaAs and Ta substrates because Sb growth was favored on the Ta substrate using the vent-bake protocol [Fig. 4.7(a)]. Although relatively high QE could be achieved on both substrates, the chemical deposition conditions for the resulting optimized QE were markedly different. In this case, the photocathode on the GaAs substrate was optimized for the QE whereas the Ta substrate exhibited no QE because the deposited alkali materials did not reach a critical level to produce optimized stoichiometry of the photocathode on the relatively thicker Sb layer. For the vent-no-bake condition, which supported the Sb film growth equally on both substrates, the QE maps were more uniform across both substrates [Fig. 4.7(b)].

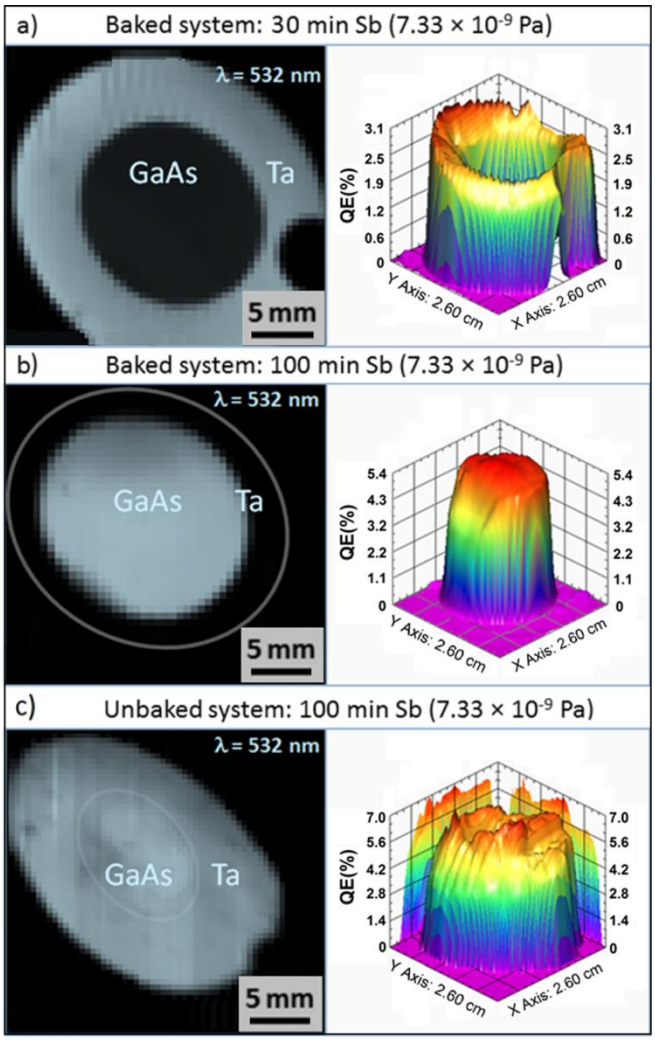


FIG. 4.6. QE (%) map of the photocathodes biased at 284 V with 532 nm (3.96 mW). The photocathodes were prepared by bialkali codeposition following the vent-bake protocol on (a) a 30 min grown Sb layer and (b) a 100 min grown Sb layer; and following the vent-no bake protocol on (c) a 100 min grown Sb layer. The Z axis in the 3D plot represents QE (%).

Optimized QE values for each substrate as a function of the Sb film thickness are illustrated in Fig. 4.8, where film thickness values represent estimates based on the surface science results described above. The QE values varied from ~3% to 10% for photocathodes with Sb layer thickness from <50 nm to ~7 μm. Recent literature reports that crystallinity of the Sb film can influence the photocathode sensitivity [143] and that a variation in crystallite sizes can affect the

energy bandgap [144]. These observations can explain the trend toward higher QE for thicker Sb films; namely, thicker films resulted in increased average crystallite and grain size, which could serve to reduce the energy band gap of the photocathodes.

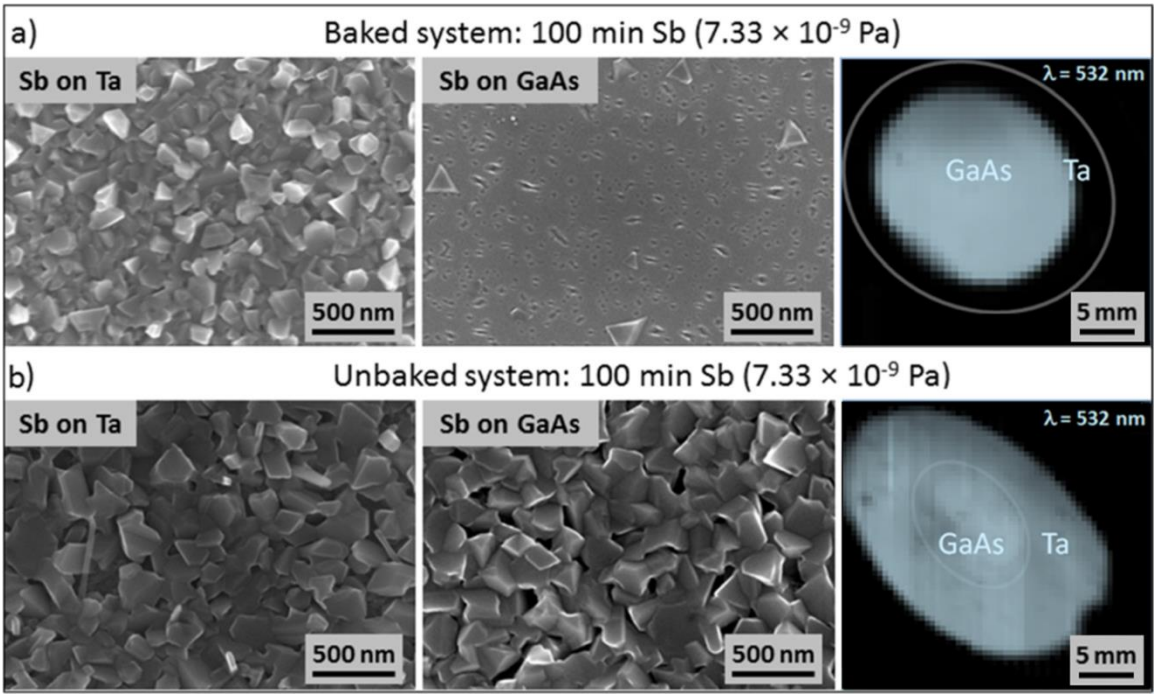


FIG. 4.7. FESEM topography and QE distribution of the photocathodes biased at 284 V with 532 nm (3.96 mW). The photocathodes were prepared by bialkali codeposition following the (a) vent-bake protocol on a 100 min grown Sb layer and (b) vent-no bake protocol on a 100 min grown Sb layer.

Others report QE of 10% and higher [36,145] for bialkali-antimonide photocathodes fabricated with very thin Sb layers (~15 nm); whereas our measured values were considerably lower for thin photocathodes. It is possible that for thin photocathodes, greater care must be taken when preparing the substrates. For example, typical alkali-antimonide photocathode recipes employing silicon substrates rely on the removal of native oxides via acid etching prior to the installation of the substrates within the deposition chamber [146]. It is well established that in order to remove

oxide and carbon contamination from the substrate surface, atomic hydrogen cleaning effectively improved the QE in GaAs:Cs photocathodes [147]. In this work, the GaAs substrates were removed from the vendor shipping containers, cleaved to size and then installed inside the deposition chamber without any further preparation. The Ta substrates were cleaned in an ultrasonic bath of acetone, followed by methanol, and then installed. Once inside the vacuum chamber, the substrates were routinely heated to 550 °C for 2 h prior to photocathode fabrication, which served to liberate weakly bound gas and contamination but could not effectively remove the native oxides.

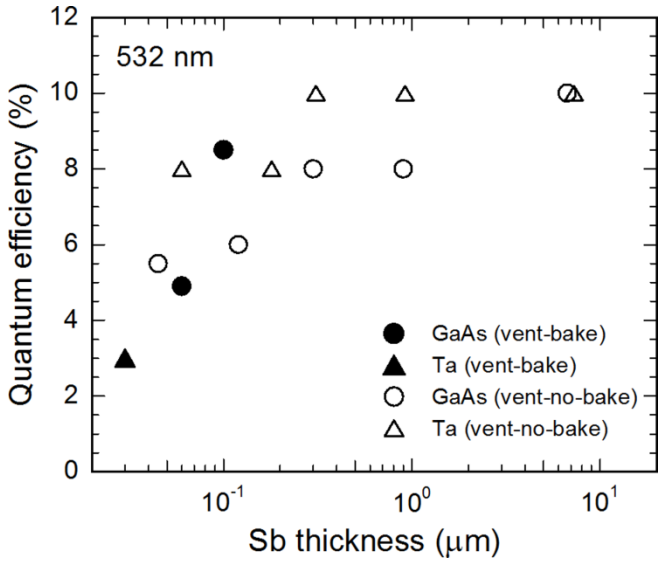


FIG. 4.8. QE as a function of Sb thickness for bialkali-antimonide photocathodes deposited on Ta and GaAs substrates. The photocathodes were biased at 284 V and illuminated with 4 mW of laser light at 532 nm.

It was relatively easy to obtain more QE data points following the vent-no-bake protocol as compared to the vent-bake protocol because the Sb growth was equally favored on both substrates and hence resulted in a similar Sb structure and morphology. This resulted in optimal

photocathode stoichiometry on both Ta and GaAs substrates simultaneously, for any Sb thickness. It was more challenging to obtain a full data set for the vent-bake vacuum protocol because the vent-bake condition provided dissimilar Sb films which made it difficult to optimize the QE on each substrate.

4.3.3. QE lifetime of photocathodes

The QE lifetime was evaluated for photocathodes manufactured under the vent-no-bake protocol by continuous illumination of photocathodes at a single location on each substrate, for an extended time period. All of the photocathodes depicted a decaying QE with time but at different rates [Fig. 4.9(a)]. During electron beam extraction from a photocathode under high bias voltage, QE decay is caused by different mechanisms such as ion bombardment and chemical poisoning of the activated photocathode surface [14]. Since our experiments were conducted at low voltage, chemical poisoning is likely to be the dominant mechanism to impact lifetime. The QE 1/e lifetimes obtained from the least square fit of the QE decay data are illustrated as a function of Sb thickness in Fig. 4.9(b). The QE lifetime for photocathodes grown on the GaAs substrate exhibited a power-law dependence on the Sb film thickness. The photocathode with the thickest Sb film (6.7 μm) provided the longest lifetime (~42 days). However, the lifetime results for photocathodes grown on the Ta substrates are inconclusive. The photocathode with a 300nm Sb film provided stable photocurrent at 200 μA for over 5 days. A photocurrent decay was experienced after 5 days only when a brief illumination interruption was made. This brief interruption enabled the estimation of the QE 1/e lifetime in excess of 90 days. However, for thicker Sb layers, the observed lifetime followed a similar trend as those grown on the GaAs substrate.

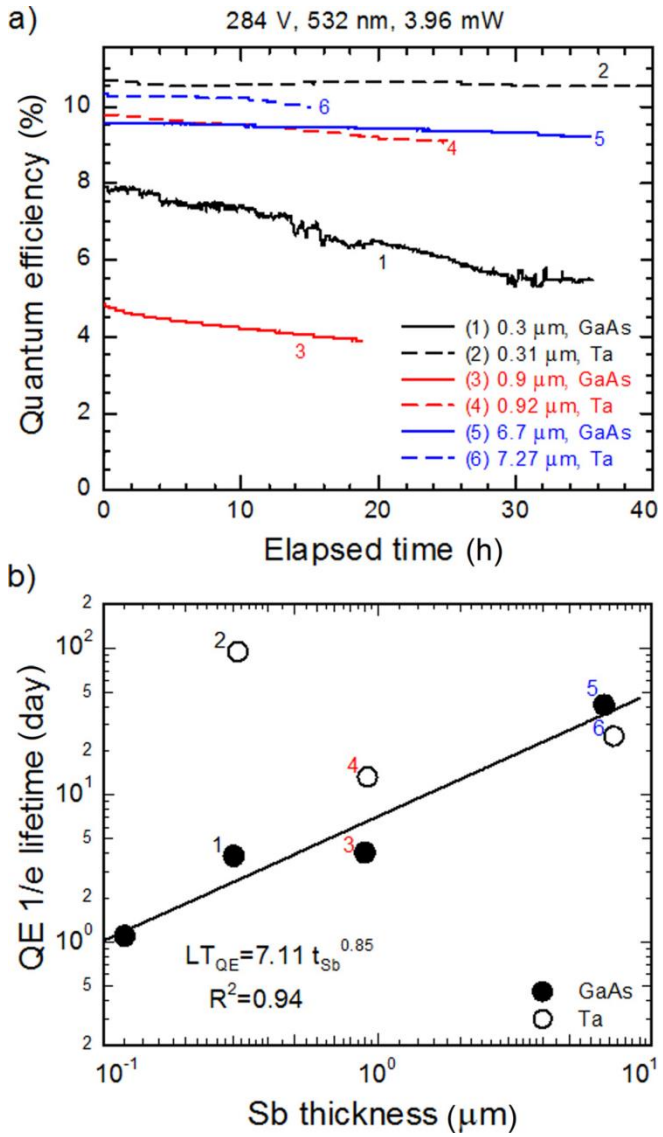


FIG. 4.9. (a) QE decay as a function of illumination time, (b) QE lifetime as a function of Sb thickness (t_{Sb}) for bialkali-antimonide photocathodes created under vent-no bake practice. The photocathodes were prepared by bialkali codeposition following the vent-no bake protocol and illuminated with 532 nm (3.96 mW) at 284 V bias.

4.3.4. Spectral response

The low power laser was replaced with the wavelength tunable light source to measure the QE as a function of wavelength from 425 to 825 nm [Fig. 4.10], for the photocathode with Sb layer of ~300 nm thickness (inset). For this photocathode, the highest QE from the Ta and GaAs

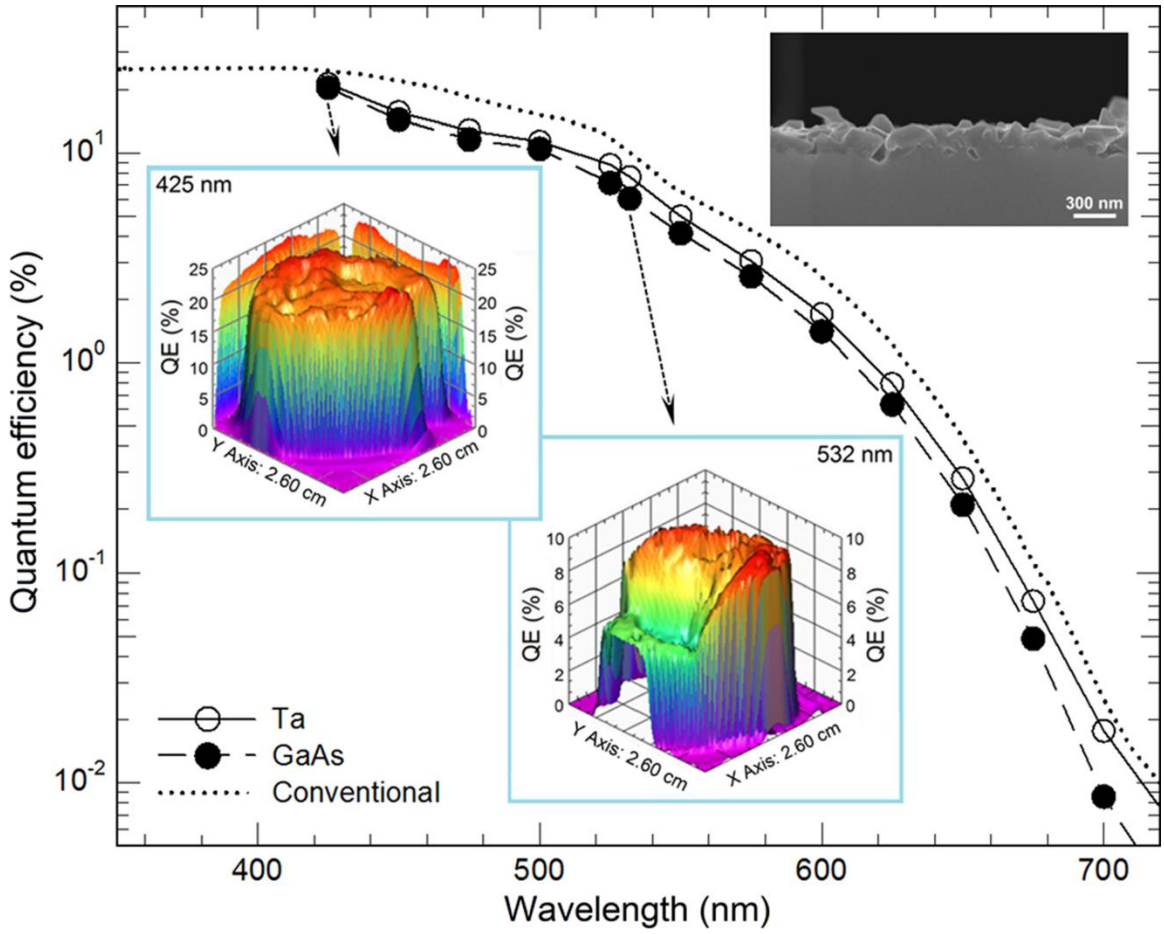


FIG. 4.10. (a) Spectral response of bialkali-antimonide photocathode deposited on Ta and GaAs substrates are shown together with the spectral response of conventional bialkali-antimonide photocathodes used in photomultiplier tubes. QE distribution is shown for 425 and 532 nm. The photocathode was prepared by bialkali codeposition on Sb layer of ~300 nm thickness deposition following the vent-no bake protocol.

substrates was 10% and 8% at 532 nm, and 24.2% and 22% at 425 nm, respectively. The QE distribution map at 532 nm depicted significant nonuniformity, which was due to an unintentional nonuniform chemical deposition. However, the effect of this spatial nonuniformity on QE distribution map appeared to minimize at 425 nm. This is likely because the effectiveness of light detection by a photocathode surface at different wavelength is known to depend on

photocathode stoichiometry [148]. Any variation in photocathode stoichiometry is expected to accompany a variation in bandgap energy which will result in the light absorption edge to vary [149] and in turn it can influence the photoelectron transport to the surface [150]. Furthermore, the stoichiometry of alkali-antimonide photocathodes varies as a function of depth from the expected CsK_2Sb composition due to varying diffusion of the alkali materials in the underlying Sb layer [151].

The obtained spectral response correlates well with the reference conventional curve [145] which represents a photocathode with very thin Sb layer (15 nm) [122]. This indicates a good stoichiometry of our photocathodes with thick Sb layers grown by codeposition of alkalis [152]. The codeposition thus enabled optimal stoichiometry of photocathodes with very thick Sb layers.

4.3.5. Correlations between Sb thickness, chemical consumption, and photocathode optical performance

The relative amount of source materials required for each photocathode was estimated by noting the duration of deposition, the partial pressure of each chemical species as indicated by the RGA, and using the following formula:

$$Q = \frac{t \times P}{t_o \times P}, \tag{4.3}$$

where Q represents the normalized quantity of a particular chemical species relative to the Cs amount applied to the photocathode manufactured with the thinnest Sb layer (denoted by the index o); t represents the time duration of depositions; and P is the partial pressure detected by the RGA. Figure 4.11 exhibits a strong correlation between the chemical requirements and the Sb

thickness. The Sb thickness and the required quantity of Cs and K increased exponentially with the applied amount of Sb. The required quantity of Cs and K also exhibited a power-law dependence on the Sb film thickness.

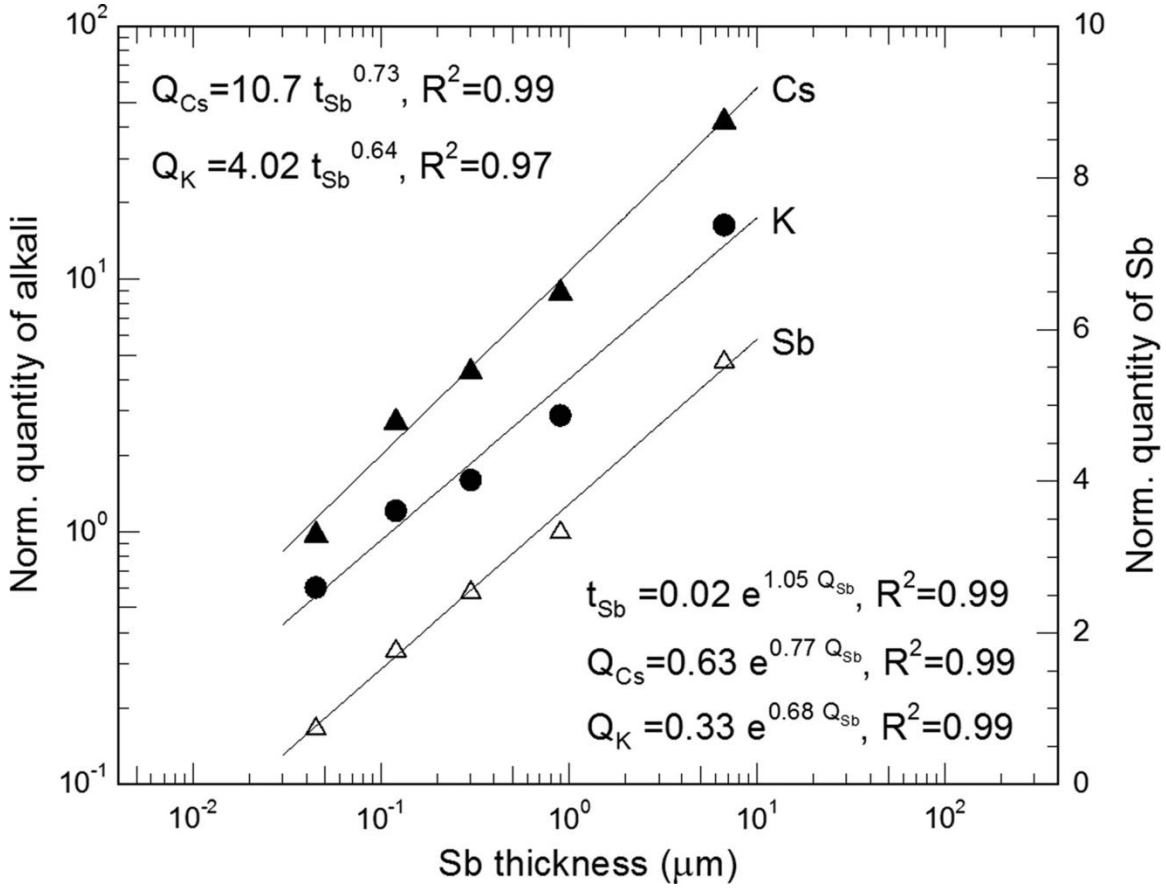


FIG. 4.11. Normalized quantity (Q) of source materials for optimal QE as a function of Sb thickness (t_{Sb}) for bialkali-antimonide photocathodes manufactured via codeposition of alkali species.

To explain some of the observations reported here, we speculate that photocathode performance using relatively thick Sb layers depends heavily on the surface morphology of the Sb film. In general, thin Sb films are smooth and dense compared to thicker Sb films that exhibit a high degree of roughness and porosity. Initially, the Sb films formed amorphous layers with

discontinuous nucleation of grains. With further addition of Sb, the nucleation saturation occurred and a full surface coverage by Sb grains was obtained. The film subsequently grew increasingly thicker and exhibited larger grain structure with increased intergranular voids (Figs. 4.2, 4.4, and 4.5), which served to increase the total surface area of Sb grains. The required amount of alkali materials for optimum QE will depend on the ratio of the effective surface area to the volume of Sb. It is clear that thicker layers of Sb served to "store" more alkalis. The QE lifetime results shown in Fig. 4.9(b) indicated that photocathodes with more alkali storage provided longer lifetime in a manner similar to that of porous substrates used in dispenser photocathodes [153], which served as an alkali-reservoir.

The increase in lifetime with respect to an increase in Sb thickness can be attributed to the increasing ability of the photocathodes to replenish the depleted alkali species from the top surface over time. For Cs-based photocathodes, the QE decay can be attributed to the loss of Cs (Ref. 142) from the convoluted effect of electron induced gas desorption [154] or ion bombardment (in dc guns) and the susceptibility of surface coating to evaporation [153]. The probable other factor with minor influence on the QE lifetime is the effect of the seasoning of the wall of the chamber in terms of water partial pressure reduction during a series of activation. The alkali coating on the chamber structure acted as a getter for water which can poison a Cs based photocathode [155,156]. This observation supports the reported fact that the photocathode lifetimes usually increase when the region surrounding the photocathode becomes coated with Cs after successive activation [157].

4.4. CONCLUSION

Antimony films grown on Ta and GaAs substrates were studied under different vacuum and deposition conditions, to better understand growth characteristics and their effect on photocathode QE and lifetime at low voltage. A field emission scanning electron microscope was used to evaluate the Sb-layer morphology as a function of Sb-layer thickness and to correlate the latter with partial pressures registered by the RGA. This allowed us to use the RGA as a chemical deposition rate monitor. Thin Sb layers provided a relatively dense smooth surface, whereas thick Sb layers appeared porous with increased surface roughness. Vacuum conditions affected the growth of Sb differently on different substrates, but with degraded vacuum this difference was minimized. The Sb films grew easily into polycrystalline form. The grain enlargement, an increase in the surface roughness, and the crystallite size enlargement were associated with increasing Sb film thickness.

Subsequent to the Sb-film characterization, the bialkali-antimonide photocathodes were fabricated by codeposition of K and Cs by means of an effusion source onto the Sb films of varying thickness. The Ta and GaAs substrates with Sb films of comparable thickness showed similar QE from ~3% to 10% for photocathodes with Sb layer thickness ranging from <50 nm to ~7 μm. A variation in the QE in the samples was attributed to the convoluted effect of structural variation, nonuniformity in chemical deposition, and substrate cleaning requirement that could affect the energy bandgap. We believe that the codeposition supported the formation of QE-optimized photocathodes when thick Sb layers were used, compared to those manufactured using sequential deposition. The performance of photocathodes was correlated with the Sb thickness and alkali consumption, where porous and thick Sb layers exhibited the best lifetime at low

voltage. The high-capacity effusion source enabled us to successfully manufacture alkali-antimonide photocathodes having maximum QE ~10% and extended low voltage lifetime (>90 days) at 532 nm. These results are encouraging for this bialkali-antimonide thin film photocathodes for their potential application in ultra-bright accelerator electron sources where high average currents with extended operation life are crucial requirements. We speculate that the Sb layer served as a reservoir, or sponge, for the alkali materials in the bialkali-antimonide photocathodes. Photocathodes such as these will be tested inside a dc high voltage photogun in future, where we expect to correlate some of the observations reported here, with measurements of photocathode lifetime at high voltage and beam quality including beam emittance.

One of the frequently asked questions related to bialkali-antimonide photocathodes is whether some amount of contamination in CsK_2Sb serves a beneficial role [131] in the chemical processes that govern bialkali-antimonide photocathode formation. This work illustrates that strict vacuum protocols (i.e., baking) are not absolutely essential, but it does not specify limits on the partial pressure of different gas species, including water vapor. A worthy follow up study could explore the impact of different gas species on bialkali-antimonide photocathode formation, with gas species like water vapor, introduced into the vacuum chamber in a more controlled manner.

CHAPTER 5

CONCLUSIONS

5.1. SUMMARY

This dissertation investigated potential applications of thin-films toward significant improvement in the performance of photoelectron guns, to meet the challenges of the worldwide accelerator community. Vacuum, field emission and photocurrent are important aspects of photogun technology. Three complementary studies were performed to explore how suitable thin-films could be used to improve photogun vacuum and thereby prolong operation, eliminate field emission from high voltage electrodes, and obtain high average current photocathodes.

In the first experiment, the outgassing rates of three nominally identical 304L stainless steel vacuum chambers were measured to determine the effect of chamber coatings and heat treatments. One chamber was coated with titanium nitride (TiN) and one with amorphous silicon (a-Si) immediately following fabrication. The last chamber was first tested without any coating and then coated with a-Si following a series of heat treatments. The outgassing rate of each chamber was measured at room temperatures between 15 and 30 °C following bakes at temperatures between 90 and 400 °C. The outgassing results were discussed in terms of diffusion-limited versus recombination-limited processes. Measurements for bare steel showed a significant reduction in the outgassing rate by nearly a factor of 20 after a 400 °C heat treatment (3.5×10^{-12} Torr L s^{-1} cm^{-2} prior to heat treatment, reduced to 1.7×10^{-13} Torr L s^{-1} cm^{-2} following heat treatment). Our studies suggest that once low outgassing rates have been achieved, baking

a stainless steel vacuum chamber at 250 °C in the recombination limited regime is detrimental to the outgassing rate. The chambers that were coated with a-Si showed minimal change in outgassing rates with heat treatment, though an outgassing rate reduced by heat treatments prior to a-Si coating was successfully preserved throughout a series of bakes. The results from both of the a-Si chambers suggest the coating is indeed hydrophobic compared to bare stainless steel, with outgassing rates in the low 10^{-12} Torr L s^{-1} cm^{-2} range obtained following bakes at only 90 °C. The results also indicate that once the chamber has been coated with amorphous silicon, additional heat treatment does not reduce the outgassing rate; however, a chamber that was heat treated prior to coating preserves the reduced outgassing rate following coating much better than uncoated steel. We conclude that the outgassing rate for the a-Si chamber is strongly dominated by surface effects rather than by the rate of diffusion of hydrogen in the bulk stainless steel. The TiN coated chamber exhibited remarkably low outgassing rates, up to four orders of magnitude lower than the uncoated stainless steel, but the uncertainty in these rates is large due to the sensitivity limitations of the spinning rotor gauge accumulation measurement and the possibility of a small pump speed due to inhomogeneity in the TiN coating.

In the second experiment, the high voltage performance of three TiN-coated aluminum electrodes, before and after gas conditioning with helium, was compared to that of bare aluminum electrodes, and electrodes manufactured from titanium alloy (Ti-6Al-4V). Preparing electrodes made of metals like stainless steel, for use inside DC high voltage electron guns, is a labor-intensive and time-consuming process. This study demonstrated the exceptional high voltage performance of aluminum electrodes coated with hard titanium nitride (TiN). The aluminum electrodes were comparatively easy to manufacture and required only hours of

mechanical polishing using silicon carbide paper prior to coating with TiN by a commercial vendor. The high voltage performance of three TiN-coated aluminum electrodes, before and after gas conditioning with helium, was compared to that of bare aluminum electrodes, and electrodes manufactured from titanium alloy (Ti-6Al-4V). Following gas conditioning, each TiN-coated aluminum electrode reached −225 kV bias voltage while generating less than 100 pA of field emission (<10 pA) using a 40 mm cathode/anode gap, corresponding to field strength of 13.7 MV/m. Smaller gaps were studied to evaluate electrode performance at higher field strength with the best performing TiN-coated aluminum electrode reaching ~22.5 MV/m with field emission less than 100 pA. These results were comparable to those obtained from our best-performing electrodes manufactured from stainless steel, titanium alloy and niobium. The TiN coating provided a very smooth surface and with mechanical properties of the coating (hardness and modulus) superior to those of stainless steel, titanium-alloy, and niobium electrodes. These features likely contributed to the improved high voltage performance of the TiN-coated aluminum electrodes.

In the third experiment, the effect of antimony thickness on the performance of bialkali-antimonide photocathodes was studied. The alkali species Cs and K were codeposited using an effusion source, onto relatively thick layers of Sb (50 nm to ~7 μm) grown on GaAs and Ta substrates inside a vacuum chamber that was baked and not-vented, and also baked and vented with clean dry nitrogen but not rebaked. The characteristics of the Sb films, including sticking probability, surface roughness, grain size, and crystal properties were very different for these conditions, yet comparable values of photocathode yield [or quantum efficiency (QE)] were obtained following codeposition of the alkali materials. The high-capacity effusion source

enabled us to successfully manufacture photocathodes having maximum QE around 10% and extended low voltage 1/e lifetime (>90 days) at 532 nm via the co-deposition method, with relatively thick layers of antimony (≥300 nm). We speculate that alkali co-deposition provides optimized stoichiometry for photocathodes manufactured using thick Sb layers, which could serve as a reservoir for the alkali.

In conclusion, this research investigated thin films for their potential applications in DC high voltage photoelectron guns to provide ultra-bright electron beams. The outgassing rate measurements on amorphous silicon and titanium nitride thin films indicates that these thin films can be used on photogun chambers to reduce the gas load and improve the pump speed to meet the extreme high vacuum, a critical requirement for ultra-bright photoguns. The field emission investigation demonstrated that a thin titanium nitride film on aluminum electrodes can effectively eliminate high voltage induced field emission by providing a smooth surface finish and higher work function at reduced expense. Finally, the photocathode preparation is optimized for high quantum yield bialkali-antimonide photocathodes for their extended operational lifetime. Simultaneous implementation of these thin films can significantly improve photogun performance to potentially meet the challenges of future ultra-bright accelerator electron sources.

5.2. FUTURE WORK

The encouraging results of the three studies conducted in this dissertation demand follow-up. Future investigations should include the following.

1. Effects of heat treatment on the outgassing rate of multilayer coating with a-Si on TiN applied on stainless steel chambers. The multi-step coating process would involve application of TiN

coating followed by degassing at 400 C for 1 day, and finally the application of a-Si coating. The intermediate TiN layer with a small pump speed can result in achieving very low outgassing rate from a-Si coating. This may result in quick and permanent attainment of XHV in a vacuum system without need of high temperature bake during operation in scenarios of repeated venting to air.

2. Field emission characterization of Al electrode coated with physical vapor deposited (PVD) TiN under DC high Voltage. PVD is a common commercial coating process which allows cost effective coating of larger structures. The PVD coating is expected to result in rougher topography than the IBED coating. The investigation would include the application of PVD TiN coatings on Al electrodes using commercial vendors and compare the high voltage field emission performance of IBED TiN coated Al electrodes studied in this dissertation. Findings form this study will lead to better understanding on the competing influence of surface characteristics (i.e., roughness) and the electronic characteristics (i.e., bandgap energy) of the coating on the field emission phenomena.
3. Study bialkali-antimonide photocathodes similar to the ones investigated in this dissertation for the characterization of beam emittance, field emission, and thermionic emission under DC high voltage. Findings of this investigation would assist in correlating thickness (i.e., roughness or grain size) with beam emittance and field emission.
4. Effects of varying evaporation rates of individual alkali during fabrication of bialkali-antimonide photocathodes and investigate its influence on the photocathode performance (i.e., QE, 1/e lifetime, and spectral response). Outcome of this investigation would lead to the optimal stoichiometry for high performance photocathode.

5. Effects of individual gas components (i.e., H_2O, O_2, etc.) present during photocathode fabrication on the performance of bialkali-antimonide photocathodes. This investigation would require controlled introduction of individual gas components during photocathode fabrication following a specific rate of alkali evaporation. This study would identify the gas components that act as contaminants and which should be avoided for successful photocathode manufacturing.
6. Verification of antimony sponge hypothesis by preparing the bialkali-antimonide photocathodes using codeposition of alkali on bulk antimony discs or foils as a function of porosity. Pure antimony discs can be mechanically polished to give mirror finish in order to minimize the surface roughness of the photocathode. We speculated based on our current study that the thick Sb layers serves as a sponge or reservoir for the alkali and have influence on the photocathode lifetime. Successful fabrication of bialkali-antimonide by deposition of alkali directly on Sb substrate has potential for extraordinary long lifetime.
7. Effects of background pressure during alkali deposition on the bialkali-antimonide photocathode performance. This study would involve application of alkali under different background pressures on pre-deposited Sb films made under identical conditions, and then compare the photocathode performance (i.e., QE, 1/e lifetime, and spectral response). Background pressure is responsible for determining the mean free-path of evaporated particles in the vacuum and would affect the extent of contamination with poisonous gas species in the vacuum. This study would reveal the ideal background pressure for successful photocathode fabrication.

REFERENCES

[1] R. Mehnert, Nucl. Instrum. Method B **113**, 81 (1996).

[2] *Electron Beam Technology*, edited by R. Bakish (John Wiley & Sons, New York, 1962).

[3] A. V. Deore, B. J. Patil, V. N. Bhoraskar, and S. D. Dhole, Indian J. Pure Ap. Phy. **50**, 482 (2012).

[4] *Reviews of Accelerator Science and Technology: Vol 1*, edited by A. W. Chao and W. Chou (World Scientific Publishing, Exeter, UK, 2009).

[5] R. Scott Kemp, Science & Global Security **13**, 183 (2005).

[6] S. K. Mahapatra, S. D. Dhole, and V. N. Bhoraskar, Nucl. Instrum. Method A **536**, 222 (2005).

[7] R. O'Rourke, "Navy shipboard lasers for surface, air, and missile defense: background and issues for congress," Congressional Research Service Report, R51426, June 12, 2015, e-print https://fas.org/sgp/crs/wea-pons/R41526.pdf.

[8] How Particle Accelerators Work, article on U.S. Department of Energy's web portal, http://energy.gov/articles/how-particle-accelerators-work.

[9] C. K. Sinclair, *High voltage DC photoemission electron guns – current status and technical challenges*, ICFA Beam Dynamics Newsletter, No. 46, issue editor: M. A. Furman, chief editor: W. Chou (Sponsored by the particles and fields commission of IUPAP, August 2008), e-print http://icfa-usa.jlab.org/archive/newsletter/icfa_bd_nl_46 .pdf

[10] C. Y. Prescott *et al*., Phys. Lett. B **77**, 347 (1978).

[11] C. K. Sinclair and R. H. Miller, IEEE Trans. Nucl. Sci. **28**, 2649 (1981).

[12] C. H. Lee, P. E. Oettinger, E. R. Pugh, R. Klinkowstein, J. H. Jacob. J. S. Fraser, and R. L. Sheffield, IEEE Trans. Nucl. Sci. **32**, 3045 (1988).

[13] J. S. Fraser, R. L. Sheffield, E. R. Gray, P. M. Giles, R. W. Springer, and V. A. Loebs, IEEE Trans. Nucl. Sci. **34**, 1705 (1987).

[14] C. K. Sinclair, P. A. Adderley, B. M. Dunham, J. C. Hansknecht, P. Hartmann, M. Poelker, J. S. Price, P. M. Rutt, W. J. Schneider, and M. Steigerwald, Phys. Rev. Spec. Top.-Accel. **10**, 023501 (2007).

[15] S. Abeyratne *et al*., *Science requirements and conceptual design for a polarized medium energy electron-ion collider at Jefferson lab*, edited by Y. Zhang and J. Bisognano (September 2012), e-print arXiv:1209.0757 [physics.acc-ph].

[16] E. C. Achenauer *et al*., "eRHIC Design Study: An Electron-Ion Collider at BNL," (July 2014), e-print arXiv:1409.1633 [physics.acc-ph].

[17] K. Aulenbacher *et al*., Nucl. Instrum. Method A **391**, 498 (1997).

[18] P. A. Adderley, J. Clark, J. Grames, J. Hansknecht, K. Surles-Law, D. Machie, M. Poelker, M. L. Stutzman, and R. Suleiman, Phys. Rev. Spec. Top.-Accel. **13**, 010101 (2010).

[19] R. V. Latham, *High Voltage Vacuum Insulation*, 2nd ed. (Academic, London, 1995).

[20] I. V. Bazarov, B. M. Dunham, and C. K. Sinclair, Phys. Rev. Lett. **102**, 104801 (2009).

[21] *The Physics and Applications of High Brightness Electron Beams*, edited by J. Rosenzweig, G. Travish and L. Serafini (World Scientific, Singapore, 2003).

[22] I. V. Bazarov and C. K. Sinclair, Phys. Rev. Spec. Top.-Accel. **8**, 034202 (2005).

[23] C. K. Sinclair, *Proceedings of PAC2003*, Portland, Oregon, USA, MOPB006 (2003), p. 76; http://accelconf.web.cern.ch/AccelConf/p03/papers/mopb006.pdf.

[24] H. G. Andresen *et al*., *Proceedings of Workshop on Photocathodes for Polarized Electron Sources for Accelerators*, SLAC, Stanford, CA, USA, 1993, SLAC-R-432 (1994), p. 2.

[25] R. W. Wood, Phys. Rev. (series I) **5**, 1(1897); http://journals.aps.org/pri/pdf/10.1103/PhysRevSeriesI.5.1

[26] L. Merminga, D. R. Douglas, and G. A. Krafft, Annu. Rev. Nucl. Part. Sci. **53**, 387 (2003).

[27] M. BastaniNejad, A. A. Elmustafa, E. Forman, J. Clark, S. Covert, J. Grames, J. Hansknecht, C. Hernandez-Garcia, M. Poelker, and R. Suleiman, Nucl. Instrum. Method A **762**, 135 (2014)

[28] J. J. Francis, "SLC procedural note," FP-238-042-94 (1991) and modifications described in University of Illinois, Champaign, IL 1991; B. Dunham, "Notes on diamond paste polishing of stainless steel," Nuclear Physics Laboratory Technical Notes, 19 May 90 revised 23 July 92, University of Washington, Seattle, WA, 1992.

[29] C. Hernandez-Garcia *et al*., *Proceedings of the 26th International FEL Conference*, Trieste, Italy (2004), p. 558.

[30] Y. M. Saveliev, F. Jackson, J. Jones, and J. McKenzie, *Proceedings of IPAC2012*, New Orleans, Louisiana, USA, MOPPP023 (2012), p. 616.

[31] B. M. Dunham *et al*., *Proceedings of IPAC2012*, New Orleans, Louisiana, USA, MOOAA01 (2012), p. 20.

[32] K. Smolenski, I. Bazarov, B. Dunham, H. Li, Y. Li, X. Liu, D. Ouzounov, and, C. Sinclair, AIP Conf. Proc. **1149**, 1077 (2008).

[33] D. J. Holder, N. Bliss, J. A. Clarke, P. A. McIntosh, M. W. Poole, E. A. Seddon, and S. L. Smith, *Proceedings of EPAC2006*, Edinburgh, Scotland, MOPCH070 (2006), p. 187.

[34] D. H. Dowell, I. Bazarov, B. Dunham, K. Harkay, C. Hernandez-Garcia, R. Legg, H. Padmore, T. Rao, J. Smedley, and W. Wan, Nucl. Instrum. Method A **622**, 685 (2010).

[35] *Towards Advanced Electron Beam Brightness Enhancement and Conditioning*, edited by K. J. Kim, A white paper based on the ANL Theory Institute on Production of Bright Electron Beams held at Argonne National Laboratory, September 22-26, 2003, ANL/APS/LS-305 (February 2004.)

[36] D. H. Dowell, S. Z. Bethel, and K. D. Friddell, Nucl. Instrum. Method A **356**, 167 (1995).

[37] R. R. Mammei et al., Phys. Rev. Spec. Top.-Accel. **16**, 033401 (2013).

[38] J. Balewski *et al*., "DarkLight: A search for dark forces at the Jefferson laboratory free-electron laser facility," (July 2013), e-print arXiv:1307.4432v2 [physics.ins-det].

[39] A. W. Thomas, "An electron-ion collider at Jefferson lab," (July 2009), e-print arXiv:0907.4785v1 [hep-ex].

[40] J. L. McCarter, T. Rao, J. Smedley, J. Grames, R. Mammei, M. Poelker, and R. Suleiman, *Proceedings of PAC11*, New York, NY, WEP284 (2011), p. 2017.

[41] T. Vecchione, I. Ben-Zvi, D. H. Dowell, J. Feng, T. Rao, J. Smedley, W. Wan and H. A. Padmore, Appl. Phys. Lett. **99**, 034103 (2011).

[42] L. Cultrera, I. Bazarov, J. Conway, B. Dunham, Y. Hwang, Y. Li, X. Liu, T. Moore, R. Merluzzi, K. Smolenski, S. Karkare, J.Maxson, and W. Schaff, *Proceedings of IPAC2012*, New Orleans, Louisiana, USA, WEOAB02 (2012), p. 2137.

[43] M. A. Mamun, A. A. Elmustafa, M. L. Stutzman, P. A. Adderley, and M. Poelker, J. Vac. Sci. Technol. A **32**, 021604 (2014).

[44] M. A. Mamun, A. A. Elmustafa, R. Taus, E. Forman, and M. Poelker, J. Vac. Sci. Technol. A **33**, 031604 (2015).

[45] M. A. Mamun, C. Hernandez-Garcia, M. Poelker, and A. A. Elmustafa, APL Mater. **3**, 066103 (2015).

[46] M. A. Mamun, A. A. Elmustafa, C. Hernandez-Garcia, R. Mammei, and M. Poelker, J. Vac. Sci. Technol. A **34**, 021509 (2016).

[47] M. L. Stutzman, P. Adderley, J. Brittian, J. Clark, J. Grames, J. Hansknecht, G. R. Myneni, and M. Poelker, Nucl. Instrum. Methods A **574**, 213 (2007).

[48] P. A. Redhead, "Extreme high vacuum, CERN Accelerator School on Vacuum Technology," CERN Rep. 99-05, 1999, p. 213.

[49] C. Benvenuti, Phys. Scr. **T22**, 48 (1988).

[50] R. Calder and G. Lewin, Br. J. Appl. Phys. **18**, 1459 (1967).

[51] M. Bernardini *et al.*, J. Vac. Sci. Technol. A **16**, 188 (1998).

[52] P. Marin, M. Dalinas, G. Lissolour, A. Marraud, and A. Reboux, Vacuum **49**, 309 (1998).

[53] C. D. Park, S. M. Chung, Xianghong Liu, and Yulin Li, J. Vac. Sci. Technol. A **26**, 1166 (2008).

[54] K. Odaka, Y. Ishikawa, and M. Furuse, J. Vac. Sci. Technol. A **5**, 2902 (1987).

[55] Y. Ishikawa and V. Nemanic, Vacuum **69**, 501 (2003).

[56] L. Westerberg, B. Hjörvarsson, E. Wallén, and A. Mathewson, Vacuum **48**, 771 (1997).

[57] Y. Tito Sasaki, J. Vac. Sci. Technol. A **25**, 1309 (2007).

[58] K. Jousten, Vacuum **49**, 359 (1998).

[59] F. Iacoviello, J. Galland, and M. Habashi, Corros. Sci. **40**, 1281 (1998).

[60] J. K. Fremery, Vacuum **53**, 197 (1999).

[61] J. P. Bacher, C. Benvenuti, P. Chiggiato, M.-P. Reinert, S. Sgobba, and A.-M. Brass, J. Vac. Sci. Technol. A **21**, 167 (2003).

[62] H. F. Dylla, D. M. Manos, and P. H. LaMarche, J. Vac. Sci. Technol. A **11**, 2623 (1993).

[63] T. Namba, M. Yamawaki, and M. Kanno, J. Nucl. Mater. **128–129**, 646 (1984).

[64] P. He, H. C. Hseuh, M. Mapes, R. Todd, D. Weiss, and D. Wilson, J. Vac. Sci. Technol. A **22**, 705 (2004).

[65] K. Saito, S. Inayoshi, Y. Ikeda, Y. Yang, and S. Tsukahara, J. Vac. Sci. Technol. A **13**, 556 (1995).

[66] S. Tsukahara, K. Saitoh, S. Inayoshi, and K. Onoe, Vacuum **43**, 1093 (1992).

[67] P. J. Kuzmenko, D. M. Behne, T. Casserly, W. Boardman, D. Upadhyaya, K. Boinapally, M. Gupta, and Y. Cao, Proc. SPIE **7018**, 701852 (2008).

[68] H. Akimichi and M. Hirata, Metrologia **42**, S184 (2005).

[69] K. H. Chung, S. K. Lee, Y. H. Shin, J. Y. Lim, S. S. Hong, and S. H. Be, Vacuum **53**, 303 (1999).

[70] T. Oishi, Y. Konishi, and M. Goto, J. Vac. Sci. Technol. A **21**, 1873 (2003).

[71] D. A. Smith, M. Higgins, and B. Kendall, presented at SVC Meeting, Restek/Elvac Laboratories (2005).

[72] C. Dong, P. Mehrotra, and G. R. Myneni, AIP Conf. Proc. **671**, 307 (2003).

[73] R. Checchetto, L. M. Gratton, A. Miotello, and C. Tosello, J. Non-Cryst. Solids **216**, 65 (1997).

[74] R. F. Chang and P. J. Abbott, J. Vac. Sci. Technol. A **25**, 1567 (2007).

[75] Micro Model 8790-00 liquid cleaner, Cole-Parmer Instrument Company, 7425 North Oak Park Ave, Niles, IL 60714. Detergent ultrasonic cleaning was followed by solvent rinses in acetone and methanol, then a rinse in DI water.

[76] SilcoTek, 112 Benner Circle, Bellefonte, PA 16823.

[77] Ionbond LLC, 7856 McCloud Rd., Greensboro, NC 27409.

[78] P. A. Redhead, J. Vac. Sci. Technol. A **20**, 1667 (2002).

[79] S. Ichimura, K. Kokubun, M. Hirata, S. Tsukahara, K. Saito, and Y. Ikeda, Vacuum **53**, 291 (1999).

[80] Y. Ishikawa, T. Yoshimura, and M. Aria, Vacuum **47**, 357 (1996).

[81] K. Odaka and S. Ueda, Vacuum **47**, 689 (1996).

[82] F. Watanabe, J. Vac. Sci. Technol. A **19**, 640 (2001).

[83] M. R. Louthan and R. G. Derrick, Corros. Sci. **15**, 565 (1975).

[84] P. J. Jennings, J. C. L. Cornish, B. W. Clare, G. T. Hefter, and D. J. Santjojo, Thin Solid Films **310**, 156 (1997).

[85] M. L. Stutzman, P. A. Adderley, M. Poelker, and M. A. Mamun, *Proceedings of IPAC2015*, Richmond, VA, USA, WEPWI024, 3–8 May 2015, p. 3540.

[86] B. C. Moore, J. Vac. Sci. Technol. A **13**, 545 (1995).

[87] V. Nemanic and J. Setina, J. Vac. Sci. Technol. A **17**, 1040 (1999).

[88] D. M. Grant, D. L. Cummings, and D. A. Blackburn, J. Nucl. Mater. **149** 180 (1987).

[89] G. P. Beukema, Physica **61**, 259 (1972).

[90] D. W. Williams and W. T. Williams, J. Phys. D: Appl. Phys. **6**, 734 (1973).

[91] E. Mahner, P. Kneisel, N. Pupeter, and G. Muller, *Proceedings of the 6th Workshop on Superconductivity*, CEBAF, Newport News, VA, 4–8 October 1993, p. 1085.

[92] M. BastaniNejad *et al.*, Phys. Rev. Spec. Top. Accel. Beams **15**, 083502 (2012).

[93] *Engineering Properties of Steels*, edited by P. D. Harvey (American Society for Metals, Materials Park, OH, 1982); D. Peckner and I. M. Bernstein, *Handbook of Stainless Steels* (McGraw-Hill, New York, 1977); *Metals Handbook*, edited by H. E. Boyer and T. L. Gall (American Society for Metals, Materials Park, OH, 1985); *Metals Handbook*, 10th ed. (ASM International, Materials Park, OH, 1990), Vol. 1.

[94] H. B. Michaelson, J. Appl. Phys. **48**, 4729 (1977).

[95] "Materials datasheet," Plansee USA LLC, Franklin, MA. See: http://www.plansee.com/en/Materials-13.htm.

[96] *Materials Properties Handbook: Titanium Alloys*, edited by R. Boyer, G. Welsch, and E. W. Collings (ASM International, Materials Park, OH, 1994); *Metals Handbook*, 10th ed., (ASM International, Materials Park, OH, 1990), Vol. 2; *Metals Handbook*, 9th ed., (ASM International, Materials Park, OH, 1980), Vol. 3; J. M. Holt, H. Mindlin, and C. Y. Ho, *Structural Alloys Handbook*, edited by C. Y. Ho (CINDAS/Purdue University, West Lafayette, IN, 1996).

[97] H. Ahmadi and M. Nouri, J. Mater. Sci. **45**, 3426 (2010).

[98] Information provided by The Aluminum Association, Inc., from Aluminum Standards and Data 2000 and/or International Alloy Designations and Chemical Composition Limits for Wrought Aluminum and Wrought Aluminum Alloys (Revised 2001); *Structural Alloys Handbook*, edited by C. Y. Ho (CINDAS/Purdue University, West Lafayette, IN, 1996);

Metals Handbook, edited by H. E. Boyer and T. L. Gall (American Society for Metals, Materials Park, OH, 1985).

[99] J. Westlinder, G. Sjöblom, and J. Olsson, Microelectron. Eng. **75**, 389 (2004).

[100] *Nanoengineering of Structural, Functional and Smart Materials*, edited by M. J. Schulz, A. D. Kelkar, and M. J. Sundaresan (CRC/Taylor & Francis Group, Boca Raton, FL, 2006), p. 535.

[101] K. Kawabata and T. Muto, Electrocomponent Sci. Technol. **8**, 249 (1981).

[102] J. Maxson, I. Bazarov, B. Dunham, J. Dobbins, X. Liu, and K. Smolenski, Rev. Sci. Instrum. **85**, 093306 (2014).

[103] M. BastaniNejad, Field emission studies toward improving the performance of DC high voltage photoelectron guns, Ph.D. thesis (Old Dominion University, 2013), p. 49.

[104] M. BastaniNejad *et al.*, J. Vac. Sci.Technol. A **33**, 041401 (2015).

[105] Beam Alloy Technology LLC, 8270 Estates Pkwy, Plain City, OH 43064.

[106] K. Halbach, Technical Report No. UCRL-17436 Lawrence Livermore National Laboratory, University of California, Livermore, CA, 1967.

[107] C. K. Sinclair, ICFA Newsl. **46**, 97 (2008).

[108] W. C. Oliver and G. M. Pharr, J. Mater. Res. **19**, 3 (2004).

[109] J. Hay, P. Agee, and E. Herbert, Exp. Technol. **34**, 86 (2010).

[110] G. Hua and D. Li, Phys. Status Solidi B 249, 1517 (2012).

[111] V. Anastassopoulos *et al.*, *A Storage Ring Experiment to Detect a Proton Electric Dipole Moment* (February 2015), e-print arXiv:1502.04317.

[112] Y. K. Semertzidis, *Proceedings of the DPF-2011 Conference*, Providence, RI, 8–13 August (2011).

[113] R. Mirzoyan, M. Laatiaoui, and M. Teshima, Nucl. Instrum. Method A **567,** 230 (2006).

[114] L. Cultrera *et al.*, Phys. Rev. Spec. Top.-Accel. **14,** 120101 (2011).

[115] S. H. Kong, J. Kinross-Wright, D. C. Nguyen, and R. L. Sheffield, Nucl. Instrum. Method A **358,** 272 (1995).

[116] R. Huang, D. Filippetto, C. F. Papadopoulos, H. Qian, F. Sannibale, and M. Zolotorev, Phys. Rev. Spec. Top.-Accel. **18,** 013401 (2015).

[117] A. Bartnik *et al.*, *Cornell ERL: Project Definition Design Report*, edited by G. H. Hoffstaetter, S. M. Gruner, and M. Tigner (Cornell University, New York, 2013).

[118] "Linac coherent light source II conceptual design report," https://portal.slac.stanford. edu/sites/lcls_public/lcls_ii/Published_Documents/CDR%20Index.pdf.

[119] V. Ptitsyn *et al.*, *Proceedings of EPAC 2004*, Lucerne, Switzerland (2004), p. 923.

[120] W. von. Drachenfels, F. Frommberger, M. Gowin, W. Hillert, M. Hoffmann, and B. Neff, AIP Conf. Proc. **675,** 1053 (2003).

[121] S. Benson *et al.*, Nucl. Instrum. Method A **582,** 14 (2007).

[122] J. Smedley *et al.*, *Proceedings of PAC2013*, Pasadena, California, USA, THPAC17 (2013), p.1178.

[123] D. E. Persyk, J. Morales, R. McKeighen, and G. Muehllehner, IEEE Trans. Nucl. Sci. **26,** 364 (1979).

[124] G. A. Condas and F. O. Wooten, J. Appl. Phys. **32,** 323 (1961).

[125] H. Levinstein, J. Appl. Phys. **20,** 306 (1949).

[126] M. Hashimoto, H. Sugibuchi, and K. Kambe, Thin Solid Films **98,** 197 (1982).

[127] N. Kaiser, Thin Solid Films **116,** 259 (1984).

[128] D. M. Dunham and C. K. Sinclair, "Charging the cesiator on the Illinois/CEBAF polarized electron source," NPL Polarized source Group Technical Note No. 90-9 (Nuclear Physics Laboratory, University of Illinois at Urbana-Champaign, IL, 1990).

[129] Alkali Metal Dispensers Brochure 1789, SAES getters, 20020 Lainate (MI) Italy (2007).

[130] W. E. Spicer and A. Herra-Gomez, "Modern theory and applications of photocathodes," SLAC-PUB-6306, August 1993, paper presented at the SPIE's 1993 International symposium on optics, imaging and instrumentation, San Diego, CA, USA, 11–16 July 1993.

[131] M. Succi, R. Canino, and B. Ferrario, Vacuum **35,** 579 (1985).

[132] B. M. van Oerle and G. J. Ernst, Nucl. Instrum. Method A **358,** 287 (1995).

[133] K. L. Jensen, D. W. Feldman, N. A. Moody, and P. G. O'Shea, J. Appl. Phys. **99,** 124905 (2006).

[134] NKT Photonics, "SuperK EXTREME supercontinuum lasers," http://www. Nktphotonics .com/ superkextreme.

[135] ICDD PDF Card No.: 01-085-1322.

[136] ICDD PDF Card No.: 01-077-3388.

[137] X. Liang *et al.*, *Proceedings of PAC2013*, Pasadena, California, USA, THPAC12 (2013), p.1163.

[138] B. D. Cullity and S. R. Stock, *Elements of X-ray Diffraction*, 3rd ed. (Prentice-Hall, NJ, 2001), p. 167.

[139] K. L. Lopez-Maldonado, P. de la Presa, M. A. de la Rubia, P. Crespo, J. deFrutos, A. Hernando, J. A. M. Aquino, and J. T. E. Galindo, J. Nanopart. Res. **16,** 2482 (2014).

[140] K. L. Chopra, *Thin Film Phenomena* (McGraw-Hill, New York, 1969).

[141] A. Braem, C. Joram, F. Piuz, E. Schyns, and J. Séguinot, Nucl. Instrum. Method A **502,** 205 (2003).

[142] A. H. Sommer, *Photoemissive Materials* (Wiley, New York, 1968).

[143] K. Nakamura, Y. Hamana, Y. Ishigami, and T. Matsui, Nucl. Instrum. Method A **623,** 276 (2010).

[144] V. P. Geetha Vani, M. Vasudeva Reddy, and K. T. Ramakrishna Reddy, ISRN Condens. Matter Phys. **2013,** 142029 (2013).

[145] M. Suyama, *Proceedings of Science*, Kobe, Japan, PD07 (2007), p. 018.

[146] M. Ruiz-Osés *et al.*, APL Mater. **2,** 121101 (2014).

[147] D.-A. Luh *et al.*, "Recent polarized photocathode R&D at SLAC," AIP Conf. Proc. **675,** 1029 (2003).

[148] G. S. Buller and R. J. Collins, Meas. Sci. Technol. **21,** 012002 (2010).

[149] M. A. Khan and R. G. Schulze, U.S. patent 4616248 (7 October 1986).

[150] "Development of high quantum efficiency UV/blue photocathode epitaxial semiconductor heterostructures for scintillation and Cherenkov radiation detection," Summary of Research, PI: Daniel J. Leopold, 7-15-200 to 7-14-2002, Washington University, NASA Grant No.: NAG5-8536.

[151] L. Xu-Dong, G. Qiang, Z. Meng, and Z. Ming-Hua, Chin. Phys. C **36,** 531 (2012).

[152] P. Michelato, Nucl. Instrum. Method A **393,** 455 (1997).

[153] E. J. Montgomery, D. W. Feldman, P. G. O'Shea, Z. Pan, N. Sennett, K. L. Jensen, and N. A. Moody, J. Directed Energy **3,** 66 (2008).

[154] D. Schultz *et al.*, "The high peak current polarized electron source of the Stanford Linear Collider," SLAC-PUB-6275, June 1993, paper presented at the workshop on high intensity electron sources, Legnaro, Padua, Italy, 24–28 May 1993.

[155] D. Durek, F. Frommberger, T. Reichelt, and M. Westermann, Appl. Surf. Sci. **143,** 319 (1999).

[156] T. Wada, T. Nitta, T. Nomura, M. Miyao, and M. Hagino, Jpn. J. Appl. Phys. **29,** 2087 (1990).

[157] *Atomic, Molecular: Optical Physics: Charged Particles*, Experimental Methods in the Physical Sciences, edited by F. B. Dunning and R. G. Hulet (Academic, San Diego, CA, 1998), Vol **29A**, p. 22.

APPENDIX A

PHENOMENOLOGICAL SIMILARITY ANALYSIS

Similarity of Fowler-Nordheim (F-N) Equation with temperature dependent outgassing rate or carrier mobility Equations

Outgassing rate:

$q \propto f(T)\mathrm{e}^{-E_D/RT}$ $\quad log(q) = log(\mathrm{A}.f(\mathrm{T})) - (\mathrm{E_D}/R).(1/\mathrm{T});\quad q\uparrow\Leftrightarrow \mathrm{T}\uparrow;\ (\Delta\, q/\Delta \mathrm{T})\uparrow\Leftrightarrow \mathrm{E_D}\uparrow$

Eg = $\mathrm{E_D}$ = Activation energy of diffusion limited outgassing

= reflects sensitivity of outgassing rate with temp variation

= media specific (H carrier density dependent) physical Prop.

y intercept $log(\mathrm{A})$ represents $log(q)_{max}$ as $\mathrm{T}\rightarrow\infty$

here A= media specific rate constant (i.e., physical property)

With baking we change both A and $\mathrm{E_D}$ (as we drive out H).

Semiconductor charge mobility rate:

$n_i \propto T^2\mathrm{e}^{-E_{gap}/k_BT}$ $\quad log(n_i) = log(\mathrm{A}.\mathrm{T}^2) - (\mathrm{E_g}/k_B).(1/\mathrm{T});\quad \mathrm{ni}\uparrow\Leftrightarrow\mathrm{T}\uparrow;\ (\Delta\, \mathrm{ni}/\Delta\mathrm{T})\uparrow\Leftrightarrow \mathrm{E_g}\uparrow$

Eg = Egap = Energy band gap

= reflects sensitivity of elec^{l} conductivity with temp variation

= media specific (carrier density dependent) physical property.

y intercept $log(A.f(T))$ represents $log(n_i)_{max}$ as $T \rightarrow \infty$

here A= media specific rate constant (i.e., physical property)

With annealing we change both A and E_g (as impurity & defect density and crystalline phases are affected by heating⇔ affect E_g).

Fowler-Nordheim electron tunneling rate in field emission:

$$\frac{I}{E^2} = J.A_e = C_1 A_e \beta^2 \exp(-\frac{C_2}{\beta E});\ C_1 = \frac{1.54\times10^{-6}\times10^{4.52\phi^{-0.5}}}{\phi}:\ C_2 = 6.53\times10^9 \phi^{1.5}:$$

$log(I/E^2) = log(C_1 A_e \beta^2) - (-E\varphi/\beta).(1/E)$; $I/E^2 \uparrow \Leftrightarrow E\uparrow$;

or, $log(I) = log(C_1 E^2 A_e \beta^2) - (-E\varphi/\beta).(1/E)$; $I\uparrow \Leftrightarrow E\uparrow$; $(\Delta I/\Delta E)\uparrow \Leftrightarrow C_2(=E_\varphi)\uparrow \Leftrightarrow \varphi\uparrow$

Eg = Eφ= φ = work function energy

= reflects sensitivity of current emission with field strength variation

= media specific (carrier density dependent) physical property.

y intercept $log(A_e \beta^2.f(E,\varphi))$ will represent $log(I)_{max}$ as $E \rightarrow \infty$

here $A = A_e \beta^2.f(\varphi)$ = media specific rate constant (i.e., physical property)

With gas conditioning and baking we change both A and φ (as we drive out electrical carriers, also heating associated change in φ).

Position of β in governing F-N Eq. is more similar to physical constants k_B or R.

Ideal gas constant *R* is expressed in units of energy (i.e. the pressure-volume product) per temperature increment per *mole.*

Boltzmann constant k_B is expressed in units of energy (i.e. the pressure-volume product) per temperature increment per *particle*.

Similarly, β should represent quantum energy per field strength (E, MV/m) increment per electron. It should be treated like a physical constant as K_B or *R*.

It would be interesting to make an attempt to use Boltman constant k_B in the Fowler-Nordheim equation to replace β and see if that helps us explain our HV results since k_B is ~10^{-23} and often we saw from our analyzed data that A_e can shift by an order of 23. We would likely find some manageable model to explain the field emission for electrodes rather than a single point field emitter for which Fowler-Nordheim is useful.

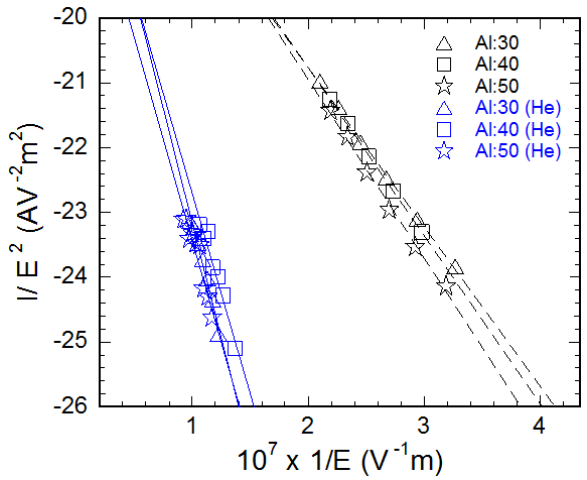


FIG. A. Fowler-Nordheim line plots for Al electrode before (dashed line) and after (solid line) helium processing based on high voltage test data for cathode/anode gap of 30, 40, and 50 mm.

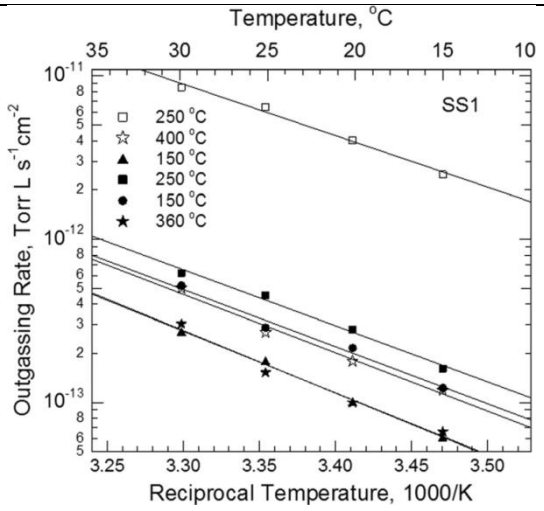


FIG. B. Outgassing rates for the bare stainless steel (SS1) chamber as a function of inverse room temperature, with each data set obtained following a bake at the temperature noted in the legend. The error bars for statistical and systematic errors are smaller than the data points for these data. The slope yields the temperature dependent activation energy as described in the text.

⇕	⇕
Lines shift with gas processing with diminishing effect.	Lines shift with each baking with diminishing effect.

HV processing itself also slightly affects the slope of the lines indicating its ability to slightly affect φ, similar to the role played by time of baking or similar to the effects of successive baking at the same temperature.

APPENDIX B

COPYRIGHT PERMISSIONS

Chapters two, three and four of this dissertation are based on works published in the Journal of Vacuum Science & Technology A. Those publications are listed chronologically:

1. M. A. Mamun, A. A. Elmustafa, M. L. Stutzman, P. A. Adderley, and M. Poelker, "Effect of heat treatments and coatings on the outgassing rate of stainless steel chambers," Journal of Vacuum Science & Technology A 32 (2), Mar/Apr 2014, 021604 (8 pages). DOI: 10.1116/1.4853795, (Published on 27 December 2013.)
2. M. A. Mamun, A. A. Elmustafa, R. Taus, E. Forman, and M. Poelker, "TiN Coated Aluminum Electrodes for DC High Voltage Electron Guns," Journal of Vacuum Science & Technology A 33 (3), May/Jun 2015, 031604 (10 pages). DOI: 10.1116/1.4916574, (Published on 1 April 2015.)
3. M. A. Mamun, A. A. Elmustafa, C. Hernandez-Garcia, R. Mammei, and M. Poelker, "Effect of Sb thickness on the performance of bialkali-antimonide photocathodes," Journal of Vacuum Science & Technology A 34 (2), Mar/Apr 2016, 021509 (14 pages). DOI: 10.1116/1.4939563, (Published on 6 January 2016.)

Copyright permissions are included in following pages.

AIP PUBLISHING LLC LICENSE
TERMS AND CONDITIONS

Mar 18, 2016

This Agreement between Jefferson Lab -- Md Abdullah Mamun ("You") and AIP Publishing LLC ("AIP Publishing LLC") consists of your license details and the terms and conditions provided by AIP Publishing LLC and Copyright Clearance Center.

License Number	3831740125072
License date	Mar 18, 2016
Licensed Content Publisher	AIP Publishing LLC
Licensed Content Publication	Journal of Vacuum Science & Technology A
Licensed Content Title	Effect of heat treatments and coatings on the outgassing rate of stainless steel chambers
Licensed Content Author	Md Abdullah A. Mamun,Abdelmageed A. Elmustafa,Marcy L. Stutzman, et al.
Licensed Content Date	Dec 27, 2013
Licensed Content Volume Number	32
Licensed Content Issue Number	2
Type of Use	Thesis/Dissertation
Requestor type	Author (original article)
Format	Print and electronic
Portion	Abstract
Number of Abstracts	1
Will you be translating?	No
Title of your thesis / dissertation	THIN FILM STUDIES TOWARD IMPROVING THE PERFORMANCE OF ACCELERATOR ELECTRON SOURCES
Expected completion date	May 2016
Estimated size (number of pages)	150
Requestor Location	Jefferson Lab Jefferson Lab 600 KELVIN DR STE 8 Newport News, VA 23606-4468 NEWPORT NEWS, VA 23606 United States Attn: Matthew Poelker
Billing Type	Invoice
Billing Address	Jefferson Lab Jefferson Lab 600 KELVIN DR STE 8 Newport News, VA 23606-4468 NEWPORT NEWS, VA 23606 United States

Attn: Matthew Poelker

Total 0.00 USD

Terms and Conditions

American Vacuum Society -- Terms and Conditions: Permissions Uses

American Vacuum Society ("AVS") hereby grants to you the non-exclusive right and license to use and/or distribute the Material according to the use specified in your order, on a one-time basis, for the specified term, with a maximum distribution equal to the number that you have ordered. Any links or other content accompanying the Material are not the subject of this license.

1. You agree to include the following copyright and permission notice with the reproduction of the Material:"Reprinted with permission from [FULL CITATION]. Copyright [PUBLICATION YEAR], American Vacuum Society." For an article, the copyright and permission notice must be printed on the first page of the article or book chapter. For photographs, covers, or tables, the copyright and permission notice may appear with the Material, in a footnote, or in the reference list.
2. If you have licensed reuse of a figure, photograph, cover, or table, it is your responsibility to ensure that the material is original to AVS and does not contain the copyright of another entity, and that the copyright notice of the figure, photograph, cover, or table does not indicate that it was reprinted by AVS, with permission, from another source. Under no circumstances does AVS, purport or intend to grant permission to reuse material to which it does not hold copyright.
3. You may not alter or modify the Material in any manner. You may translate the Material into another language only if you have licensed translation rights. You may not use the Material for promotional purposes. AVS reserves all rights not specifically granted herein.
4. The foregoing license shall not take effect unless and until AVS or its agent, Copyright Clearance Center, receives the Payment in accordance with Copyright Clearance Center Billing and Payment Terms and Conditions, which are incorporated herein by reference.
5. AVS or the Copyright Clearance Center may, within two business days of granting this license, revoke the license for any reason whatsoever, with a full refund payable to you. Should you violate the terms of this license at any time, AVS, American Vacuum Society, or Copyright Clearance Center may revoke the license with no refund to you. Notice of such revocation will be made using the contact information provided by you. Failure to receive such notice will not nullify the revocation.
6. AVS makes no representations or warranties with respect to the Material. You agree to indemnify and hold harmless AVS, American Vacuum Society, and their officers, directors, employees or agents from and against any and all claims arising out of your use of the Material other than as specifically authorized herein.
7. The permission granted herein is personal to you and is not transferable or assignable without the prior written permission of AVS. This license may not be amended except in a writing signed by the party to be charged.
8. If purchase orders, acknowledgments or check endorsements are issued on any forms containing terms and conditions which are inconsistent with these provisions, such inconsistent terms and conditions shall be of no force and effect. This document, including the CCC Billing and Payment Terms and Conditions, shall be the entire agreement between the parties relating to the subject matter hereof.

This Agreement shall be governed by and construed in accordance with the laws of the State of New York. Both parties hereby submit to the jurisdiction of the courts of New York County for purposes of resolving any disputes that may arise hereunder.

Questions? customercare@copyright.com or +1-855-239-3415 (toll free in the US) or +1-978-646-2777.

AIP PUBLISHING LLC LICENSE
TERMS AND CONDITIONS

Mar 18, 2016

This Agreement between Jefferson Lab -- Md Abdullah Mamun ("You") and AIP Publishing LLC ("AIP Publishing LLC") consists of your license details and the terms and conditions provided by AIP Publishing LLC and Copyright Clearance Center.

License Number	3831740236179
License date	Mar 18, 2016
Licensed Content Publisher	AIP Publishing LLC
Licensed Content Publication	Journal of Vacuum Science & Technology A
Licensed Content Title	Effect of heat treatments and coatings on the outgassing rate of stainless steel chambers
Licensed Content Author	Md Abdullah A. Mamun,Abdelmageed A. Elmustafa,Marcy L. Stutzman, et al.
Licensed Content Date	Dec 27, 2013
Licensed Content Volume Number	32
Licensed Content Issue Number	2
Type of Use	Thesis/Dissertation
Requestor type	Author (original article)
Format	Print and electronic
Portion	Excerpt (> 800 words)
Will you be translating?	No
Title of your thesis / dissertation	THIN FILM STUDIES TOWARD IMPROVING THE PERFORMANCE OF ACCELERATOR ELECTRON SOURCES
Expected completion date	May 2016
Estimated size (number of pages)	150
Requestor Location	Jefferson Lab Jefferson Lab 600 KELVIN DR STE 8 Newport News, VA 23606-4468 NEWPORT NEWS, VA 23606 United States Attn: Matthew Poelker
Billing Type	Invoice
Billing Address	Jefferson Lab Jefferson Lab 600 KELVIN DR STE 8 Newport News, VA 23606-4468 NEWPORT NEWS, VA 23606 United States Attn: Matthew Poelker

Total 0.00 USD

Terms and Conditions

American Vacuum Society -- Terms and Conditions: Permissions Uses

American Vacuum Society ("AVS") hereby grants to you the non-exclusive right and license to use and/or distribute the Material according to the use specified in your order, on a one-time basis, for the specified term, with a maximum distribution equal to the number that you have ordered. Any links or other content accompanying the Material are not the subject of this license.

1. You agree to include the following copyright and permission notice with the reproduction of the Material:"Reprinted with permission from [FULL CITATION]. Copyright [PUBLICATION YEAR], American Vacuum Society." For an article, the copyright and permission notice must be printed on the first page of the article or book chapter. For photographs, covers, or tables, the copyright and permission notice may appear with the Material, in a footnote, or in the reference list.
2. If you have licensed reuse of a figure, photograph, cover, or table, it is your responsibility to ensure that the material is original to AVS and does not contain the copyright of another entity, and that the copyright notice of the figure, photograph, cover, or table does not indicate that it was reprinted by AVS, with permission, from another source. Under no circumstances does AVS, purport or intend to grant permission to reuse material to which it does not hold copyright.
3. You may not alter or modify the Material in any manner. You may translate the Material into another language only if you have licensed translation rights. You may not use the Material for promotional purposes. AVS reserves all rights not specifically granted herein.
4. The foregoing license shall not take effect unless and until AVS or its agent, Copyright Clearance Center, receives the Payment in accordance with Copyright Clearance Center Billing and Payment Terms and Conditions, which are incorporated herein by reference.
5. AVS or the Copyright Clearance Center may, within two business days of granting this license, revoke the license for any reason whatsoever, with a full refund payable to you. Should you violate the terms of this license at any time, AVS, American Vacuum Society, or Copyright Clearance Center may revoke the license with no refund to you. Notice of such revocation will be made using the contact information provided by you. Failure to receive such notice will not nullify the revocation.
6. AVS makes no representations or warranties with respect to the Material. You agree to indemnify and hold harmless AVS, American Vacuum Society, and their officers, directors, employees or agents from and against any and all claims arising out of your use of the Material other than as specifically authorized herein.
7. The permission granted herein is personal to you and is not transferable or assignable without the prior written permission of AVS. This license may not be amended except in a writing signed by the party to be charged.
8. If purchase orders, acknowledgments or check endorsements are issued on any forms containing terms and conditions which are inconsistent with these provisions, such inconsistent terms and conditions shall be of no force and effect. This document, including the CCC Billing and Payment Terms and Conditions, shall be the entire agreement between the parties relating to the subject matter hereof.

This Agreement shall be governed by and construed in accordance with the laws of the State of New York. Both parties hereby submit to the jurisdiction of the courts of New York County for purposes of resolving any disputes that may arise hereunder.

Questions? customercare@copyright.com or +1-855-239-3415 (toll free in the US) or +1-978-646-2777.

AIP PUBLISHING LLC LICENSE
TERMS AND CONDITIONS

Mar 18, 2016

This Agreement between Jefferson Lab -- Md Abdullah Mamun ("You") and AIP Publishing LLC ("AIP Publishing LLC") consists of your license details and the terms and conditions provided by AIP Publishing LLC and Copyright Clearance Center.

License Number	3831740194826
License date	Mar 18, 2016
Licensed Content Publisher	AIP Publishing LLC
Licensed Content Publication	Journal of Vacuum Science & Technology A
Licensed Content Title	Effect of heat treatments and coatings on the outgassing rate of stainless steel chambers
Licensed Content Author	Md Abdullah A. Mamun,Abdelmageed A. Elmustafa,Marcy L. Stutzman, et al.
Licensed Content Date	Dec 27, 2013
Licensed Content Volume Number	32
Licensed Content Issue Number	2
Type of Use	Thesis/Dissertation
Requestor type	Author (original article)
Format	Print and electronic
Portion	Figure/Table
Number of figures/tables	12
Title of your thesis / dissertation	THIN FILM STUDIES TOWARD IMPROVING THE PERFORMANCE OF ACCELERATOR ELECTRON SOURCES
Expected completion date	May 2016
Estimated size (number of pages)	150
Requestor Location	Jefferson Lab Jefferson Lab 600 KELVIN DR STE 8 Newport News, VA 23606-4468 NEWPORT NEWS, VA 23606 United States Attn: Matthew Poelker
Billing Type	Invoice
Billing Address	Jefferson Lab Jefferson Lab 600 KELVIN DR STE 8 Newport News, VA 23606-4468 NEWPORT NEWS, VA 23606 United States Attn: Matthew Poelker

Total 0.00 USD

Terms and Conditions

American Vacuum Society -- Terms and Conditions: Permissions Uses

American Vacuum Society ("AVS") hereby grants to you the non-exclusive right and license to use and/or distribute the Material according to the use specified in your order, on a one-time basis, for the specified term, with a maximum distribution equal to the number that you have ordered. Any links or other content accompanying the Material are not the subject of this license.

1. You agree to include the following copyright and permission notice with the reproduction of the Material:"Reprinted with permission from [FULL CITATION]. Copyright [PUBLICATION YEAR], American Vacuum Society." For an article, the copyright and permission notice must be printed on the first page of the article or book chapter. For photographs, covers, or tables, the copyright and permission notice may appear with the Material, in a footnote, or in the reference list.
2. If you have licensed reuse of a figure, photograph, cover, or table, it is your responsibility to ensure that the material is original to AVS and does not contain the copyright of another entity, and that the copyright notice of the figure, photograph, cover, or table does not indicate that it was reprinted by AVS, with permission, from another source. Under no circumstances does AVS, purport or intend to grant permission to reuse material to which it does not hold copyright.
3. You may not alter or modify the Material in any manner. You may translate the Material into another language only if you have licensed translation rights. You may not use the Material for promotional purposes. AVS reserves all rights not specifically granted herein.
4. The foregoing license shall not take effect unless and until AVS or its agent, Copyright Clearance Center, receives the Payment in accordance with Copyright Clearance Center Billing and Payment Terms and Conditions, which are incorporated herein by reference.
5. AVS or the Copyright Clearance Center may, within two business days of granting this license, revoke the license for any reason whatsoever, with a full refund payable to you. Should you violate the terms of this license at any time, AVS, American Vacuum Society, or Copyright Clearance Center may revoke the license with no refund to you. Notice of such revocation will be made using the contact information provided by you. Failure to receive such notice will not nullify the revocation.
6. AVS makes no representations or warranties with respect to the Material. You agree to indemnify and hold harmless AVS, American Vacuum Society, and their officers, directors, employees or agents from and against any and all claims arising out of your use of the Material other than as specifically authorized herein.
7. The permission granted herein is personal to you and is not transferable or assignable without the prior written permission of AVS. This license may not be amended except in a writing signed by the party to be charged.
8. If purchase orders, acknowledgments or check endorsements are issued on any forms containing terms and conditions which are inconsistent with these provisions, such inconsistent terms and conditions shall be of no force and effect. This document, including the CCC Billing and Payment Terms and Conditions, shall be the entire agreement between the parties relating to the subject matter hereof.

This Agreement shall be governed by and construed in accordance with the laws of the State of New York. Both parties hereby submit to the jurisdiction of the courts of New York County for purposes of resolving any disputes that may arise hereunder.

Questions? customercare@copyright.com or +1-855-239-3415 (toll free in the US) or +1-978-646-2777.

AIP PUBLISHING LLC LICENSE
TERMS AND CONDITIONS

Mar 18, 2016

This Agreement between Jefferson Lab -- Md Abdullah Mamun ("You") and AIP Publishing LLC ("AIP Publishing LLC") consists of your license details and the terms and conditions provided by AIP Publishing LLC and Copyright Clearance Center.

License Number	3831740337405
License date	Mar 18, 2016
Licensed Content Publisher	AIP Publishing LLC
Licensed Content Publication	Journal of Vacuum Science & Technology A
Licensed Content Title	TiN coated aluminum electrodes for DC high voltage electron guns
Licensed Content Author	Md Abdullah A. Mamun,Abdelmageed A. Elmustafa,Rhys Taus, et al.
Licensed Content Date	Apr 1, 2015
Licensed Content Volume Number	33
Licensed Content Issue Number	3
Type of Use	Thesis/Dissertation
Requestor type	Author (original article)
Format	Print and electronic
Portion	Abstract
Number of Abstracts	1
Will you be translating?	No
Title of your thesis / dissertation	THIN FILM STUDIES TOWARD IMPROVING THE PERFORMANCE OF ACCELERATOR ELECTRON SOURCES
Expected completion date	May 2016
Estimated size (number of pages)	150
Requestor Location	Jefferson Lab Jefferson Lab 600 KELVIN DR STE 8 Newport News, VA 23606-4468 NEWPORT NEWS, VA 23606 United States Attn: Matthew Poelker
Billing Type	Invoice
Billing Address	Jefferson Lab Jefferson Lab 600 KELVIN DR STE 8 Newport News, VA 23606-4468 NEWPORT NEWS, VA 23606 United States Attn: Matthew Poelker

Total 0.00 USD

Terms and Conditions

American Vacuum Society -- Terms and Conditions: Permissions Uses

American Vacuum Society ("AVS") hereby grants to you the non-exclusive right and license to use and/or distribute the Material according to the use specified in your order, on a one-time basis, for the specified term, with a maximum distribution equal to the number that you have ordered. Any links or other content accompanying the Material are not the subject of this license.

1. You agree to include the following copyright and permission notice with the reproduction of the Material:"Reprinted with permission from [FULL CITATION]. Copyright [PUBLICATION YEAR], American Vacuum Society." For an article, the copyright and permission notice must be printed on the first page of the article or book chapter. For photographs, covers, or tables, the copyright and permission notice may appear with the Material, in a footnote, or in the reference list.
2. If you have licensed reuse of a figure, photograph, cover, or table, it is your responsibility to ensure that the material is original to AVS and does not contain the copyright of another entity, and that the copyright notice of the figure, photograph, cover, or table does not indicate that it was reprinted by AVS, with permission, from another source. Under no circumstances does AVS, purport or intend to grant permission to reuse material to which it does not hold copyright.
3. You may not alter or modify the Material in any manner. You may translate the Material into another language only if you have licensed translation rights. You may not use the Material for promotional purposes. AVS reserves all rights not specifically granted herein.
4. The foregoing license shall not take effect unless and until AVS or its agent, Copyright Clearance Center, receives the Payment in accordance with Copyright Clearance Center Billing and Payment Terms and Conditions, which are incorporated herein by reference.
5. AVS or the Copyright Clearance Center may, within two business days of granting this license, revoke the license for any reason whatsoever, with a full refund payable to you. Should you violate the terms of this license at any time, AVS, American Vacuum Society, or Copyright Clearance Center may revoke the license with no refund to you. Notice of such revocation will be made using the contact information provided by you. Failure to receive such notice will not nullify the revocation.
6. AVS makes no representations or warranties with respect to the Material. You agree to indemnify and hold harmless AVS, American Vacuum Society, and their officers, directors, employees or agents from and against any and all claims arising out of your use of the Material other than as specifically authorized herein.
7. The permission granted herein is personal to you and is not transferable or assignable without the prior written permission of AVS. This license may not be amended except in a writing signed by the party to be charged.
8. If purchase orders, acknowledgments or check endorsements are issued on any forms containing terms and conditions which are inconsistent with these provisions, such inconsistent terms and conditions shall be of no force and effect. This document, including the CCC Billing and Payment Terms and Conditions, shall be the entire agreement between the parties relating to the subject matter hereof.

This Agreement shall be governed by and construed in accordance with the laws of the State of New York. Both parties hereby submit to the jurisdiction of the courts of New York County for purposes of resolving any disputes that may arise hereunder.

Questions? customercare@copyright.com or +1-855-239-3415 (toll free in the US) or +1-978-646-2777.

AIP PUBLISHING LLC LICENSE
TERMS AND CONDITIONS

Mar 18, 2016

This Agreement between Jefferson Lab -- Md Abdullah Mamun ("You") and AIP Publishing LLC ("AIP Publishing LLC") consists of your license details and the terms and conditions provided by AIP Publishing LLC and Copyright Clearance Center.

License Number	3831740464962
License date	Mar 18, 2016
Licensed Content Publisher	AIP Publishing LLC
Licensed Content Publication	Journal of Vacuum Science & Technology A
Licensed Content Title	TiN coated aluminum electrodes for DC high voltage electron guns
Licensed Content Author	Md Abdullah A. Mamun,Abdelmageed A. Elmustafa,Rhys Taus, et al.
Licensed Content Date	Apr 1, 2015
Licensed Content Volume Number	33
Licensed Content Issue Number	3
Type of Use	Thesis/Dissertation
Requestor type	Author (original article)
Format	Print and electronic
Portion	Excerpt (> 800 words)
Will you be translating?	No
Title of your thesis / dissertation	THIN FILM STUDIES TOWARD IMPROVING THE PERFORMANCE OF ACCELERATOR ELECTRON SOURCES
Expected completion date	May 2016
Estimated size (number of pages)	150
Requestor Location	Jefferson Lab Jefferson Lab 600 KELVIN DR STE 8 Newport News, VA 23606-4468 NEWPORT NEWS, VA 23606 United States Attn: Matthew Poelker
Billing Type	Invoice
Billing Address	Jefferson Lab Jefferson Lab 600 KELVIN DR STE 8 Newport News, VA 23606-4468 NEWPORT NEWS, VA 23606 United States Attn: Matthew Poelker
Total	0.00 USD

Terms and Conditions

American Vacuum Society -- Terms and Conditions: Permissions Uses

American Vacuum Society ("AVS") hereby grants to you the non-exclusive right and license to use and/or distribute the Material according to the use specified in your order, on a one-time basis, for the specified term, with a maximum distribution equal to the number that you have ordered. Any links or other content accompanying the Material are not the subject of this license.

1. You agree to include the following copyright and permission notice with the reproduction of the Material:"Reprinted with permission from [FULL CITATION]. Copyright [PUBLICATION YEAR], American Vacuum Society." For an article, the copyright and permission notice must be printed on the first page of the article or book chapter. For photographs, covers, or tables, the copyright and permission notice may appear with the Material, in a footnote, or in the reference list.
2. If you have licensed reuse of a figure, photograph, cover, or table, it is your responsibility to ensure that the material is original to AVS and does not contain the copyright of another entity, and that the copyright notice of the figure, photograph, cover, or table does not indicate that it was reprinted by AVS, with permission, from another source. Under no circumstances does AVS, purport or intend to grant permission to reuse material to which it does not hold copyright.
3. You may not alter or modify the Material in any manner. You may translate the Material into another language only if you have licensed translation rights. You may not use the Material for promotional purposes. AVS reserves all rights not specifically granted herein.
4. The foregoing license shall not take effect unless and until AVS or its agent, Copyright Clearance Center, receives the Payment in accordance with Copyright Clearance Center Billing and Payment Terms and Conditions, which are incorporated herein by reference.
5. AVS or the Copyright Clearance Center may, within two business days of granting this license, revoke the license for any reason whatsoever, with a full refund payable to you. Should you violate the terms of this license at any time, AVS, American Vacuum Society, or Copyright Clearance Center may revoke the license with no refund to you. Notice of such revocation will be made using the contact information provided by you. Failure to receive such notice will not nullify the revocation.
6. AVS makes no representations or warranties with respect to the Material. You agree to indemnify and hold harmless AVS, American Vacuum Society, and their officers, directors, employees or agents from and against any and all claims arising out of your use of the Material other than as specifically authorized herein.
7. The permission granted herein is personal to you and is not transferable or assignable without the prior written permission of AVS. This license may not be amended except in a writing signed by the party to be charged.
8. If purchase orders, acknowledgments or check endorsements are issued on any forms containing terms and conditions which are inconsistent with these provisions, such inconsistent terms and conditions shall be of no force and effect. This document, including the CCC Billing and Payment Terms and Conditions, shall be the entire agreement between the parties relating to the subject matter hereof.

This Agreement shall be governed by and construed in accordance with the laws of the State of New York. Both parties hereby submit to the jurisdiction of the courts of New York County for purposes of resolving any disputes that may arise hereunder.

Questions? customercare@copyright.com or +1-855-239-3415 (toll free in the US) or +1-978-646-2777.

AIP PUBLISHING LLC LICENSE
TERMS AND CONDITIONS

Mar 18, 2016

This Agreement between Jefferson Lab -- Md Abdullah Mamun ("You") and AIP Publishing LLC ("AIP Publishing LLC") consists of your license details and the terms and conditions provided by AIP Publishing LLC and Copyright Clearance Center.

License Number	3831740423311
License date	Mar 18, 2016
Licensed Content Publisher	AIP Publishing LLC
Licensed Content Publication	Journal of Vacuum Science & Technology A
Licensed Content Title	TiN coated aluminum electrodes for DC high voltage electron guns
Licensed Content Author	Md Abdullah A. Mamun,Abdelmageed A. Elmustafa,Rhys Taus, et al.
Licensed Content Date	Apr 1, 2015
Licensed Content Volume Number	33
Licensed Content Issue Number	3
Type of Use	Thesis/Dissertation
Requestor type	Author (original article)
Format	Print and electronic
Portion	Figure/Table
Number of figures/tables	9
Title of your thesis / dissertation	THIN FILM STUDIES TOWARD IMPROVING THE PERFORMANCE OF ACCELERATOR ELECTRON SOURCES
Expected completion date	May 2016
Estimated size (number of pages)	150
Requestor Location	Jefferson Lab Jefferson Lab 600 KELVIN DR STE 8 Newport News, VA 23606-4468 NEWPORT NEWS, VA 23606 United States Attn: Matthew Poelker
Billing Type	Invoice
Billing Address	Jefferson Lab Jefferson Lab 600 KELVIN DR STE 8 Newport News, VA 23606-4468 NEWPORT NEWS, VA 23606 United States Attn: Matthew Poelker
Total	0.00 USD

Terms and Conditions

American Vacuum Society -- Terms and Conditions: Permissions Uses

American Vacuum Society ("AVS") hereby grants to you the non-exclusive right and license to use and/or distribute the Material according to the use specified in your order, on a one-time basis, for the specified term, with a maximum distribution equal to the number that you have ordered. Any links or other content accompanying the Material are not the subject of this license.

1. You agree to include the following copyright and permission notice with the reproduction of the Material:"Reprinted with permission from [FULL CITATION]. Copyright [PUBLICATION YEAR], American Vacuum Society." For an article, the copyright and permission notice must be printed on the first page of the article or book chapter. For photographs, covers, or tables, the copyright and permission notice may appear with the Material, in a footnote, or in the reference list.
2. If you have licensed reuse of a figure, photograph, cover, or table, it is your responsibility to ensure that the material is original to AVS and does not contain the copyright of another entity, and that the copyright notice of the figure, photograph, cover, or table does not indicate that it was reprinted by AVS, with permission, from another source. Under no circumstances does AVS, purport or intend to grant permission to reuse material to which it does not hold copyright.
3. You may not alter or modify the Material in any manner. You may translate the Material into another language only if you have licensed translation rights. You may not use the Material for promotional purposes. AVS reserves all rights not specifically granted herein.
4. The foregoing license shall not take effect unless and until AVS or its agent, Copyright Clearance Center, receives the Payment in accordance with Copyright Clearance Center Billing and Payment Terms and Conditions, which are incorporated herein by reference.
5. AVS or the Copyright Clearance Center may, within two business days of granting this license, revoke the license for any reason whatsoever, with a full refund payable to you. Should you violate the terms of this license at any time, AVS, American Vacuum Society, or Copyright Clearance Center may revoke the license with no refund to you. Notice of such revocation will be made using the contact information provided by you. Failure to receive such notice will not nullify the revocation.
6. AVS makes no representations or warranties with respect to the Material. You agree to indemnify and hold harmless AVS, American Vacuum Society, and their officers, directors, employees or agents from and against any and all claims arising out of your use of the Material other than as specifically authorized herein.
7. The permission granted herein is personal to you and is not transferable or assignable without the prior written permission of AVS. This license may not be amended except in a writing signed by the party to be charged.
8. If purchase orders, acknowledgments or check endorsements are issued on any forms containing terms and conditions which are inconsistent with these provisions, such inconsistent terms and conditions shall be of no force and effect. This document, including the CCC Billing and Payment Terms and Conditions, shall be the entire agreement between the parties relating to the subject matter hereof.

This Agreement shall be governed by and construed in accordance with the laws of the State of New York. Both parties hereby submit to the jurisdiction of the courts of New York County for purposes of resolving any disputes that may arise hereunder.

Questions? customercare@copyright.com or +1-855-239-3415 (toll free in the US) or +1-978-646-2777.

AIP PUBLISHING LLC LICENSE
TERMS AND CONDITIONS

Mar 18, 2016

This Agreement between Jefferson Lab -- Md Abdullah Mamun ("You") and AIP Publishing LLC ("AIP Publishing LLC") consists of your license details and the terms and conditions provided by AIP Publishing LLC and Copyright Clearance Center.

License Number	3831731135370
License date	Mar 18, 2016
Licensed Content Publisher	AIP Publishing LLC
Licensed Content Publication	Journal of Vacuum Science & Technology A
Licensed Content Title	Effect of Sb thickness on the performance of bialkali-antimonide photocathodes
Licensed Content Author	Md Abdullah A. Mamun,Abdelmageed A. Elmustafa,Carlos Hernandez-Garcia, et al.
Licensed Content Date	Jan 6, 2016
Licensed Content Volume Number	34
Licensed Content Issue Number	2
Type of Use	Thesis/Dissertation
Requestor type	Author (original article)
Format	Print and electronic
Portion	Abstract
Number of Abstracts	1
Will you be translating?	No
Title of your thesis / dissertation	THIN FILM STUDIES TOWARD IMPROVING THE PERFORMANCE OF ACCELERATOR ELECTRON SOURCES
Expected completion date	May 2016
Estimated size (number of pages)	150
Requestor Location	Jefferson Lab Jefferson Lab 600 KELVIN DR STE 8 Newport News, VA 23606-4468 NEWPORT NEWS, VA 23606 United States Attn: Matthew Poelker
Billing Type	Invoice
Billing Address	Jefferson Lab Jefferson Lab 600 KELVIN DR STE 8 Newport News, VA 23606-4468 NEWPORT NEWS, VA 23606 United States

Attn: Matthew Poelker

Total 0.00 USD

Terms and Conditions

American Vacuum Society -- Terms and Conditions: Permissions Uses

American Vacuum Society ("AVS") hereby grants to you the non-exclusive right and license to use and/or distribute the Material according to the use specified in your order, on a one-time basis, for the specified term, with a maximum distribution equal to the number that you have ordered. Any links or other content accompanying the Material are not the subject of this license.

1. You agree to include the following copyright and permission notice with the reproduction of the Material:"Reprinted with permission from [FULL CITATION]. Copyright [PUBLICATION YEAR], American Vacuum Society." For an article, the copyright and permission notice must be printed on the first page of the article or book chapter. For photographs, covers, or tables, the copyright and permission notice may appear with the Material, in a footnote, or in the reference list.
2. If you have licensed reuse of a figure, photograph, cover, or table, it is your responsibility to ensure that the material is original to AVS and does not contain the copyright of another entity, and that the copyright notice of the figure, photograph, cover, or table does not indicate that it was reprinted by AVS, with permission, from another source. Under no circumstances does AVS, purport or intend to grant permission to reuse material to which it does not hold copyright.
3. You may not alter or modify the Material in any manner. You may translate the Material into another language only if you have licensed translation rights. You may not use the Material for promotional purposes. AVS reserves all rights not specifically granted herein.
4. The foregoing license shall not take effect unless and until AVS or its agent, Copyright Clearance Center, receives the Payment in accordance with Copyright Clearance Center Billing and Payment Terms and Conditions, which are incorporated herein by reference.
5. AVS or the Copyright Clearance Center may, within two business days of granting this license, revoke the license for any reason whatsoever, with a full refund payable to you. Should you violate the terms of this license at any time, AVS, American Vacuum Society, or Copyright Clearance Center may revoke the license with no refund to you. Notice of such revocation will be made using the contact information provided by you. Failure to receive such notice will not nullify the revocation.
6. AVS makes no representations or warranties with respect to the Material. You agree to indemnify and hold harmless AVS, American Vacuum Society, and their officers, directors, employees or agents from and against any and all claims arising out of your use of the Material other than as specifically authorized herein.
7. The permission granted herein is personal to you and is not transferable or assignable without the prior written permission of AVS. This license may not be amended except in a writing signed by the party to be charged.
8. If purchase orders, acknowledgments or check endorsements are issued on any forms containing terms and conditions which are inconsistent with these provisions, such inconsistent terms and conditions shall be of no force and effect. This document, including the CCC Billing and Payment Terms and Conditions, shall be the entire agreement between the parties relating to the subject matter hereof.

This Agreement shall be governed by and construed in accordance with the laws of the State of New York. Both parties hereby submit to the jurisdiction of the courts of New York County for purposes of resolving any disputes that may arise hereunder.

Questions? customercare@copyright.com or +1-855-239-3415 (toll free in the US) or +1-978-646-2777.

AIP PUBLISHING LLC LICENSE
TERMS AND CONDITIONS

Mar 18, 2016

This Agreement between Jefferson Lab -- Md Abdullah Mamun ("You") and AIP Publishing LLC ("AIP Publishing LLC") consists of your license details and the terms and conditions provided by AIP Publishing LLC and Copyright Clearance Center.

License Number	3831731400871
License date	Mar 18, 2016
Licensed Content Publisher	AIP Publishing LLC
Licensed Content Publication	Journal of Vacuum Science & Technology A
Licensed Content Title	Effect of Sb thickness on the performance of bialkali-antimonide photocathodes
Licensed Content Author	Md Abdullah A. Mamun,Abdelmageed A. Elmustafa,Carlos Hernandez-Garcia, et al.
Licensed Content Date	Jan 6, 2016
Licensed Content Volume Number	34
Licensed Content Issue Number	2
Type of Use	Thesis/Dissertation
Requestor type	Author (original article)
Format	Print and electronic
Portion	Excerpt (> 800 words)
Will you be translating?	No
Title of your thesis / dissertation	THIN FILM STUDIES TOWARD IMPROVING THE PERFORMANCE OF ACCELERATOR ELECTRON SOURCES
Expected completion date	May 2016
Estimated size (number of pages)	150
Requestor Location	Jefferson Lab Jefferson Lab 600 KELVIN DR STE 8 Newport News, VA 23606-4468 NEWPORT NEWS, VA 23606 United States Attn: Matthew Poelker
Billing Type	Invoice
Billing Address	Jefferson Lab Jefferson Lab 600 KELVIN DR STE 8 Newport News, VA 23606-4468 NEWPORT NEWS, VA 23606 United States Attn: Matthew Poelker

Total 0.00 USD

Terms and Conditions

American Vacuum Society -- Terms and Conditions: Permissions Uses

American Vacuum Society ("AVS") hereby grants to you the non-exclusive right and license to use and/or distribute the Material according to the use specified in your order, on a one-time basis, for the specified term, with a maximum distribution equal to the number that you have ordered. Any links or other content accompanying the Material are not the subject of this license.

1. You agree to include the following copyright and permission notice with the reproduction of the Material:"Reprinted with permission from [FULL CITATION]. Copyright [PUBLICATION YEAR], American Vacuum Society." For an article, the copyright and permission notice must be printed on the first page of the article or book chapter. For photographs, covers, or tables, the copyright and permission notice may appear with the Material, in a footnote, or in the reference list.
2. If you have licensed reuse of a figure, photograph, cover, or table, it is your responsibility to ensure that the material is original to AVS and does not contain the copyright of another entity, and that the copyright notice of the figure, photograph, cover, or table does not indicate that it was reprinted by AVS, with permission, from another source. Under no circumstances does AVS, purport or intend to grant permission to reuse material to which it does not hold copyright.
3. You may not alter or modify the Material in any manner. You may translate the Material into another language only if you have licensed translation rights. You may not use the Material for promotional purposes. AVS reserves all rights not specifically granted herein.
4. The foregoing license shall not take effect unless and until AVS or its agent, Copyright Clearance Center, receives the Payment in accordance with Copyright Clearance Center Billing and Payment Terms and Conditions, which are incorporated herein by reference.
5. AVS or the Copyright Clearance Center may, within two business days of granting this license, revoke the license for any reason whatsoever, with a full refund payable to you. Should you violate the terms of this license at any time, AVS, American Vacuum Society, or Copyright Clearance Center may revoke the license with no refund to you. Notice of such revocation will be made using the contact information provided by you. Failure to receive such notice will not nullify the revocation.
6. AVS makes no representations or warranties with respect to the Material. You agree to indemnify and hold harmless AVS, American Vacuum Society, and their officers, directors, employees or agents from and against any and all claims arising out of your use of the Material other than as specifically authorized herein.
7. The permission granted herein is personal to you and is not transferable or assignable without the prior written permission of AVS. This license may not be amended except in a writing signed by the party to be charged.
8. If purchase orders, acknowledgments or check endorsements are issued on any forms containing terms and conditions which are inconsistent with these provisions, such inconsistent terms and conditions shall be of no force and effect. This document, including the CCC Billing and Payment Terms and Conditions, shall be the entire agreement between the parties relating to the subject matter hereof.

This Agreement shall be governed by and construed in accordance with the laws of the State of New York. Both parties hereby submit to the jurisdiction of the courts of New York County for purposes of resolving any disputes that may arise hereunder.

Questions? customercare@copyright.com or +1-855-239-3415 (toll free in the US) or +1-978-646-2777.

AIP PUBLISHING LLC LICENSE
TERMS AND CONDITIONS

Mar 18, 2016

This Agreement between Jefferson Lab -- Md Abdullah Mamun ("You") and AIP Publishing LLC ("AIP Publishing LLC") consists of your license details and the terms and conditions provided by AIP Publishing LLC and Copyright Clearance Center.

License Number	3831731294871
License date	Mar 18, 2016
Licensed Content Publisher	AIP Publishing LLC
Licensed Content Publication	Journal of Vacuum Science & Technology A
Licensed Content Title	Effect of Sb thickness on the performance of bialkali-antimonide photocathodes
Licensed Content Author	Md Abdullah A. Mamun,Abdelmageed A. Elmustafa,Carlos Hernandez-Garcia, et al.
Licensed Content Date	Jan 6, 2016
Licensed Content Volume Number	34
Licensed Content Issue Number	2
Type of Use	Thesis/Dissertation
Requestor type	Author (original article)
Format	Print and electronic
Portion	Figure/Table
Number of figures/tables	12
Title of your thesis / dissertation	THIN FILM STUDIES TOWARD IMPROVING THE PERFORMANCE OF ACCELERATOR ELECTRON SOURCES
Expected completion date	May 2016
Estimated size (number of pages)	150
Requestor Location	Jefferson Lab Jefferson Lab 600 KELVIN DR STE 8 Newport News, VA 23606-4468 NEWPORT NEWS, VA 23606 United States Attn: Matthew Poelker
Billing Type	Invoice
Billing Address	Jefferson Lab Jefferson Lab 600 KELVIN DR STE 8 Newport News, VA 23606-4468 NEWPORT NEWS, VA 23606 United States Attn: Matthew Poelker

Total 0.00 USD

Terms and Conditions

American Vacuum Society -- Terms and Conditions: Permissions Uses

American Vacuum Society ("AVS") hereby grants to you the non-exclusive right and license to use and/or distribute the Material according to the use specified in your order, on a one-time basis, for the specified term, with a maximum distribution equal to the number that you have ordered. Any links or other content accompanying the Material are not the subject of this license.

1. You agree to include the following copyright and permission notice with the reproduction of the Material:"Reprinted with permission from [FULL CITATION]. Copyright [PUBLICATION YEAR], American Vacuum Society." For an article, the copyright and permission notice must be printed on the first page of the article or book chapter. For photographs, covers, or tables, the copyright and permission notice may appear with the Material, in a footnote, or in the reference list.
2. If you have licensed reuse of a figure, photograph, cover, or table, it is your responsibility to ensure that the material is original to AVS and does not contain the copyright of another entity, and that the copyright notice of the figure, photograph, cover, or table does not indicate that it was reprinted by AVS, with permission, from another source. Under no circumstances does AVS, purport or intend to grant permission to reuse material to which it does not hold copyright.
3. You may not alter or modify the Material in any manner. You may translate the Material into another language only if you have licensed translation rights. You may not use the Material for promotional purposes. AVS reserves all rights not specifically granted herein.
4. The foregoing license shall not take effect unless and until AVS or its agent, Copyright Clearance Center, receives the Payment in accordance with Copyright Clearance Center Billing and Payment Terms and Conditions, which are incorporated herein by reference.
5. AVS or the Copyright Clearance Center may, within two business days of granting this license, revoke the license for any reason whatsoever, with a full refund payable to you. Should you violate the terms of this license at any time, AVS, American Vacuum Society, or Copyright Clearance Center may revoke the license with no refund to you. Notice of such revocation will be made using the contact information provided by you. Failure to receive such notice will not nullify the revocation.
6. AVS makes no representations or warranties with respect to the Material. You agree to indemnify and hold harmless AVS, American Vacuum Society, and their officers, directors, employees or agents from and against any and all claims arising out of your use of the Material other than as specifically authorized herein.
7. The permission granted herein is personal to you and is not transferable or assignable without the prior written permission of AVS. This license may not be amended except in a writing signed by the party to be charged.
8. If purchase orders, acknowledgments or check endorsements are issued on any forms containing terms and conditions which are inconsistent with these provisions, such inconsistent terms and conditions shall be of no force and effect. This document, including the CCC Billing and Payment Terms and Conditions, shall be the entire agreement between the parties relating to the subject matter hereof.

This Agreement shall be governed by and construed in accordance with the laws of the State of New York. Both parties hereby submit to the jurisdiction of the courts of New York County for purposes of resolving any disputes that may arise hereunder.

Questions? customercare@copyright.com or +1-855-239-3415 (toll free in the US) or +1-978-646-2777.

VITA

MD ABDULLAH AL MAMUN

M. A. Mamun obtained his B.S. in Mechanical Engineering in 1999 from Bangladesh University of Engineering and Technology (BUET). He secured an MBA in 2005 from Institute of Business Administration (IBA) of Dhaka University (DU). He received his M.S. in mechanical engineering from the College of Engineering and Computer Science of Florida Atlantic University (FAU) in 2009. He completed his Ph.D. in Mechanical Engineering at Old Dominion University (ODU) in 2016.

During his doctoral research, M. A. Mamun joined at the Jefferson Lab electron source group in 2011 as a graduate research assistant. At Jefferson Lab, M. A. Mamun completed experimental works for his Ph.D. dissertation on "Thin-film studies toward improving the performance of accelerated electron source." In search of the "Holy Grail" of cathodes for sourcing high average current and high brightness electron beams for DOE proposed accelerators, he worked on the optimization of the bialkali antimonide photocathode fabrication at Jefferson Lab. His work is appreciated as the first within the last decade or so to successfully use effusion sources in a reliable way to produce nice results for this photocathode. Some of his experiments are being reproduced by the researchers in Brookhaven National Lab (BNL) and University of Chicago, and has been found interesting by SLAC National Accelerator Lab and Lawrence Berkeley National Lab (LBNL) researchers.

M. A. Mamun conducts research in the experimental solid state physics with specific focus on the fabrication and characterization of functional thin films and bulk materials. Much of his study is focused on the low scale deformation and failure analysis by characterizing the nanomechanical properties of materials using nanoindentation technique. He has authored and co-authored 17 referred journal articles and 16 conference proceedings articles during his academic program at ODU. His works were presented to the scientific community through 10 oral presentations at conferences, 25 poster presentations, and 10 abstracts.

Prior to ODU he was a guest instructor and graduate research assistant in the Department of Mechanical Engineering at Florida Atlantic University (FAU). He served as a faculty member for the Department of Mechanical Engineering at Chittagong University of Engineering and Technology (CUET), Bangladesh from 2000-2003. Before joining FAU he briefly served in the supply chain function of Unilever Bangladesh Limited (UBL).

Throughout his academic program at BUET, M. A. Mamun received national level technical scholarship including the Dean's list award. He was awarded with graduate teaching/research assistantships throughout his study period in FAU. He enjoyed graduate research fellowship during his doctoral research at Jefferson Lab, and graduate teaching/research assistantship from MAE dept. of ODU from 2009-2010.

Contact Information: Email: mmamu001@odu.edu